Electromechanical Properties of 3D Multifunctional Nano-Architected Materials

Thesis by
Max L. Lifson

In Partial Fulfillment of the Requirements for the
Degree of
Doctor of Philosophy

Caltech

CALIFORNIA INSTITUTE OF TECHNOLOGY
Pasadena, California

2019
Defended December 13, 2018

ACKNOWLEDGEMENTS

sense of community.

Finally, I'd like to thank my family, whose support was critical to my success. Thank you to my parents, who have been an incredible source of inspiration, comfort, and guidance throughout my life. Thank you for the many encouraging phone calls and numerous joyous visits. Thank you to Steve, Dorothy, and Brian for cheering me on, especially as a new member to your family. Lastly, I'd like to thank my wife Lauren for her unwavering support and encouragement. Thank you for patiently standing by me as I have navigated the inevitable lows and celebrated the highs of my program. I love all of you very much.

ABSTRACT

In this thesis, we explore the fabrication and characterization of 3D architected multifunctional materials in three different categories: varied density for tailored mechanical response, stiff ultra low-k dielectric materials, and direct laser writing of piezoelectric structures at the micron scale. The density of an architected material plays a large role in determining its effective Young's modulus, strength, and deformation behavior. The first section of this work explores the effect of incorporating two density regions into hollow nanolattices, which results in two distinct mechanical response regions for horizontal interfaces and a combined varying response for a diagonal interface. The second section of this work describes low dielectric constant (low-k) materials, which have gained increasing popularity because of their critical role in developing faster, smaller, and higher performance devices. We report the fabrication of 3D nano-architected hollow-beam alumina dielectrics with a k value of 1.06 - 1.10 at 1 MHz that is stable over the voltage range of -20 to 20 V and a frequency range of 100 kHz to 10 MHz, with an effective Young's modulus of 30 MPa, a strength of 1.07 MPa, a nearly full shape recoverability to its original size after >50% compressions, and outstanding thermal stability with a thermal coefficient of dielectric constant (TCK) of 2.43×10^{-5} K^{-1} up to 800° C. Finally, we report the fabrication of monolithic piezoelectric ZnO structures of arbitrary shape via a polymer complex route. We have confirmed the microstructure using XRD, TEM, and SAED, and have observed its electromechanical response using a novel in-situ experiment.

PUBLISHED CONTENT AND CONTRIBUTIONS

1. Kim, M.-W., Lifson, M. L., Gallivan, R. A., Greer, J. R. & Kim, B.-J. Breakdown Behavior of Extreme Ultra Low-k Nano-Architected Materials. *In Preparation* (2019).
   M.L.L. participated in the conception of the project, designed and fabricated the samples, developed the electrical breakdown mechanism, participated in creating the FEA model, and participated in the writing of the manuscript.

2. Lifson, M. L. & Greer, J. R. Utilizing Density in 3D Nano-architected Materials for Tailored Mechanical Response. *In Preparation* (2019).
   M.L.L. participated in the conception of the project, fabricated the samples, performed and analyzed the mechanical experiments, and participated in the writing of the manuscript.

3. Yee*, D. W., Lifson*, M. L. & Greer, J. R. Additive Manufacturing of 3D Architected Multifunctional Metal Oxides. *In Preparation* (2019).
   M.L.L. participated in the conception and design of the project, participated in developing the heating profile and performing SEM analyses, performed the XRD analyis, prepared samples for and performed TEM analyses, conceived and built the electromechanical set up, performed the in-situ open circuit voltage response experiments, and participated in the writing of the manuscript.

4. Lifson*, M. L., Kim*, M.-W., Greer, J. R. & Kim, B.-J. Enabling Simultaneous Extreme Ultra Low-k in Stiff, Resilient, and Thermally Stable Nano-Architected Materials. *Nano Letters* **17.** doi: 10.1021/acs.nanolett.7b03941, 7737–7743 (2017).
   M.L.L. participated in the conception of the project, fabricated the samples, prepared the mechanical data from reported values, developed the analytical relationship between dielectric constant and stiffness, and participated in the writing of the manuscript.

TABLE OF CONTENTS

LIST OF ILLUSTRATIONS

LIST OF TABLES

C h a p t e r   1

INTRODUCTION

1.1   Materials Design

One major goal of materials science is to understand and design the underlying properties of a material in order to characterize or optimize its performance for particular applications or fundamental understanding. For the majority of the field's history, this has involved studying the atomic microstructure of materials in order to improve their macroscopic properties, such as improving strength through high carbon steel [1], decreasing corrosion susceptibility [2], lowering the melting point of metals through eutectic compositions [3], and changing the electrical properties of materials through atomic doping [4]. This has resulted in stronger materials for structural and vehicular applications, a myriad of electrical and semiconducting materials for integrated circuits, and bio-compatible materials for human implants. A powerful additional method to continue improving materials which have become vital to modern technological development is introducing architecture into materials design.

1.2   Architected Materials

Architected materials are composite materials that utilize two or more materials, or materials and space, to produce collective properties that are more useful than those of one component alone [5]. These materials are not new — ancient Greeks attached iron rods to marble slabs in order to achieve greater spans than possible with only marble [6]. Architected materials are also found in numerous biological settings, including the human body. For example, tribecular bone contains a hierarchical composite structure of tribecular fibers, with an underlying nanocomposite structure that provides its high strength and damage resistance [7]. In modern technology, composite materials are increasingly important, recently making up half of the weight of a Boeing 787 Dreamliner, for example [8].

One particularly powerful method of utilizing architecture in materials design is to introduce porosity into materials. This is easily recognizable on both the large scale, in building construction like the Eiffel Tower, to small everyday items, such as household dish sponges. Stochastic porosity can significantly reduce the weight of engineering materials, resulting in both beneficial strength-to-weight ratios and

greater surface area [9, 10]. However, consciously architected porosity has been shown to have particular advantages at very low densities. In addition to the constituent material and geometry of architecture, porous, or cellular, solids can be characterized by their relative density. The effective Young's modulus, E^*, which is a measure of the stiffness of a material, is known to scale by the following relation:

$$E^* \propto E_s \overline{\rho}^n \tag{1.1}$$

where E_s is the Young's modulus of the fully dense constituent material, $\overline{\rho}$ is the relative density, and n is a parameter defined by the cell geometry [11]. Hexagonal honeycomb structures, which are important historical and current 2D architected cellular solids [12, 13], exhibit a scaling value n of 3 for in-plane stiffness [14]. Ultralight stochastic foams have also been shown to exhibit an n value of 3 [15], while higher density open cellular foams and periodic non-rigid ultralight structures have been shown to follow an n value of 2 [11, 16, 17]. Rigid 3D nano-architected periodic nanolattices described in the following chapters have been shown to exhibit an n scaling value of 1.61 [18], which allows this material to maintain a higher level of mechanical stiffness as the relative density decreases. This shallower drop-off of mechanical performance, as well as its inherent tunability, make 3D architected nanolattices a very promising candidate for engineering materials for a variety of lightweight applications.

1.3 Architected Multifunctional Materials

While porosity itself can be considered a feature of multifunctionality, as porous materials can be used as a mechanical materials while providing a beneficial strength-to-weight-ratio, the following sections focus on functionality besides weight saving. For ease of description, we can separate this field into passive and active multifunctionality.

Passive Multifunctionality

For this work, we define passive functionality as one where no external action is required for the material to make use of the function. Beyond their weight-saving capabilities and improved mechanical properties over stochastic foams, 3D architected multifunctional materials have been used in a variety of passive functional applications.

- **Biological**

Additive manufacturing is particularly well suited for biological devices and materials, as they can be tailored to fit specific functions and can be customized for individual people. In particular, 3D architected multifunctional materials have been proposed and demonstrated for several passive biological applications. It has been shown that the stiffness of a bone tissue scaffold can greatly influence the rate of bone tissue growth [19]. Similarly, the surface of architected structures have been functionalized with various chemical functional groups for drug delivery, drug capture, and antifouling applications [20].

- **Thermal and Electrical**

As expected for highly porous structures, hollow alumina nanolattices have been shown to exhibit ultralow thermal conductivity and mechanical resilience [21]. As will be elaborated on in a following section, the vast majority of 3D architected materials at the micron scale have been polymers due to the versatility of photolithography. Recent advances in micro-additive manufacturing techniques have expanded to include core-shell composite or hollow beam structures, as well as very recent monolithic carbon, metal, and metal oxides materials. As such, understanding the electrical properties of these materials has become a young, but growing field. Interesting anisotropic electrical conductivity has been shown for graphene/SiC composite woodpile structures [22]. Due to their high porosity and high stiffness-to-weight ratio, 3D architected materials are also very well suited for low-k dielectric applications, as will be explored in Chapter 4.

Active Smart Materials

Active smart materials are defined here as materials that respond directly to external stimuli. These responses can be used as sensors, actuators, and other novel devices.

- **Sensors**

Nano-architected materials are particularly well suited for sensors due to their controllable high surface-to-volume ratio and high surface activity [23]. A templated collection of alumina nanotubes can be used as a humidity sensor due to resistance changes [24]. Similarly, changes in resistance or current in zinc oxide (ZnO) nanowire devices have been used to demonstrate pH and UV sensors [25], and

changes in resistance in tin dioxide (SnO_2) nanowires have been shown to enable highly sensitive gas sensors [23].

• **Shape Memory Alloys**

One of the most widespread smart architected materials is used in stents made of Nitinol for clearing or keeping open human arteries [26]. This and other shape memory materials can be activated to return to a thermally programmed shape after deformation. For example, a shape memory alloy stent or pipe can be cooled, deformed to a smaller shape, inserted into an artery or fitting, and finally heated to return to its original larger shape, either opening the artery or creating a tight seal in the case of a pipe. Shape memory alloys also have a beneficial power to weight ratio over other actuator systems and represent a promising lightweight replacement [27].

• **Piezoelectric Materials**

Another large category for actuators, as well as sensors, is piezoelectric materials. These materials will be discussed in more detail in Chapter 5, but in brief, a piezoelectric material can expand or shrink with an applied voltage or can produce a voltage when stressed. Piezoelectric architected materials have been proposed for many applications, including energy harvesting [25], force sensing and actuation [26, 27], bone tissue stimulating scaffolds [28], and improved smaller resonators for portable imaging technologies, such as ultrasound [29].

Summary and Outlook

Multifunctional materials have been and will continue to be a promising field for new innovation. The field of architected materials in particular has exploded over the last several years due to advances in micro-additive manufacturing and is still in its infancy. These advancements have opened up a large parameter space in which to create novel devices and materials to improve some of society's greatest problems.

1.4   Micro-Additive Manufacturing

The explosion of micro-additive manufacturing (AM) techniques over the last two decades has opened a vast property space for engineering materials and materials design. Self-propagating photopolymer waveguides have been used to create micro-scale truss structures with beam diameters in the range of 80-180 µm for periodic linear structures [30]. Another fabrication technique is holographic lithography,

which can create periodic 10-60 μm thick films with unit cell sizes on the order of 400 nm [31]. The popular technique of digital light processing (sometimes combined with microstereolithography) has been used to create complex 3D polymer structures with a projected pixel size of 5 x 5 μm^2 and a layer spacing of 5 μm [32]. Two-photon lithography (TPL) has been demonstrated as an extraordinary AM technique in that it can produce sample beams below 1 x 1 μm^2 in cross section [33]. The greatest advantage of TPL is its ability to create any arbitrary 3D geometry at the micron scale. A detailed explanation of the mechanism TPL utilizes is described in the following chapter, and a further description of TPL's unique utility can be found in Chapter 5.

1.5 Outline and Objectives

The focus of this thesis is on recent developments we have made in the field of 3D architected multifunctional materials. These materials have been enabled by new micro-additive manufacturing techniques, and we highlight those specifically fabricated with two-photon lithography (TPL). Our group has previously shown hollow ceramic porous nanolattices to posses highly tunable and desirable mechanical properties in structures of uniform density. It has also recently shown that these structures can be fabricated to possess unique thermally insulating [21], chemically functionalized [20], mechanically robust lithiating [34], and tunable photonic [35] capabilities. In the following chapters, this thesis pushes this body of work into the realm of multiple densities, and delves deeper into the multifunctional capabilities of these materials by exploring electromechanical functionalities. In order to highlight the versatility of these materials, three examples in different categories of multifunctionality will be explored.

This work begins by describing the fabrication and characterization of architected dielectric materials in Chapter 2. Chapter 3 explores the effect of combining two regions of different density into the same structure. Varying the configuration of these different density regions is shown to allow considerable tuning of the nanolattice's stiffness, strength, and deformation behavior. Moving beyond the purely mechanical world, the rest of this thesis will describe projects within two main applications for electrically multifunctional materials, one passive and one active, to show the power of these techniques. Chapter 4 demonstrates the exceptional performance of porous nanolattices as extreme ultra low-k dielectric materials. In particular, they exhibit remarkably low dielectric constant to stiffness ratios and remarkably stable behavior across voltage, frequency, and temperature. The following chapters will

describe the fabrication and characterization of 3D architected piezoelectric materials. Chapter 5 will discuss the novel fabrication method and characterization of monolithic 3D architected ZnO, as well as the custom measurement system that was built to study its electromechanical properties. Chapter 6 will discuss the efforts to quantify the electrical measurements from this custom system on quartz pillars and propose additional experiments to improve the understanding of new materials. The last chapter will provide a summary and outlook for this work.

C h a p t e r   2

FABRICATION AND CHARACTERIZATION OF ARCHITECTED DIELECTRICS

The fabrication process of architected dielectric materials occurs in several steps. First, a structure is designed. Next, a polymer scaffold is written and coated with the dielectric material. Finally, the interior polymer is removed, resulting in a hollow dielectric structure. These steps and the methods used to characterize these nanostructures are illustrated in more depth in the following sections of this chapter.

2.1 Design

Before fabrication, the exact architecture and dimensions are designed in the computer aided design (CAD) software SolidWorks. Figure 2.1 shows a representative image of an octet unit cell CAD design. While any arbitrary shape can be fabricated within the resolution of the additive manufacturing technique, space-filling unit cells are typically used to create engineering materials. For the majority of this work, we have chosen to use the octet truss, or simply phrased "octet", unit cell due to its ease of manufacture, its high strength-to-weight ratio, and high stiffness [18, 36].
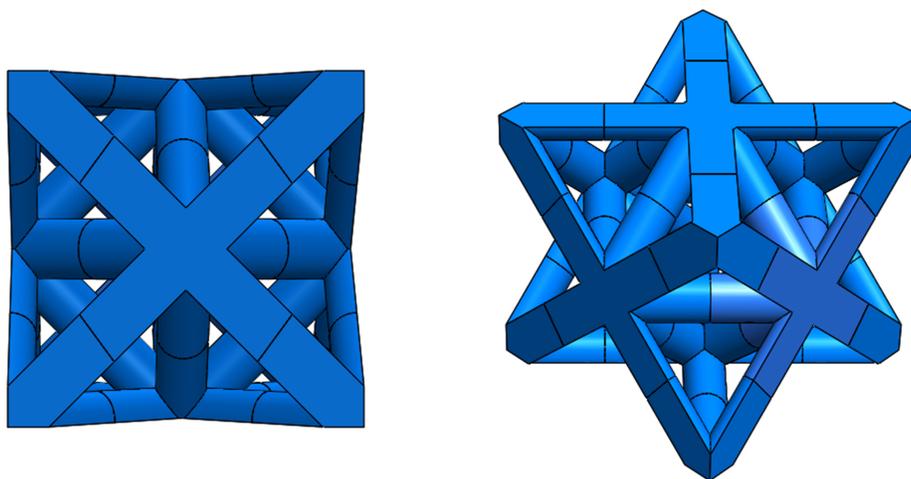
Figure 2.1: SolidWorks CAD design of octet unit cell face-on view (left) and isometric view (right).

In order to actually fabricate the modeled structures, instructions are needed to specify the tessellation of the unit cell and to prescribe the spacing between fabrication layers in the z direction and between each pass of the laser in the x-y plane. The CAD design can be imported directly into the additive manufacturing system's software to specify these parameters, however, we have chosen to create more detailed instructions to enable larger control over the writing parameters. With our CAD design in mind, we utilize MATLAB code to control the unit cell architecture and dimensions, write spacing within a layer and between layers, and strut shape. The shape of the voxel, or writing volume, is elliptical by default due to the optics of our laser. Code has been adapted to create more circular beams by carefully overlapping passes of the beam. This increases the minimum resolution of the technique, but provides greater control over the shape of the struts. Ultimately, this code generates a file which instructs the AM system to write along the prescribed pathway until the structure is completed. More detailed information can be found in Reference [37].

2.2 Two Photon Lithography Writing
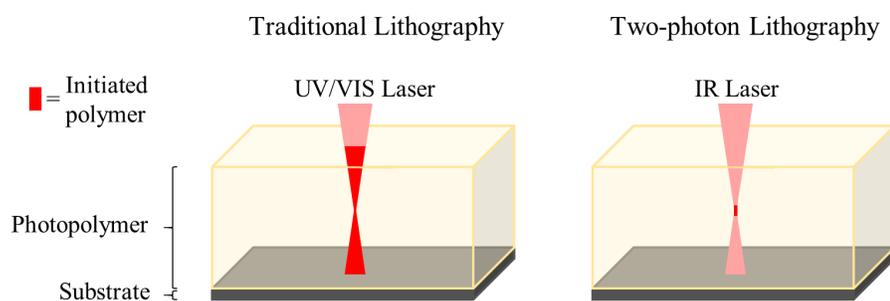
Figure 2.2: Comparison of traditional and two-photon lithography. The dark red region signifies polymer that has been photoinitiated

While there have been many advances in the field of additive manufacturing over the last decade, two-photon lithography (TPL) direct laser writing (DLW) has emerged as a particularly interesting technique due to its small resolution and shape versatility [33]. Unlike traditional lithography, which utilizes light, typically in the ultraviolet (UV) spectra, to crosslink polymer throughout the photoresist volume, TPL enables full 3D control of crosslinking. This 3D control is possible because the photoiniator, which starts the chain reaction of polymerization, is only activated by an energy that is just less than the energy of two photons. As such, the volume that is initiated into

crosslinking is confined to the volume where the laser is focused enough such that there is a high probability of the photoinitiator absorbing two photons. This process is illustrated in Figure 2.2.

A Photonic Professional TPL-DLW System (Nanoscribe GmbH) with an IR laser was used to fabricate the polymer scaffolds used in this work. Unless otherwise noted, such as in Chapter 5, IP-DIP 780 polymer was used on silicon (Si) substrates. Write scan speed and laser power were optimized for each structure by fabricating dosage sweep arrays. If the energy dose is too high, above the energy required for polymerization, the polymer will bubble due to local evaporation [38, 39]. If the dose is too low, there will be insufficient energy to fully crosslink the polymer. Once all of the structures on the substrate are completed, they can be developed as follows. First, the Si chip substrate that holds the structures is placed in propylene glycol monomethyl ether acetate (PGMEA) for 20 minutes to dissolve and remove the uncrosslinked polymer. It is then immediately submersed in isopropyl alcohol (IPA) for at least 5 minutes. This development process results in a shrinkage from the as-written size of approximately 10%.

Stitching
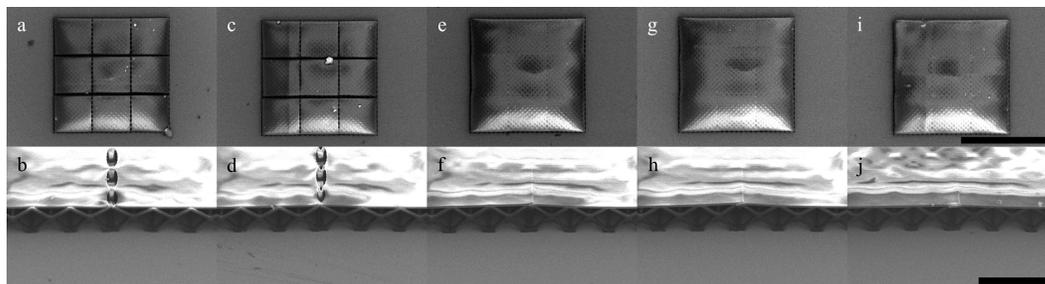
Figure 2.3: Stitching optimization of large nanolattices. Top-down and side-edge view of nanolattices stitched with a-b) -2 μm, c-d) -1 μm, e-f) +1 μm, g-h) +2 μm, i-j) +4 μm overlap. Scale bars for the top and bottom rows are 300 μm and 30 μm, respectively.

The field of view of the TPL system is limited to a circle of roughly 140 μm in diameter, and the stage is limited to 300 μm of travel in the x,y,z directions. As such, if structures that are larger than this are desired in the x-y plane (such as those in Chapter 4), the TPL instruction file must stitch these structures together via either a piezo (if under 300 μm) or stage movement. If taller structures are desired, stitching must be done with the stage in the z direction. For this work, structures up to 1 mm x 1 mm, but below 300 μm in height were required. As such, stage movement

parameters were optimized to stitch nanolattices together. Figure 2.3 shows 3 x 3 arrays of nanolattices with varying overlap distances. An overlap of +2 μm was selecting as having the most reliable overlap to ensure full coverage of the top plate.

Critical Point Drying

After developing the sample, the solvent must be removed. Critical point drying (CPD) is used to remove the IPA used during developing in order to avoid damage to the structure caused by capillary forces during evaporation. An Autosamdri 931 (Tousimis) was used with CO_2 for all samples except those described in Chapter 5.

2.3 Scaffold Coating with Alumina and Hollowing

Once the polymer scaffolds were developed and dried, they were coated with approximately 10 nm of alumina (Al_2O_3) in a Cambridge Nanotech S200 ALD (atomic layer deposition) system using H_2O and trimethylaluminum (TMA) precursors. The deposition was performed at 150° C and consisted of 100 cycles of a 15 ms pulse of H_2O, a purge for 20 s, a 15 ms pulse of TMA, and a purge for 20 s. A focused ion beam (FIB) system (FEI Versa 3D) was then used at 30 kV and 1 nA to remove portions of the outer alumina coating. Figure 2.4a and b show a polymer nanolattice and a coated nanolattice with the edge faces removed with the FIB, respectively. For large samples with a top plate, such as those in Chapter 4, additional holes were carefully created in the "roof" coating of the structure to allow for greater internal access. The samples were then placed in a Diener Zepto oxygen plasma system at 100 W and 0.6 mbar pressure for several hours in order to remove the now-exposed interior polymer scaffold. Figure 2.4c and d show a partially hollow nanolattice after 5 hours of plasma immersion and a fully hollow nanolattice, respectively. Some additional fabrication considerations and challenges can be found in Appendix A.
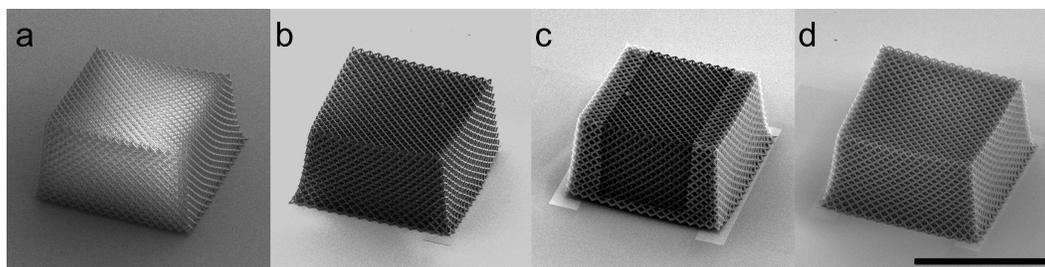
Figure 2.4: Hollowing process of nanolattices via oxygen plasma. a) Polymer nanolattice. b) Nanolattice coated with alumina with the edges milled by the FIB. c) Nanolattice after 5 hrs in the oxygen plasma, with hollow sides. d) Fully hollow nanolattice. Scale bar 100 μm.

2.4 Electron Beam Imaging

At the polymer, core-shell composite, and hollow stages of fabrication, samples are imaged using Scanning Electron Microscopy (SEM). While the outline of many of these structures can been seen via optical microscopy, SEM allows for imaging of the micron and nanometer-scale features that lend these structures their unique properties. A Quanta and Versa 3D SEM (both ThermoFisher Scientific) were used, typically at 2-5 kV accelerating voltage. Images were used to optimize fabrication parameters, and measurements from these images were fed back into the CAD model in order to obtain accurate relative density measurements.

2.5 Mechanical Characterization

In order to characterize the mechanical properties of these novel architected materials, we utilized nanomechanical testing equipment in order to perform compression experiments at extremely high resolution and quasi-static (10^{-3} s^{-1}) speeds. There are two configurations of this experiment, both ex-situ and in-situ.
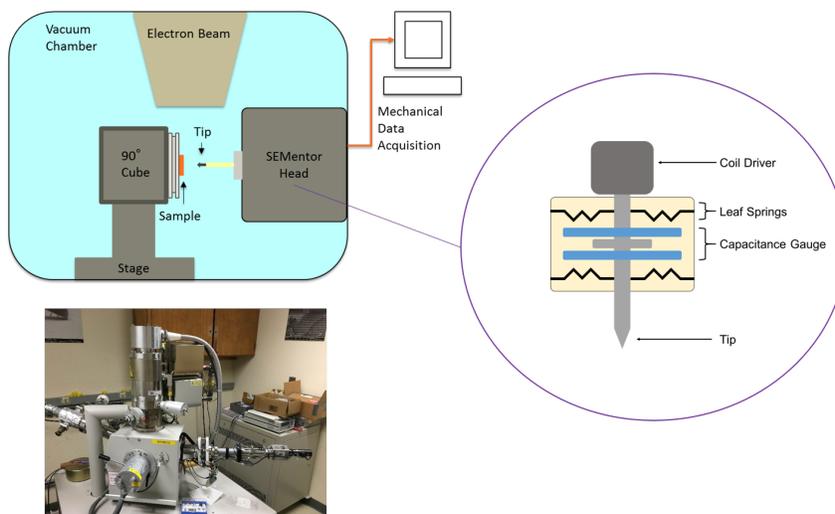
Figure 2.5: Schematic and picture of the SEMentor in-situ mechanical characterization equipment.

Figure 2.5 shows a schematic and picture of the in-situ mechanical equipment, nicknamed "SEMentor", which consists of an InSEM Nanomechanical Module (Nanomechanics, Inc.) attached to a Quanta SEM (ThermoFisher Scientific). The configuration of the nanomechanical module inside the SEM chamber allows for simultaneous imaging during the mechanical experiments. The heart of the experiment is the nanomechanical, or SEMentor, head. This transducer is actuated by a coil driver and contains a capacitance gauge that measures the displacement of the

shaft. At the end of the shaft is a tip, which can be removed and replaced with a tip of different geometry and size to best match the type of experiment being performed. The leaf springs control the conversion of the applied force from the coil driver to the tip displacement, as would be expected from Hooke's law, and their linearity is of critical importance to the accuracy of the measurement. A further discussion of this and the associated corrections can be found in Appendix B. A feedback system allows for this experiment to be run in either a displacement or load controlled configuration - in this work, we chose to maintain consistent displacement control in order to maintain a constant strain rate. The transducer has a maximum load of 50 mN and a maximum range of 40 μm. This system can also be run in an extension mode, where the extension arm that holds the transducer applies the displacement to the sample, while the transducer measures the force required to maintain its capacitive displacement location. This method lowers the mechanical resolution of the experiment, but allows for displacements beyond 40 μm. The significant advantage of these in-situ techniques is that they allow for the characterization of deformation of materials that would otherwise be invisible from the mechanical data alone.

The ex-situ variation of this experiment in a G200 Nanoindenter (Agilent Technologies) utilizes an almost identical configuration, except the transducer is vertical above a horizontal sample, and an optical microscope is used to align the experiment, but the experiment occurs without simultaneous viewing. This transducer has a maximum load of 500 mN, a maximum displacement range of 500 μm, and is in general much more stable (<0.05 nm/sec drift) due to better vibration isolation.

For this work, stress is defined as the load per footprint area of the sample and strain is defined as the displacement normalized by the original sample height. Due to the inherent brittle nature of the constituent ceramic material, the maximum slope upon loading of the stress-strain data was used to determine the effective Young's modulus (E^*), and the first significant failure event was used to determine the effective strength (σ^*). A representative example can be found in Figure 2.6. It should be noted that we use "effective" Young's modulus and strength, rather than yield stress, as we were testing a finite number of unit cells in these cellular solids. While we were careful to use more than 5 unit cells in every direction in order to limit the effect of the boundary conditions, this remains an approximation of the true continuum material behavior.
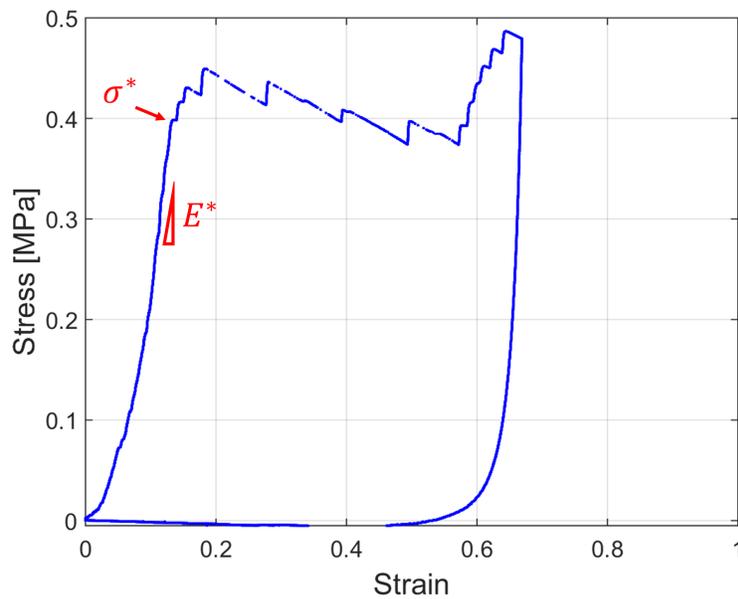
Figure 2.6: Representative mechanical data example to illustrate locations for Young's modulus and strength.

2.6 Summary

In summary, this chapter has described the fabrication and characterization methods of 3D nano-architected dielectric materials. These materials were created using the versatile TPL method to create a polymer scaffold upon which a thin conformal layer of alumina was applied via ALD. After removing regions of the outer shell to expose the scaffold, the underlying polymer was removed via oxygen plasma. This resulted in a hollow beam nanolattice, which was imaged in an SEM. Mechanical experiments were performed using nanomechanical testing equipment to produce yield-displacement, and subsequent stress-strain data. These techniques allow us to develop and characterize novel materials for a variety of applications, as well as gain deep understanding of the mechanics of architected materials at the micro and nano scale.

C h a p t e r   3

UTILIZING DENSITY IN 3D NANO-ARCHITECTED MATERIALS FOR TAILORED MECHANICAL RESPONSE

Adapted with permission from:

1. Lifson, M. L. & Greer, J. R. Utilizing Density in 3D Nano-architected Materials for Tailored Mechanical Response. *In Preparation* (2019).

The previous chapter discussed the fabrication and characterization methods of hollow architected dielectric materials. This chapter will discuss the first of three examples of novel multifunctionality of these materials, utilizing regions of two densities to influence their mechanical deformation response.

3.1   Introduction

Porous materials are becoming increasingly important for their weight-saving utility, as well as their multifunctional properties as thermal insulators for energy-saving houses [40] and direct flame protection [24], gas sensors [24, 41], Li ion battery anodes and cathodes [42, 43], catalysis materials [44, 45], and solar cell components [40, 46], to name a few applications. New 3D architected materials that are enabled by improved additive manufacturing technology have several distinct advantages over more traditional stochastic foams. Mechanically, nanolattices produced via two photon lithography (TPL) have exhibited high tensile elasticity [47], high strength-to-density ratios [48], suppression of brittle failure [49, 50], flaw insensitivity [51], and exceptional mechanical resilience [18, 52]. They have also exhibited remarkably low thermal conductivity to specific modulus values [21] and extreme ultra low dielectric constant to stiffness ratios [53]. Recent work has shown that the node geometry can play a significant role in the effective stiffness of non-slender nanolattices [17]. It has also been shown that careful architectural design can be used to create tailored buckling of polymer nanolattices [54] and structures that twist when compressed uniaxially [55]. However, through simply altering the density in these nanolattices, it has been shown one can specifically tailor the function of these structures, such as their stiffness [18], dielectric constant [53], and efficiency of bone tissue growth [19]. While these properties alone are unique and useful, what would happen if one combined two regions of different density? If it is possible

to utilize TPL to create a multiple stiffness material, or one with a tailored deformation, the technique could have particular utility in shock absorption for vehicles and biomechanics [56–58], dual stiffness floors to prevent fractures from falls [59], o-ring seal technology [60], and tailored protective equipment [61]. In this work, we show that varying the density within a nanolattice, even coarsely, does allow for the tailoring of its mechanical response and deformation.

3.2 Methods

Sample Fabrication
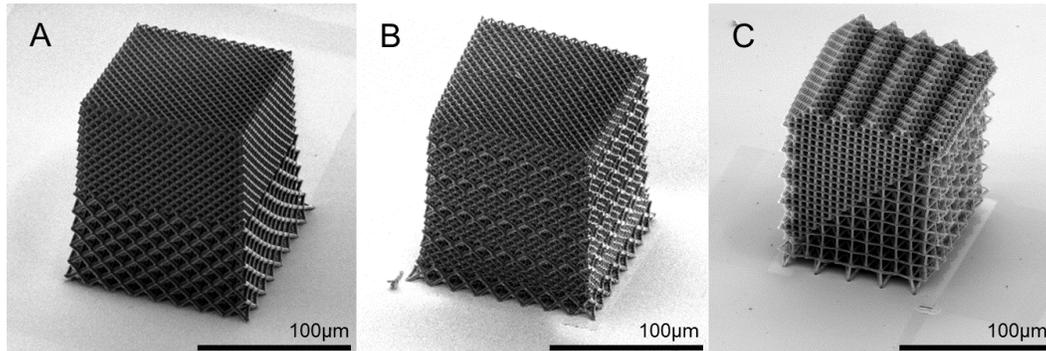
Figure 3.1: Overview of varied density nanolattices. A) Bi-phase nanolattice, B) alternating layer nanolattice, and C) diagonal interface nanolattice.

Nanolattices with nearly cylindrical beams and octet geometry with unit cells of 8 μm and 16 μm were designed in CAD software. Uniform density structures, comprised of all 8 μm (high density) or 16 μm (low density) unit cells were designed to be 128 μm x 128 μm x 80 μm for use as control samples. Bi-phase density structures consisted of a 128 μm x 128 μm x 80 μm section with an 8 μm unit cell stacked immediately on top of a section of the same dimensions with a 16 μm unit cell (Figure 3.1A). Alternating layer density structures consisted of repeating layers of 16 μm unit cell layers below two 8 μm unit cell layers for a total combined design height of 128 μm x 128 μm x 160 μm (Figure 3.1B). The diagonal nanolattices were fabricated using the same unit cells as the non-diagonal ones, however the unit cells were rotated 45° in the x-z plane (Figure 3.1C). The layers are stacked such that the bottom plane is comprised of only 16 μm unit cells. The next layer is staggered by half a unit cell laterally and vertically to create a pattern with no gaps and is otherwise a repeat of the layer before. With each subsequent pair of two staggered layers, one additional row of 16 μm unit cells is replaced by a 2x2 diamond row of 8 μm unit cells until the top layer is of uniform high density. This results in a

designed 113 μm x 112 μm x 147 μm structure. These designs were then used to fabricate polymer scaffolds using two photon lithography (TPL) direct laser writing (DLW) in a Photonic Professional TPL-DLW System (Nanoscribe GmbH) in IP-DIP 780 polymer on silicon substrates. These polymer scaffolds were then coated with 12 nm of alumina in a Cambridge Nanotech S200 atomic layer deposition (ALD) system using H_2O and trimethylaluminum (TMA) precursors. In order to remove the sacrificial polymer scaffold, opposite lateral sides of the alumina coating were removed using a Versa 3D (ThermoFisher Scientific) focused ion beam (FIB). The samples were then immersed in an oxygen plasma within a Diener Zepto plasma system until the nanolattices were completely hollow.

Density Calculation

The relative density of each density region was calculated by estimating the fraction of material in each unit cell volume. This was done by measuring the unit cell and beam dimensions of coated and uncoated nanolattices using an SEM and creating CAD models of the structures using these real measurements. The difference between these two material volumes divided by the total volume of the unit cell is the relative density of the final hollow unit cell.

Uniaxial Compression Experiments

Two types of uniaxial compression experiments were performed. Ex-situ experiments were performed using a 650 μm diameter stainless steel flat punch tip in a G200 Nanoindenter (Agilent Technologies) utilizing the XP load cell. In-situ mechanical experiments were performed in a Quanta SEM (ThermoFisher Scientific) with an attached InSEM Nanomechanical Module (Nanomechanics, Inc.) using a 500 μm diameter stainless steel flat punch tip. This experiment was conducted using the extension arm to provide displacement while the load cell measured the force required to maintain a fixed transducer displacement. All samples were loaded to about 80% strain at a constant strain rate of 10^{-3} s^{-1}. In both types of experiments, the effective Young's modulus was defined as the maximum slope during the elastic loading portion of the experiment, and the effective strength was defined as the stress at which the first major failure event occurred. The recoverability was defined as the measured nanolattice height after one cycle of compression (to about 80% strain) divided by the initial pristine nanolattice height.

3.3 Mechanical Response of Varied Density Nanolattices

The relative densities of the 8 μm and 16 μm unit cell were calculated to be 0.87% and 0.43%, respectively. Each size was designed to have similar beam radius to length a/L values with wall thickness to radius t/a values below the $t/a_{crit} \approx 0.016$ lower limit for enabling shell buckling, which provides architectural recoverability from an otherwise brittle ceramic material [18]. The actual a/L values of 0.11 and 0.12 and t/a values of 0.0157 and 0.0086 were measured for the 8 μm and 16 μm unit cells, respectively. The 8 μm unit cell had a major axis beam radius of 765 nm and a minor axis beam radius of 650 nm. The 16 μm unit cell had a major axis beam radius of 1.4 μm and a minor axis beam radius of 1.3 μm.

The stiffness scaling of these hollow nanolattices has been shown to follow the relation:

$$E^* \propto \overline{\rho}^n \tag{3.1}$$

where E^* is the effective Young's modulus, $\overline{\rho}$ is the relative density, and $n = 1.61$ [18]. This scaling is significantly improved for low densities over the scaling of $n = 3$, observed for ultralight stochastic foams [15], or $n = 2$, for higher density open cellular foams or periodic non-rigid ultralight structures [11, 16, 17]. Matching intuition, the relation in Equation 3.1 indicates that the effective Young's modulus of a uniformly high density structure will be higher than that of a uniformly low density structure. The effective Young's modulus of the uniform nanolattice made up entirely of 8 μm unit cells was 11.6 ± 2.9 MPa compared to 1.96 ± 0.47 MPa of the uniformly 16 μm unit cell nanolattice. When combining regions of two different materials in one structure, one might expect to calculate a single expected stiffness based on a model of two springs in series. However, vast differences in effective strength prevent both regions from being substantially loaded at the same time. The strength of these hollow nanolattices also scale with density and have been shown to behave according to the following relation:

$$\sigma^* \propto \overline{\rho}^m \tag{3.2}$$

where σ^* is the effective strength and $m = 1.76$ [18]. For example, the measured strength of the uniformly high density nanolattice was 390 ± 14 kPa, compared to 75 ± 0.71 kPa for the uniformly low density nanolattice.

Bi-phase Nanolattice
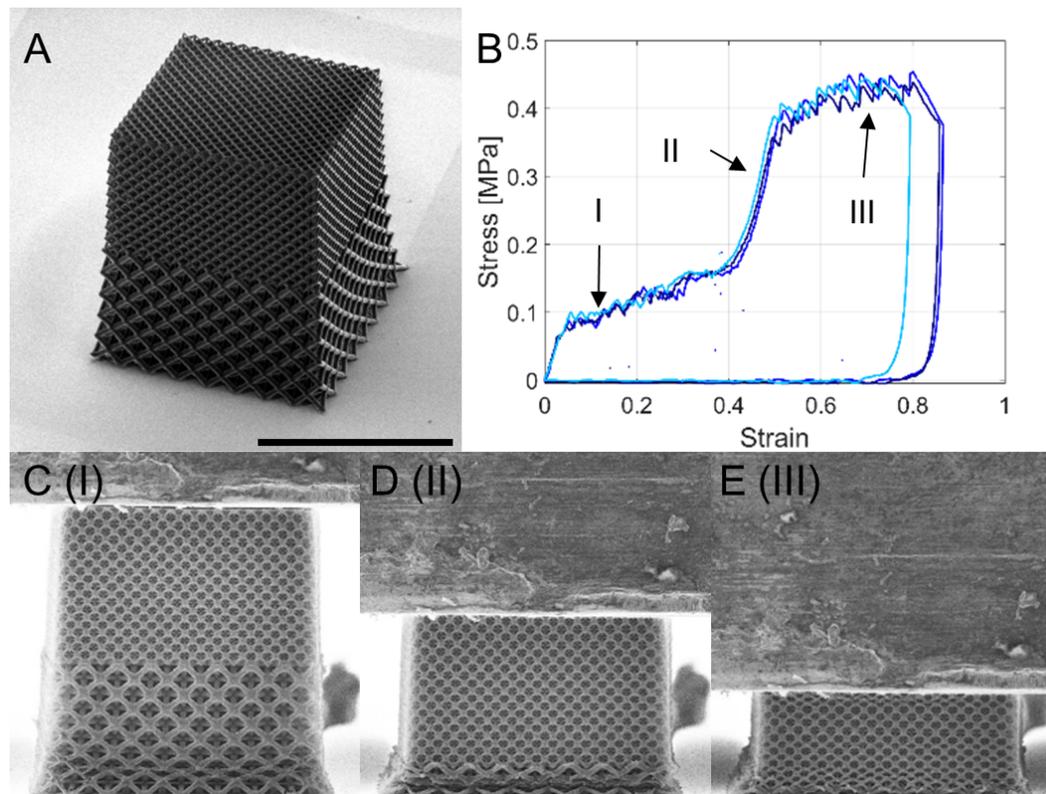
Figure 3.2: Bi-phase nanolattice A) SEM image of the undeformed hollow structure. Scalebar is 100 μm. B) Ex-situ mechanical data. C-E) SEM images during in-situ testing at strains indicated by I, II, and III in B. The width of each image is 150 μm.

Figure 3.2A shows an SEM micrograph of the bi-phase nanolattice. Ex-situ mechanical data can be found in Figure 3.2B. Figure 3.2C-E show the deformation of the nanolattice at each indicated point during the in-situ experiment. A video of this experiment can be found in the supplementary materials as Supplementary Movie 1. Just beyond the first elastic loading regime, the low density layers begin to shell buckle one by one, as seen in Figure 3.2C. The effective Young's modulus of this low density regime was measured as 4.43 ± 0.93 MPa, with a strength of 66 ± 1.7 kPa. During this initial phase of the compression, the high density region behaves as if it is part of the indenter tip and exhibits no noticeable deformation. Figure 3.2D shows that once all of the low density layers have yielded, there is a transition region where the high density region begins to experience loading. Beyond the transition region, the high density layers shell buckle one by one, as seen in Figure 3.2E, until the experiment reaches the prescribed strain. The effective Young's modulus of this second regime was measured as 5.45 ± 0.80 MPa, with a strength of 380 ± 15 kPa.

The recoverability of this nanolattice was measured as 82% from one cycle of in-situ experiments.

Alternating Layer Nanolattice
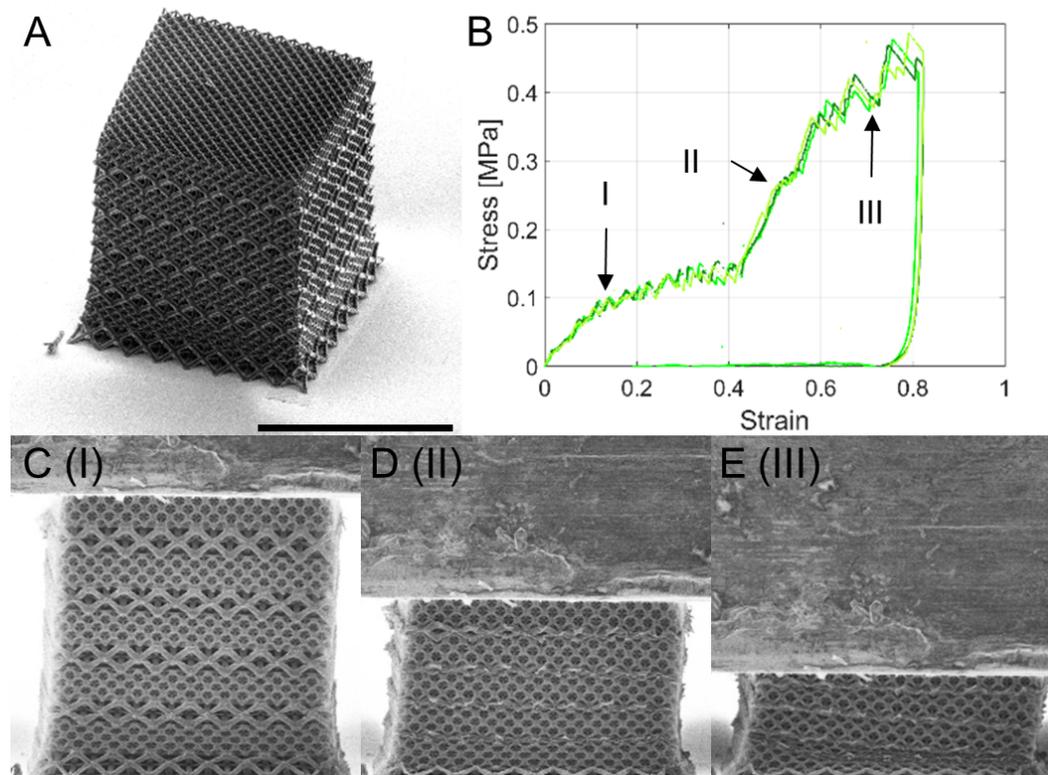
Figure 3.3: Alternating layer nanolattice A) SEM image of the undeformed hollow structure. Scalebar is 100 µm. B) Ex-situ mechanical data. C-E) SEM images during in-situ testing at strains indicated by I, II, and III in B. The width of each image is 140 µm.

An SEM micrograph of the alternating layer nanolattice can be found in Figure 3.3A, with corresponding ex-situ mechanical data in Figure 3.3B. As with the bi-layer nanolattice experiments, a snapshot from the in-situ experiment in Figure 3.3C shows that the low density layers shell buckle first. The effective Young's modulus of this regime was measured as 2.05 ± 0.11 MPa, with a strength of 68 ± 4.5 kPa. Despite the distribution of density in alternating layers, Figure 3.3D shows that every low density layer buckles before the first high density layer at the time the experiment reaches the transition region. After each low density layer is compressed, the high density layers begin to shell buckle one by one, as seen in Figure 3.3E, until the experiment reaches the prescribed strain. The effective Young's modulus of this

20

second regime was measured as 7.50 ± 0.72 MPa, with a strength of 360 ± 10 kPa. In-situ experiments showed the recoverability of this nanolattice after one cycle was 85%. A video of this experiment can be found as Supplementary Movie 2.

Diagonal Interface Nanolattice
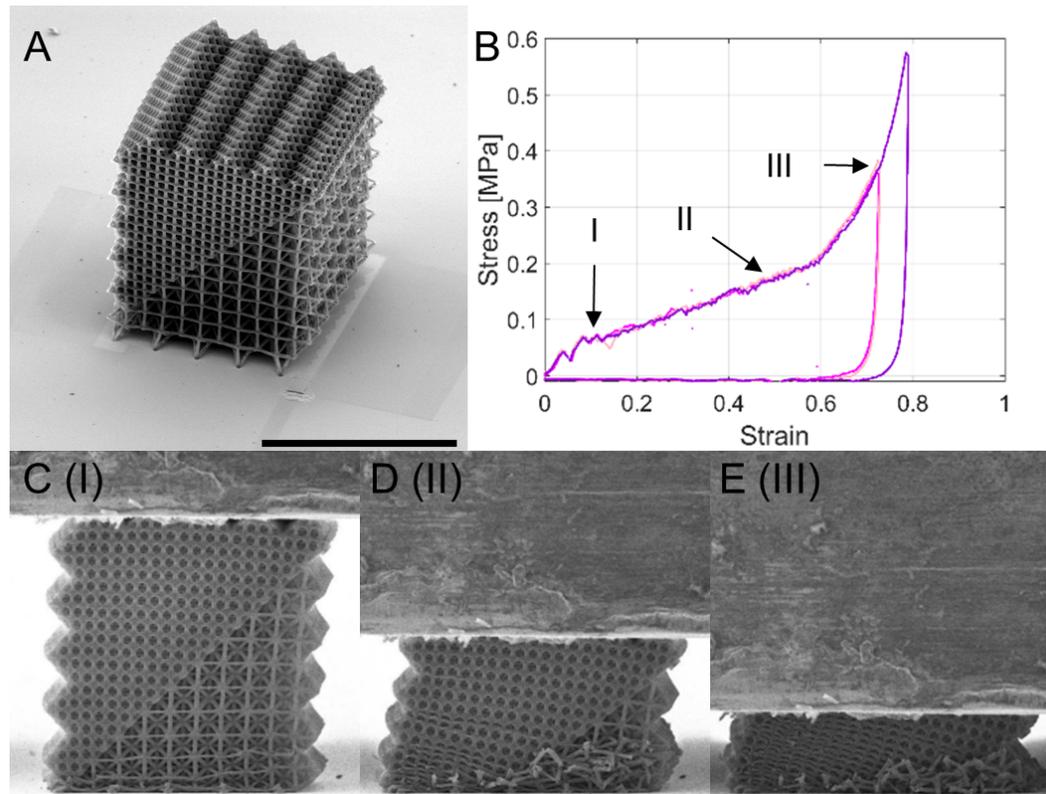
Figure 3.4: Diagonal interface nanolattice A) SEM image of the undeformed hollow structure. Scalebar is 100 µm. B) Ex-situ mechanical data. C-E) SEM images during in-situ testing at strains indicated by I, II, and III in B. The width of each image is 140 µm.

The diagonal nanolattice is illustrated in an SEM micrograph in Figure 3.4A, with corresponding ex-situ data in Figure 3.4B. In order to accommodate the diagonal design, there are triangular prisms without structural beams at the substrate and indenter interfaces and on two sides of the nanolattice. Figure 3.4C shows that the low density beams at the substrate interface shell buckle first, followed by the next layer comprised of only low density unit cells. The initial buckling due to the missing beams at the interface correlates to the first dip in stress in the stress-strain data. A video of this experiment can be found as Supplementary Movie 3. The effective Young's modulus of this first regime was measured as 2.26 ± 0.66 MPa,

with a strength beyond the initial dip of 70 ± 2.0 kPa. An image of the nanolattice compressed to the transition region of the other two nanolattices, approximately 0.45 strain, is found in Figure 3.4D. In general, this image shows that this diagonal nanolattice still exhibits layer by layer shell buckling. During the compression, layers that sit at the concave vertices of each block are the layers that shell buckle first, as this geometry likely causes the largest stress concentration. Due to the vast difference in density and strength, there is a slight moment created by the wedge of higher density material. As the nanolattice is further strained, a larger fraction of the undeformed material is comprised of high density unit cells. This is the likely cause of the effective strain hardening observed in the mechanical data. Figure 3.4E shows an image near full strain, where the low density region is completely compressed. The high density region is almost completely strained, except for a small region above the low density region, likely because of the localization of strain on the left half, which results in the right half being less constrained. The effective Young's modulus and strength of this high density region were not calculated, as there is no observed distinct linear region or yield point. The recoverability of this nanolattice was measured as 72% from one cycle of in-situ experiments.

Comparison of Varied Density Nanolattices
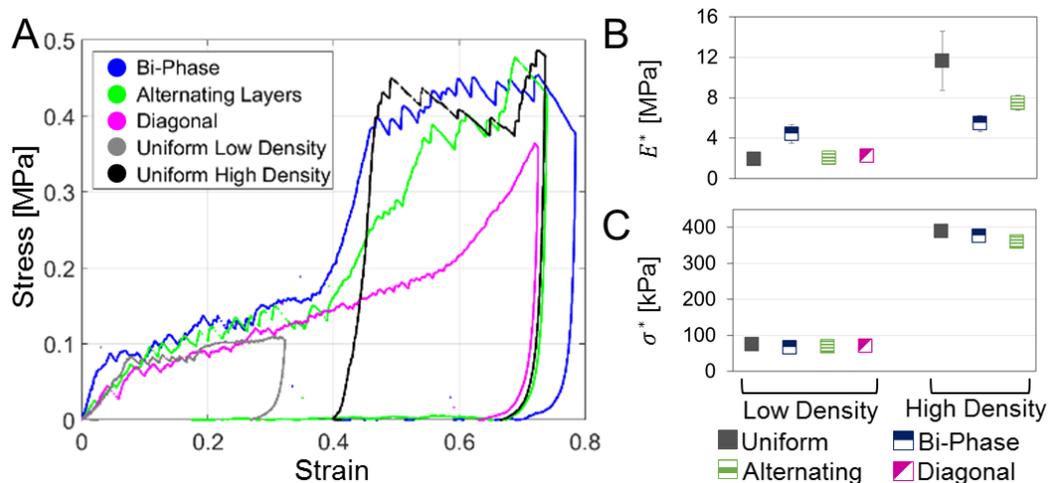
Figure 3.5: A) Comparison of the mechanical response of all 3 nanolattices compared to uniform density controls. The uniform high density data has been offset in strain for visual comparison. Summary of data from the low and high density regions of all structures for effective B) Young's modulus and C) strength.

Figure 3.5A compares the stress-strain response of each of the three varied density nanolattices, compared to the respective uniform nanolattices of each density. Since

the nanolattices are different heights, the strain is scaled to reference the 145 μm tall diagonal nanolattices for comparison, as they were the tallest after the full fabrication process. The low and high density region deformations of the bi-phase and alternating layer nanolattices match very well with their uniform density counterparts, in grey and black, respectively. The mechanical deformation of the diagonal interface nanolattice follows closely to the uniform low density nanolattice control in the low density region, but deviates from the other two graded nanolattices when they begin their transition to the high density region. Beyond this point, it exhibits modest strain hardening before a steep increase around 0.6 strain. This steep increase in slope is likely due to a larger fraction of the high density region being strained once all of the lower density unit cells are compressed. It should be noted that the stress values for roughly the second half of this experiment are likely lower than would be expected from true uniaxial compression, as there is a slight bending moment.

Figures 3.5B and C summarize the effective Young's moduli and strength, respectively, within the low and high density regions of the stress-strain curves from each nanolattice. The strengths of each region match well to the value of the corresponding uniform density control. This is expected, as yielding will occur when a sufficient stress is achieved within a layer and this stress for a given material, microstructure, and architecture can be related to only the density via Equation 3.2. This is not the case for the Young's moduli. During initial loading, only the lower density regions are effectively strained. After this initial loading, the higher density region is being strained in series with the compressed lower density region. The effective Young's modulus of a compressed uniform 16 μm nanolattice was calculated to be 10.7 MPa from the unloading slope of its stress-strain curve. Using a simple model for two springs in series:

$$\frac{1}{E_{eq}} = \frac{1}{E_1} + \frac{1}{E_2} \tag{3.3}$$

The expected equivalent Young's modulus of the uncompressed high density region that sits on top of the compressed low density region was 5.56 MPa. This matches well for the observed effective Young's modulus from the second linear region, which was 5.45 ± 0.80 MPa and 7.50 ± 0.72 MPa for the bi-phase and alternating nanolattices, respectively. The value for the alternating layer nanolattice may be slightly higher due to the effect of the interface between each layer. Since the density variation is evenly distributed throughout the volume, it's possible the high

density layers are in better mechanical contact with each other, resulting in a higher stiffness, compared to the mechanical contact between the large continuous high density block sitting on top of the compressed low density block in the bi-phase nanolattice case. The effective Young's moduli for the lower density region match fairly well, however the value for the bi-phase nanolattice is peculiarly high. This may be due to an unnoticed anomaly with these structures, but it could perhaps be due to the unique construction. It's possible that the single additional constraint at the top of the homogeneous low density region increases the stiffness in a way that the multiple constraints in the alternating density structure cannot. This effect of the boundary conditions could likely be evaluated using a finite element analysis (FEA) software with sufficient computing power. In contrast, the stiffness values match very closely for the uniform low density nanolattice and low density region of the alternating layer nanolattice, indicating that the multiple low-high density interfaces do not play a large role during the first half of the compression. Counterintuitively, this structure with a more uniform density distribution exhibits a more heterogeneous distribution in its regions' effective Young's moduli.

Deformation Behavior

Beyond this quantitative mechanical property comparison between the structures, their distinct architectural features contribute greatly to their deformation behavior. As mentioned previously, the low density region of the bi-phase structure is completely compressed before the high density region. This bi-phase deformation provides an entirely sacrificial region before the stronger higher density region is affected, which may prove particularly useful to maximize the lifetime of a particular product. Conversely, while the individual layers behave similarly, the alternating layer structure as a whole compresses uniformly, as the low density regions are distributed more uniformly. This uniform deformation could be a significant design feature for applications that require a more uniform compression response. For the diagonal interface structures, two architectural features lend unique properties. First, the missing diagonal half unit cells create stress concentrations that cause the layers at the vertices to shell buckle first before their surrounding layers. This illustrates that the architecture can guide the path of shell buckling, providing a route for directional deformation, even within one density region. Second, since the structure contains an increasing fraction of high density unit cells along its height, it gradually stiffens and becomes stronger. This gentler transition, which can likely be tuned by the angle of the interface, provides a greater degree of control over the

mechanical response of these structures. Additionally, this configuration results in a slight bending moment in the structure, which could provide deflection capabilities to this material.

3.4 Summary and Outlook

We demonstrate that with even a relatively simple binary density distribution, we can significantly tailor the mechanical deformation of hollow 3D architected nanolattices. We show that the strength for the low and high density regions of each nanolattice match very well to their respective uniform density counterparts, as would be expected. We also show that the effective Young's moduli of the low density regions match relatively well to that of the control sample. The stiffness of the high density region follows what would be expected from two springs in series, with the other spring as the compressed low density region. Additionally, a diagonal interface produces an initial response similar to the low density case, but a much more gradual transition to a higher density response. During deformation, we have shown that distributing the density variation in alternating layers creates a correspondingly distributed deformation, whereas a bi-phase variation in density results in the lower density half compressing entirely before the one with higher density. By varying the interface angle, we have shown that it is possible to modulate the transition between the two density regions. In general, this work illustrates that segments of different density can be combined together in different configurations in a nanolattice to produce a tailored mechanical response. This can provide a powerful tool for matching the stiffness, strength, exact stress-strain shape, and deformation characteristics for tailored applications, all while using only one chemical composition and architecture.

C h a p t e r   4

SIMULTANEOUS EXTREME ULTRA LOW-*K* IN STIFF, RESILIENT, AND THERMALLY STABLE NANO-ARCHITECTED MATERIALS

Adapted with permission from:

1. Lifson*, M. L., Kim*, M.-W., Greer, J. R. & Kim, B.-J. Enabling Simultaneous Extreme Ultra Low-k in Stiff, Resilient, and Thermally Stable Nano-Architected Materials. *Nano Letters* **17.** doi: 10.1021/acs.nanolett.7b03941, 7737–7743 (2017).

The previous chapter dealt with binary density gradients within nanolattices for tailoring mechanical properties and deformation as an example of the versatility of 3D architected structures in the mechanical property space. This chapter moves the discussion to electrically multifunctional materials. In particular, it discusses making improvements to dielectric materials that are ubiquitous in modern society, as they enable ever-advancing silicon integrated circuits (ICs) that power our computers, mobile cellular devices, and the internet.

4.1   Dielectric Capacitance

In 2018, approximately 95% of Americans own a cellphone, 77% of which are smartphones [62], which can contain dozens of highly specialized circuits that all rely on constantly improving semiconductor design, processing, and materials. Decreasing transistor sizes has aided in computing density and transistor gate delay, however this has also led to a sharp increase in the interconnect delay, which accounted for 39/41 ps (95%) of the total circuit delay at the 100 nm node, compared to 7/14 ps (50%) at the 250 nm node for aluminum metal and SiO_2 dielectric [63]. This interconnect delay is due to the capacitance created between the substrate and subsequent metal wiring layers. For a parallel plate capacitor, the capacitance is given by:

$$C = \frac{k\epsilon_0 A}{d} \tag{4.1}$$

where k is the relative dielectric constant, ϵ_0 is the free space permittivity, A is the plate area, and d is the plate separation. When a dielectric material is placed

between the plates of a capacitor, its internal polarization counteracts the applied electric field. This results in the need for additional charge to be stored on the capacitor plates for a given voltage (and electric field), which leads to an increase in the capacitance, since $C = Q/V$, where Q is the charge on the plates, and V is the applied voltage [64]. The higher the k value of the dielectric material, the larger the polarization and capacitance, which results in adverse effects for circuits, such as heating and timing losses. New ultra low-k ($k < 2.5$) materials are needed to replace the current dielectric materials in order to relieve these problems, particularly as technology nodes approach 14 nm, 7 nm, and below.

4.2 Ultra Low-k Dielectric Materials

Background

Designing and synthesizing low dielectric constant (low-k) materials has been a subject of intense research because of their potential use in high-performance technological applications like computer processing [65, 66], wireless communications [34, 67–69], and automotive radar [70]. Lowering the k of the interlayer dielectric decreases the resistance–capacitance (RC) delay, lowers power consumption, and reduces crosstalk between nearby interconnects, all of which pose significant issues for modern integrated circuits (ICs) [71–73]. The low-k property is also favored in low temperature cofired ceramic (LTCC) technology and represents the backbone of multi chip module (MCM) technology, which enables the integration of passive elements like inductors, resistors, and capacitors, which serve as building blocks for 3D circuits for the microwave/millimeter communications industry [74, 75]. For example, the antenna in a typical RF module for radiating/receiving radio waves requires the supporting substrate whose k is sufficiently low to prevent surface wave propagation and to increase the bandwidth [76].

Introducing controlled porosity into otherwise monolithic materials has been envisioned as a promising route for developing ultra low-k interconnect materials [77–83]. The selection of potential candidates for that is challenging because lowering the k of these materials through increasing porosity is often accompanied by the degradation of mechanical integrity, that is, a 77% reduction in Young's modulus after a 46% decrease in the density of bridged organosilicates [84] and a 4 order of magnitude reduction in the mechanical strength of silica aerogels measured via three-point flexural test when spanning 0–95% porosity [85]. Other properties also have been shown to degrade with introducing porosity; for example, the dielectric constant of a Sr–based metal–organic framework was reported to increase by 18%

over the temperature range of 0-350° C [86], the breakdown voltage field of porous SiCOH deposited using plasma enhanced chemical vapor deposition (PECVD) was reported to decrease from 5.5 MV/cm at 30% porosity to 3.6 MV/cm at 45% porosity [87], and the dielectric loss, *tan δ*, of polycrystalline alumina was reported to increase over 2 orders of magnitude when the porosity increased from 2% to 40% [88]. The deterioration of these properties can be attributed to large variations in aggregated particle and pore sizes, disordered pore distributions, and interconnected pores [89]. The low *k* of 1.25–1.36 have been attained in aerosols at high frequencies of 0.050–1.3 GHz and as low as 1.08 in the higher 11–12 GHz range [90, 91]. To date, no material with a *k* below 1.42 (at 1 MHz) whose mechanical properties were also investigated has been reported [82].

Fabrication

Figure 4.1 shows the fabrication process of capacitors that contain nano-architected dielectrics. First, a nanolattice with a horizontal top plate and overall dimensions of 128 μm × 128 μm planar top area and 8 μm height, a unit cell size of 4 μm, 300 nm major axis beam diameter, and 250 nm minor axis beam diameter was fabricated out of an acrylic polymer resin using two-photon photolithography (TPL) direct laser writing (DLW). This scaffold was written directly on a Au/Ti bilayer (80/12 nm) that had been previously evaporated on a Si wafer (1 mm × 1 mm), which serves as the bottom electrode (Figure 4.1a-b). This polymer nanolattice was then coated with a 10 nm thick conformal layer of alumina (Al_2O_3) using atomic layer deposition (ALD) (Figure 4.1c). Two opposing outer edges of the nanolattice were then removed by focused ion beam (FIB) milling, which uncapped the alumina coating on the outermost beams and exposed the interior polymer scaffold to be etched away in oxygen plasma (Figure 4.1d). An identical bilayer, Au/Ti (80/12 nm), was then evaporated as a top electrode on the top plate of the nanolattice to create a parallel plate capacitor (Figure 4.1e-h). Figure 4.1f shows a dark-field transmission electron microscopy (TEM) image and a SAD pattern of an individual alumina tube that demonstrate that the film is an amorphous matrix that contains ~5–15 nm nanograins.

4.3 Dielectric Properties of Hollow Alumina Nanolattices

To investigate the dielectric properties of the nanolattice, we measured the capacitance of nanolattices with unit cell sizes of 4 and 8 μm and total heights of 4 and 8 μm (see schematics and images in Figure 4.2). The capacitance was measured using
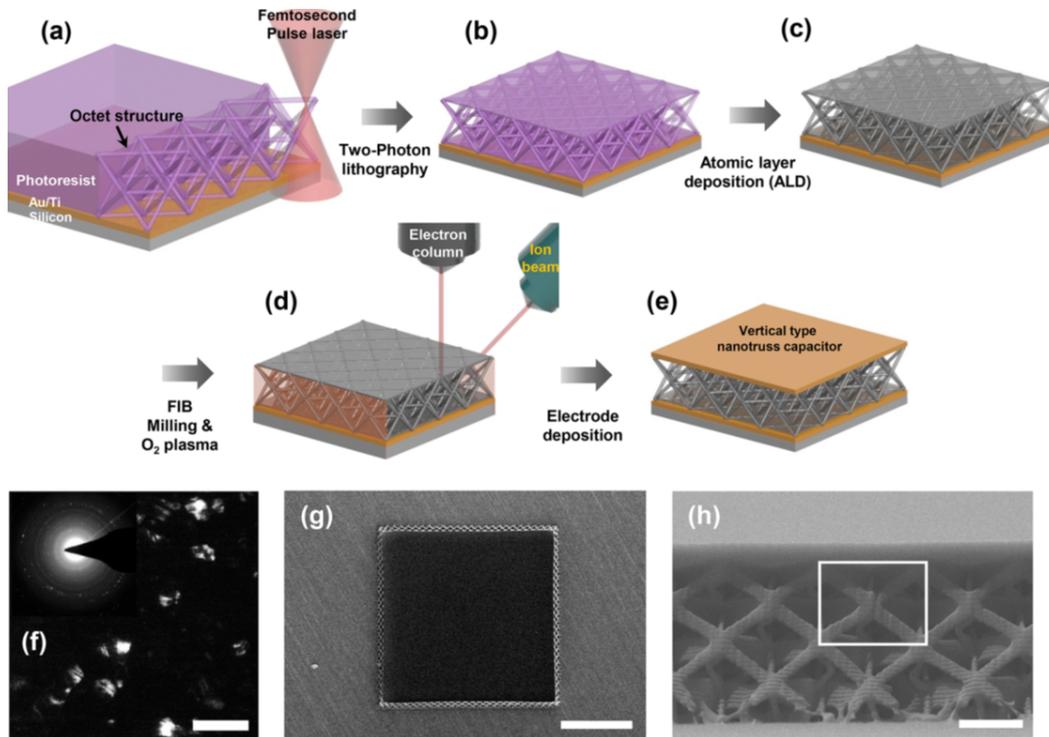
Figure 4.1: Schematics describing the manufacturing process of the nanolattice capacitor. (a and b) Fabrication of a polymer scaffold via two-photon photolithography (TPL) direct laser writing (DLW). (c) Alumina coating on the polymer nanolattice using ALD. (d) Removal of the polymer scaffold using FIB and oxygen plasma etching. (e) Deposition of the top electrode layer. (f) TEM dark-field image and SAD pattern of a single alumina tube. The scale bar is 50 nm. (g and h) Top- and side-view SEM images of the nanolattice capacitor (4 μm unit cell, 8 μm sample height, and 128 μm × 128 μm planar top), respectively. The boxed area indicates a unit cell. The scale bars of panels g and h are 50 and 3 μm, respectively.

a Keithley 4200–SCS impedance analyzer with the ability to control the temperature and probe the top surface of the nanolattice without applying forces (further details can be found in the Methods section of Reference [53]). Figure 4.3a-c shows capacitance density vs frequency plots of the fabricated samples, which convey that each nanolattice had a nearly constant capacitance density over the frequency range of 100 kHz to 10 MHz at an applied bias of 20 V. The data show that the 4 μm single-unit-cell-high 384×384 μm^2 top area sample had the highest capacitance density of 2.4 ± 0.25 pF; both the 4 μm double-unit-cell-high and the 8 μm single-unit-cell-high samples with top areas of 128×128 μm^2 had the capacitances of 1.17 ± 0.17 pF and 1.18 ± 0.14 pF, respectively. Figure 4.3d-f shows capacitance densities as a function of bias swept from $-V$ to $+20V$ at frequencies of 100 kHz, 1 MHz,
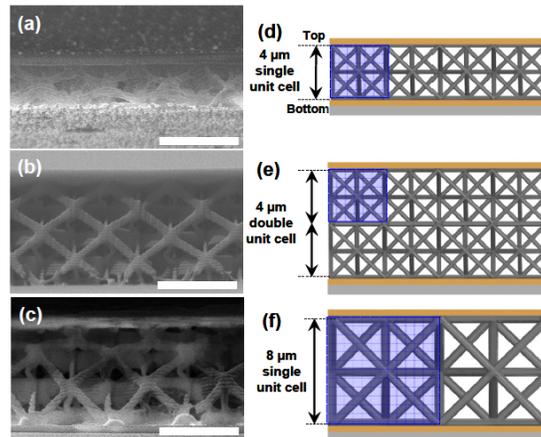
Figure 4.2: Images and schematics of nanolattice capacitors. SEM side view images of (a) 4 μm single unit cell layer, (b) double stacked 4 μm unit cell layers, (c) 8 μm single unit cell layer with (d-f) the schematics depicting their lattice geometries, respectively. The scale bars are 5 μm.
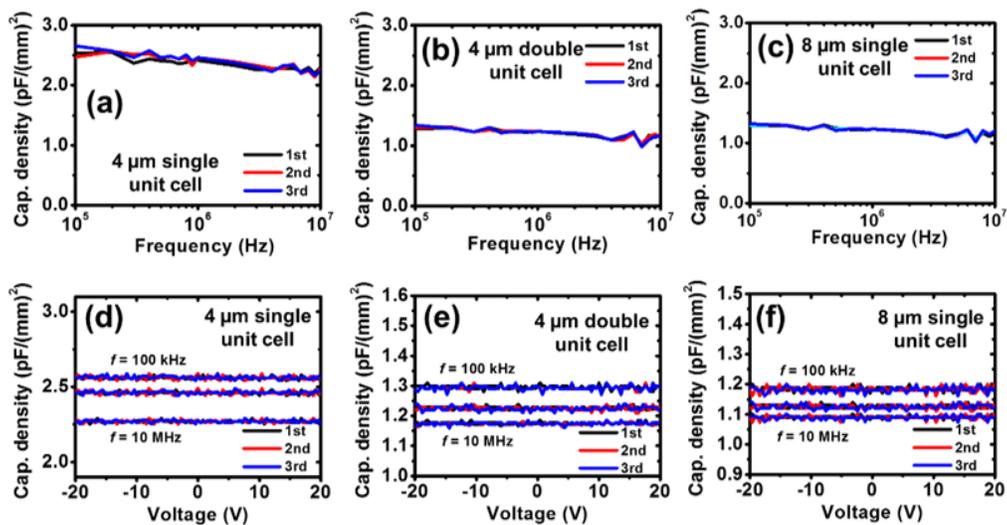
Figure 4.3: Dielectric properties of nanolattice capacitors. (a-c) Frequency dependence on the capacitance density of the three capacitors. (d-f) Voltage dependence on the capacitance density of the three capacitors.

and 10 MHz. These plots show that the capacitance densities were stable, with the dielectric losses of 0.034 ± 0.004 at 100 kHz, 0.026 ± 0.004 at 1 MHz, and 0.033 ± 0.005 at 10 MHz (dielectric loss data can be found in Reference [53]). The C–V

plots shown in Figure 2df were normalized by the relative capacitance as a function of applied voltage at varied frequencies to extract the voltage coefficients of capacitance (VCCs) [92], $(C - C_o)/C_o$, where C_o is the capacitance density at zero bias. These measurements revealed that VCCs were virtually nonexistent for all samples, which implies that the nanolattices are stable over this voltage range. Measurements of nanolattice capacitance over three experiments produced approximately identical data, as conveyed in the plots in Figure 4.3d-f.

We calculated the dielectric constant, k, for a parallel plate capacitor using the measured capacitance densities [93]:

$$k = \frac{Cd}{\epsilon_0 A} \tag{4.2}$$

where ϵ_0 is the dielectric permittivity in a vacuum (8.85×10^{-12} F/m), A is the footprint area of the electrode, d is the thickness of the dielectric layer, and C is the capacitance. To obtain the dielectric constant, the capacitance density (C/A) was inserted into Equation 4.2 with the proper thickness of the structure based on SEM images. To calculate the expected dielectric constant of the capacitor, we first calculated the relative density, $\overline{\rho}$, of the hollow nanolattices following the approach described in Chapter 2 and in detail in Reference [53]. The relative density of the nanolattices and the dielectric constant can be related through an analytical expression:

$$k = f_a k_a + f_m k_m = f_m(k_m - 1) + 1 = \overline{\rho}(k_m - 1) + 1 \tag{4.3}$$

where f_a is the relative fraction of air in the structure, f_m is the fraction of solid material (i.e., the volume of the shell on the hollow structure), which is equivalent to $\overline{\rho}$, k_a is the dielectric constant of air of ≈ 1, and k_m is the dielectric constant of the constitutive solid. The solid that comprises nanolattices in this work is ALD-deposited Al_2O_3 where the dielectric constant has been reported by Tapily et al. to be 8 [94]. Table 4.1 summarizes the dielectric properties measured and calculated using Equation 4.3 of nanolattices with different unit cell sizes and relative densities. It demonstrates that the lowest k of 1.06 was attained by the nanolattice with an 8 μm unit cell; the rest of the samples had indistinguishable dielectric constants of 1.10. We found that the measured and the calculated k's match well, and the marginal underestimation of the calculated k in capacitors with a 4 μm unit cell size is likely

caused by the small dimensional deviations in the periodic structure, which alters its relative density. These results suggest that the k of this material can be finely tailored by altering the relative density, following the relation in Equation 4.3.

Relative Density $\overline{\rho}$	Unit Cell Size [μm]	Area [μm^2]	Height [μm]	Measured Dielectric Constant [1 MHz -20V ~ +20V]	Calculated Dielectric Constant	Dielectric Loss [1 MHz -20V ~ +20V]
0.93%	4	128 x 128	4	1.10	1.07	0.034 ± (0.004)
1.0%	4	128 x 128	8	1.10	1.07	0.026 ± (0.004)
0.89%	8	128 x 128	8	1.06	1.06	0.036 ± (0.004)
0.93%	4	384 x 384	4	1.10	1.07	0.026 ± (0.003)

Table 4.1: Summary of calculated and measured dielectric constant and measured dielectric loss for different relative densities, sample height, and unit cell sizes.

4.4 Mechanical Properties of Hollow Alumina Nanolattices

The mechanical behavior of TPL-produced nanolattices has been extensively investigated and revealed their exceptional mechanical resilience [18, 52], insensitivity to flaws [51], suppression of brittle failure [49, 50], high tensile elasticity [47], and high strength-to-density ratio [48]. In cellular solids, the relative density uniquely defines the mechanical properties, that is, stiffness and strength, through a scaling relationship [18]. For example, the power law scaling of the effective Young's modulus as a function of relative density is:

$$E^* \propto \overline{\rho}^{\,n} \tag{4.4}$$

where n is empirically determined. The specific scaling of stiffness with relative density for hollow alumina nanolattices has been reported to have an exponent, n, of 1.61 [18]. Figure 4.4a shows a representative stress vs strain plot of an octet geometry Al_2O_3 hollow-beam nanolattice with a relative density of 1.3%, a unit cell size of 5 μm, major axis beam diameter of 1.48 μm, minor axis beam diameter of 0.37 μm, and alumina shell thickness of 10 nm during a uniaxial compression experiment [18]. To obtain accurate deformation characteristics, stiffness, and strength, the overall dimensions of samples for the compression experiments were 20 μm × 20 μm × 25 μm, which are factors of ~3 and ~6 taller than those made for the capacitors. Load data from the nanoindenter were converted into stress by dividing it by the contact area of the sample, and displacement was converted

to strain through normalizing by the sample height. The slope of the unloading portion of cyclic stress-strain data was averaged to calculate the structural stiffness, or effective Young's modulus, E^*, of the nanolattice, and the first peak in the data that corresponds to the initial layer buckling event demarcates the effective strength, σ^*. The data in Figure 3a reveal an E^* of 30 MPa and σ^* of 1.07 MPa, as well as ~98% shape recovery when strained to >50%. This stiffness of 30 MPa at a relative density of 1.3% in the alumina nanolattices is roughly 2 orders of magnitude greater than that of similarly dense ultralight foams, e.g., silica aerogels, whose modulus has been reported to be 100 kPa at approximately 1% relative density [95]. The structural order provided by the octet architecture of the nanolattices in this work enables an improved utilization of the constituent material to create samples that are 2 orders of magnitude stiffer than stochastic foams at similar relative densities [16]. The ability of this brittle material to recover after compression is enabled by shell buckling in the beams, a recoverable instability, which is determined by the wall thickness-to beam diameter ratio, t/a [18]. These results point to the mechanical resilience of the nanolattices even at relative densities of $\leq 1\%$, a regime where other porous materials permanently deform. Since the dielectric constant of architected materials appears to be governed by the intrinsic dielectric constant of the solid material that comprises it and the relative density, one can expect little change to k after recovery. It is also important for these nanolattices to support large voltage differences without initiating electrical breakdown. An investigation of the changes in breakdown strength during mechanical compression can be found in a following section.

Figure 4.4b shows a plot of Young's modulus vs dielectric constant for several existing low-k dielectrics, with hollow alumina nanolattices in this work marked as a filled diamond symbol. The relationship between effective Young's modulus and relative density shown in Equation 4.4 and the one between the dielectric constant and relative density (Equation 4.3) allow us to postulate an analytical relationship between the dielectric constant of hollow alumina nanolattices and their stiffness:

$$E^* \propto \left(\frac{(k-1)}{(k_m - 1)} \right)^n \tag{4.5}$$

The dashed contour in Figure 4.4b presents the solution of Equation 4.5 using the appropriate parameters for the hollow alumina nanolattices. This boundary represents the available parameter space where it is possible to fabricate hollow alumina nanoarchitectures whose combined dielectric constant and effective Young's modu-
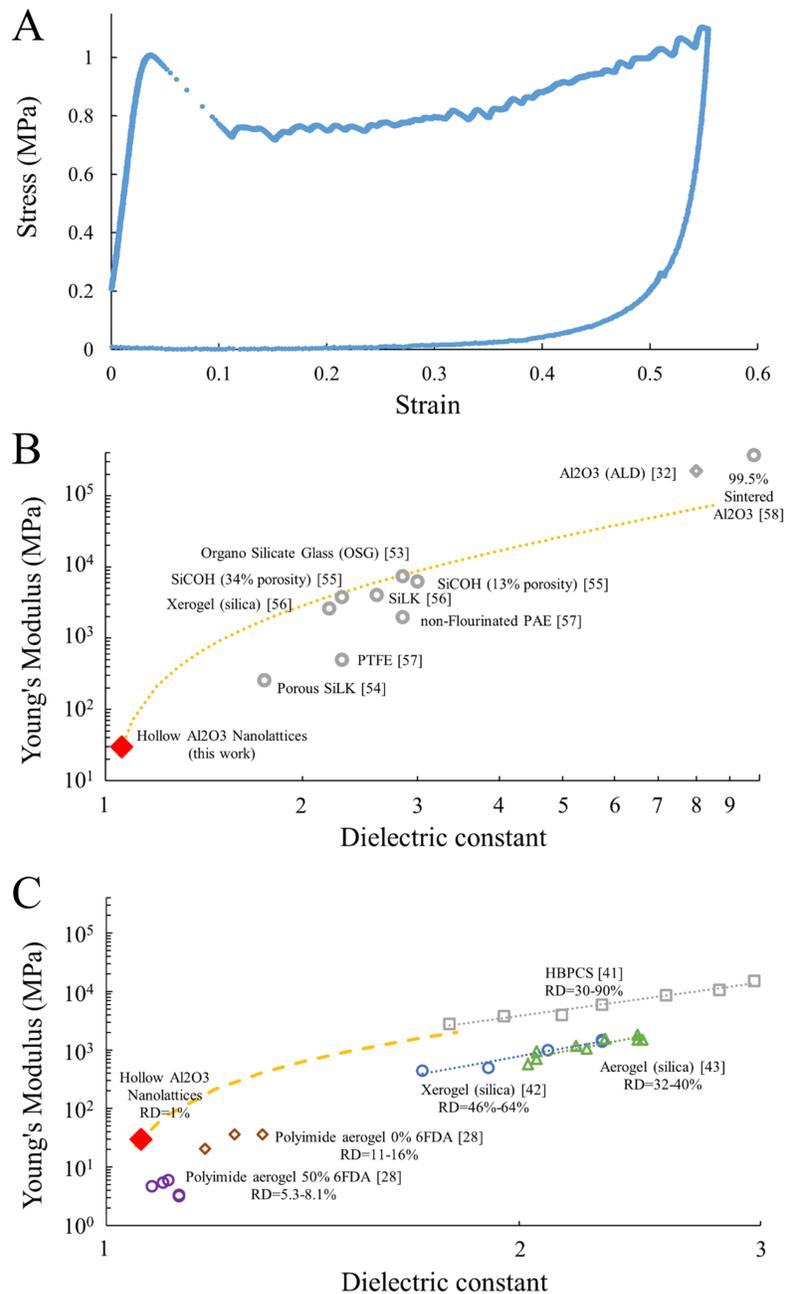
Figure 4.4: Mechanical properties of a representative nanolattice and correlation with its dielectric constant compared to other low-k materials. (a) Representative strain vs stress plot of a hollow alumina nanolattice provided by Dr. Lucas R. Meza. (b and c) Young's modulus vs dielectric constant plots of the nanolattice compared with other low-k materials. Please see Reference [53] for corresponding references in this figure.

lus outperform all other existing materials that have been reported to date in the low-*k*

($k < 3.9$) and ultra low-k ($k < 2.5$) regimes in the 100 kHz to 10 MHz frequency range. To further illustrate the unique position of nano-architected materials, Figure 4.4c compares the hollow alumina nanolattices to several other material systems whose porosity can be varied through processing: hyperbranched poly(amidoamine) conjugated silica (HBPCS) (RD 30-90%) [96], silica xerogel (RD 45-64%) [97], silica aerogel (RD 32-40%)[98], and polyimide aerogel with varying amounts of 2,2-bis(3,4-dicarboxyphenyl)-hexafluoropropane dianhydride (6FDA) in the backbone of the polyimide (0% 6FDA RD 11-16%, 50% 6FDA RD 5.3- 8.1%) [91]. The dashed contour represents the same scaling as one shown in Figure 4.4b for nanolattices with relative densities between 1% and 10%. The data points and trend lines for other reported material systems represent their corresponding scaling of stiffness with dielectric constant for the range of relative densities that have been attained using their respective fabrication techniques. The scaling law factor, n, for hyperbranched poly(amidoamine) conjugated silica (HBPCS) [96], silica xerogel [97], and silica aerogel [98], was calculated to be 2.43, 3.51, and 4.67, respectively. This is in contrast to the scaling law for the hollow alumina nanolattice, which has $n = 1.61$ [18]. This lower scaling law factor explains why the hollow alumina nanolattice can maintain its mechanical properties to a larger degree with decreasing relative density than the other porous materials mentioned above. The two sets of polyimide data have different formulated numbers of repeat units in the oligomers, as well as the total polymer concentration in the precursor solution, which prevents accurate formulation of the scaling. These polyimide data were taken at 11-12 GHz, well above the 1 MHz frequencies used in other studies. It has been observed that most materials exhibit lower dielectric constants at higher frequencies, as the orientation polarization typically vanishes around 1 GHz with increasing frequency [73, 99]. The relative densities of each shown material system are also depicted in the plot. This landscape conveys that (1) the dielectric constant of 1.06 for the hollow alumina nanolattices is extremely low for this frequency regime and (2) the Young's moduli of these nanolattices is at least an order of magnitude greater than what has been observed in insulating materials at such low porosity.

4.5 Frequency, Voltage, and Temperature Stability

To investigate the dependence of the dielectric constant on temperature, we first measured the capacitance densities of an 8 μm unit cell nanolattice at a constant frequency of 1 MHz while spanning the applied voltage from -10 V to +10 V. The measurements were carried out in an isothermal condition with the temperature

varying from 25 to 800° C. Figure 4.5a shows the capacitance density vs voltage
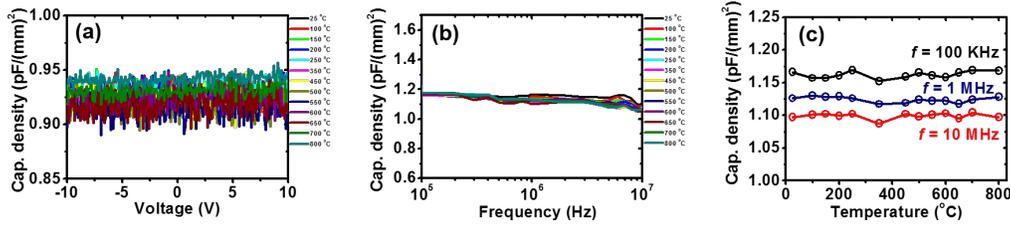
Figure 4.5: Temperature stability of the nanolattice capacitor with 8 μm single unit cell layer. (a) Capacitance density vs voltage plots at varied temperatures (25-800° C). (b) Capacitance density vs frequency plots at varied temperatures. (c) Capacitance density vs temperature plots at 100 kHz, 1 MHz, and 10 MHz.

at several representative temperatures during this experiment. The data indicate that capacitance densities were virtually constant, 0.925 ± 0.025 (pF/mm^2), and the extracted VCCs from all the measured capacitances across all temperatures were approximately zero. We also measured the variation of capacitance density as a function of frequency at different temperatures (25-800° C) as shown in Figure 4.5b, which demonstrates that the effect of temperature on capacitance density is negligible. We observed small dielectric losses within the range of 0.01-0.1 over the entire range of tested frequencies, temperature, and voltage (see Reference [53] for more details).

The dielectric constant of nanolattices was calculated to be 1.06 ± 0.05 using the measured capacitances at the applied temperatures and frequencies, as depicted in Figure 4.5c. The temperature dependence of the relative dielectric constant is usually quantified by the temperature coefficients (TCKs) defined as [100, 101]:

$$TCK = \frac{\Delta k}{k_{RT}\Delta T} \tag{4.6}$$

where Δk is the change in relative dielectric constant with respect to the reference dielectric constant at room temperature, k_{RT}, and ΔT is the change in temperature relative to the reference temperature. The TCK of the nanolattice was calculated to be 2.43×10^{-5} K^{-1}. The dielectric constant of a polycrystalline alumina film is strongly temperature-dependent: k increases by a factor of ~1.3 when temperature increases from 300 to 400 K [102]. The thermal conductivity of materials generally decreases with introducing porosity; for instance, the thermal conductivity of bulk alumina is ~0.17 W/cm K, and that of ~75% porous alumina is ~12 times lower, at 0.014

W/cm K [103]. The observed high temperature stability exhibited by the alumina nanolattices in this work likely stems from the low thermal conductivity of these percolating ultralow-density nanoarchitectures. This stability can have significant beneficial impact for microprocessors and devices whose circuits undergo thermal fluctuations caused by the heat that is released during their operation or from the environment. It is also a stark contrast to ultra low-k organic polymers ($k \leq 2$), which suffer from severe restrictions in thermal processing because they decompose at low temperatures [77, 104–106].

4.6 Phenomenological Electrical Breakdown Behavior

This section adapted with permission from:

1. Kim, M.-W., Lifson, M. L., Gallivan, R. A., Greer, J. R. & Kim, B.-J. Breakdown Behavior of Extreme Ultra Low-k Nano-Architected Materials. *In Preparation* (2019).

Electrical Breakdown Data
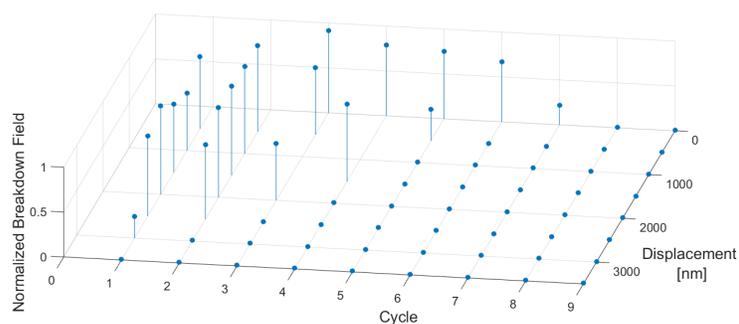
Figure 4.6: Electrical breakdown field data by displacement during cyclic experiment.

Our collaborators at the Gwangju Institute of Technology (GIST) have performed initial electrical breakdown measurements on a single unit cell tall nanolattice capacitor that we fabricated at Caltech using an identical process as described in this chapter. This measurement consisted of compressing a 128 μm x 128 μm x 8 μm nanolattice with a conductive probe in 500 nm increments under an optical microscope and performing a voltage sweep at 0.16 V/s while measuring current at each displacement. Displacement was applied up to 3500 nm before being removed in the same increments until reaching the initial height. This was repeated for 9 cycles. Electrical breakdown was defined as the first sudden increase of at least one order of magnitude in measured current. A 3D representation of this data,

normalized to the maximum breakdown field observed during the experiment, can be found in Figure 4.6. It should be noted that missing data points indicate no breakdown was observed during voltage sweeps at the particular configuration.

Breakdown was not observed for zero displacement of the first two cycles due to the maximum voltage limit of the experiment. Beyond this very first part of the breakdown, where initial non-recoverable deformation is likely to occur, three main qualitative observations can be made from this data. First, within each cycle, the value of the breakdown field is relatively constant until the experiment reaches a displacement at which the breakdown occurs immediately, indicating the material can no longer sustain a potential difference across it. Second, the material regains the ability to sustain a voltage upon unloading; however, the field at which the material experiences electrical breakdown occurs at lower values with increasing cycles. Third, the displacement at which this electrical breakdown occurs decreases with increasing cycles.

Finite Element Analysis Model

It has been shown that DC conduction of Al_2O_3 at high electric fields can be described by a space charge limited conduction (SCLC) model [107, 108]. In the SCLC model, electrons or holes are injected into the material via the electrodes and alter the local space charge distributions. This can create a conducting filament within the material such that the local internal electric field exceeds the breakdown voltage. The first conducting filament to bridge the two electrodes causes global electrical breakdown of the material, characterized by a drastic increase in measured current.

While calculating the breakdown voltage value for a given experiment is difficult, we can assume there will exist some internal electric field at which the material will exhibit breakdown. In order to better visualize this breakdown phenomena, we created a phenomenological model with corresponding qualitative FEA figures in COMSOL multiphysics 5.3 (COMSOL Inc.) to estimate the local electric field (with units V/m) within the architected material. We modeled a stationary 2D slice of the hollow ceramic nanolattices with the voltage difference between the terminal and ground as 100 V using the electrostatics package. The terminal and ground were designated as the top and bottom boundaries, respectively, and were specified using the default material parameters for gold. The 10 nm shell members were designated as alumina with an $\epsilon_r = 8$ [94], with the remaining dielectric as the

default software settings for air ($\epsilon_r = 1$). The model involves solving both Gauss' law and the electrical potential equation:

$$\nabla \cdot \boldsymbol{D} = \rho_V \tag{4.7}$$

$$\boldsymbol{E} = -\nabla V \tag{4.8}$$

where $\boldsymbol{D}$ is the electric flux density, ρ_V is the volumetric charge density, $\boldsymbol{E}$ is the electric field, and V is the electric potential, or voltage.

(a): Undeformed   (b): Beam Bending

(c): Partial Beam Buckling   (d): Full Beam Buckling

(e): Half Unit Cell Displacement
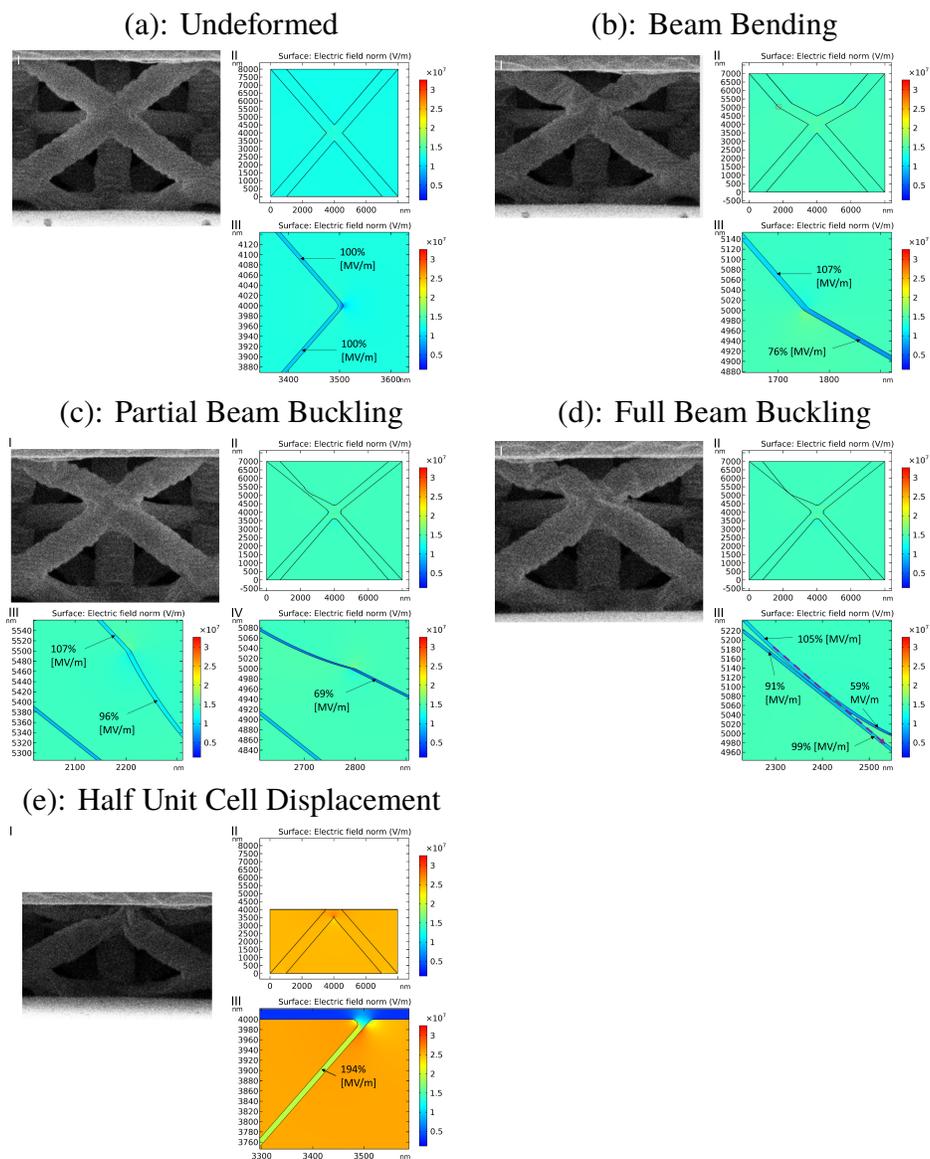
Figure 4.7: Five deformation scenarios modeled with FEA.

We modeled five geometric cases to match mechanical behavior observed during cyclic testing of these structures in SEMentor that can be found in Figure 4.7. Each case has a corresponding SEM image labeled I and a low magnification FEA image showing the norm of the electric field in the image labeled II. The red rectangle on each image labeled II can be found magnified in panel III. If there is also a blue rectangle, this can be found in panel IV. The initial undeformed case can be found in Figure 4.7a. The local electric field within the undeformed beam above and below the node is equal and will be labeled 100%. Next, we explored 3 intermediate deformation mechanisms, all occurring around 1000 nm of displacement. The first of these mechanisms is beam bending, which can be seen in Figure 4.7b. Here, both walls of the hollow tube bend and remain roughly parallel. Our model shows that the local electric field is higher above the point of bending in the shell and lower below this point. The lower half of the unit cell has a field that is 110% of the original, which is simply caused by the decrease in plate separation while maintaining the same voltage. This does not lead to an increased pathway of higher electric field, and thus is not likely a contributor to decreasing the required breakdown field. The second deformation case is partial beam buckling, as shown in Figure 4.7c. This case shows a similar effect to the previous: the local electric field is slightly higher above the initiation of buckling and slightly lower below it. The lower half of the unit cell also has a field that is 110% of the original. As before, there is no continuous pathway of increased electric field, which would result in greater breakdown susceptibility. The final intermediate deformation case is full beam buckling in Figure 4.7d. This can occur after repeated cycles where the hollow tube fails to recover its original shape. In this scenario, the higher electric field in the top shell above the wrinkling vertex comes into contact with the relatively unchanged electric field of the bottom shell below the vertex. As before, the lower half of the unit cell has a field that is 110% of the original. This scenario does create a potential continuous pathway of increased electric field, which can result in an effective lower breakdown strength. The final scenario in Figure 4.7e describes the geometry at the maximum displacement of the experiment. Here, the conductive tip comes into contact with the plane of nodes that are positioned at roughly half the height of the structure. This effectively removes the entire pathway along the top half of the structure and creates a direct pathway between the tip, the shell below the node, and the substrate, while the applied field is simultaneously higher due to a decreased plate separation. The FEA model predicts an internal field in this shell that is almost 2 times what was found in the undeformed case.

Applicability of the Model to the Breakdown Data

This fairly simple qualitative model can lend us insight into the three main observations from the electrical breakdown data. For the first point, the binary nature of the breakdown response within a cycle could be explained by the fact that there is not a continuous pathway with an increased local electric field created by a beam bending or partial beam buckling scenario, but there is a pathway with a significantly increased field once the tip is in contact with the node halfway down the structure. Within this first cycle, the material behaves as a switch: it either breaks down according to the structural breakdown strength or as a short circuit. In the second observation, the material regains most of its breakdown strength for a given displacement because of the mechanical recoverability in the material, however it likely decreases slightly with increasing cycles as an increasing number of beams become fully buckled and no longer recover. This full buckle beam scenario does allow for a pathway of increased continuous local electric field. Similarly, the third observation that the displacement at which electrical breakdown occurs decreases with increasing cycles could be explained by the fully buckled beams. With increasing cycles, as the displacement increases, there exists a higher probability that there is a conductive pathway that exceeds the breakdown strength, likely passing through the node of the touching shells in the fully buckled beam.

Summary of Breakdown Observations

As we delve further into exploring the electrical properties of multifunctional materials, this investigation gives us some initial insights into the unique electrical breakdown behavior and recoverability of hollow alumina nanolattices. Beyond the initial displacement and for small strains, this material maintains a quite stable dielectric breakdown strength and, within a few cycles, the material recovers a substantial portion of its breakdown strength for a given displacement. These features could provide potential resilience to devices needed to withstand several mechanical shocks. Finally, this simple model suggests that it may be possible to utilize breakdown voltage as a diagnostic tool to characterize the mechanical integrity of architected dielectric materials.

Varied Density Effect Investigation

Beyond understanding the effects during the deformation of a single nanolattice, we are also investigating the influence of the configuration of the conduction pathway through the structure on its breakdown performance. To do this, we have created
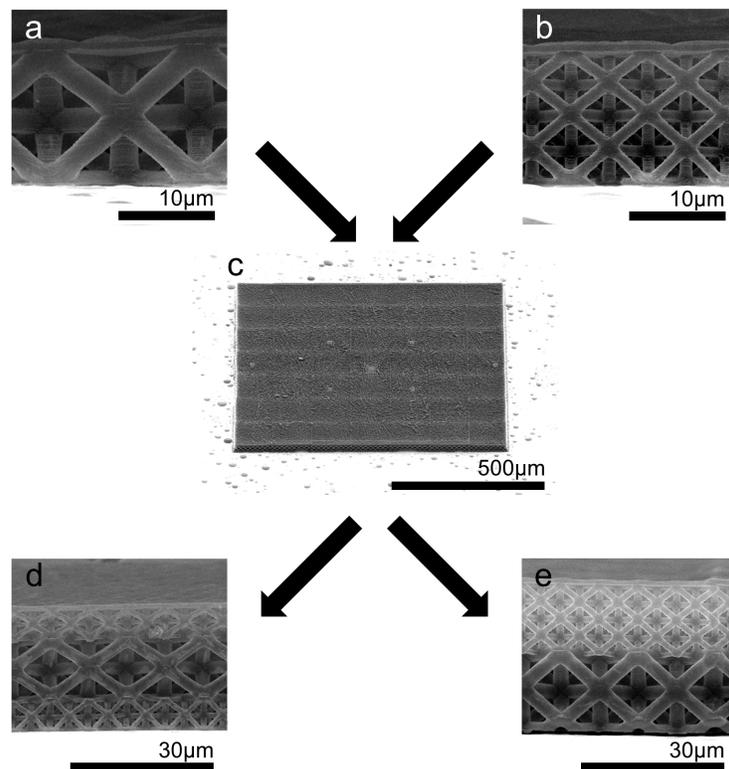
Figure 4.8: Introducing varied density into nanocapacitors. a) 16 μm unit cells can be combined with b) 8 μm unit cells into a c) nanolattice capacitor to create an d) alternating layer nanolattice or a e) bi-phase nanolattice.

four different types of nanolattices: two uniform density nanolattices with 16 μm and 8 μm unit cells, and two varied density configurations, with an alternating layer and bi-phase nanolattice. These can be found in Figure 4.8. The fabrication for this endeavor followed the method and design of the previous chapter. Structures were stitched together in the x-y plane to create designed 640 μm x 640 μm x 16 μm uniform density nanocapacitors or 896 μm x 896 μm x 32 μm varied density nanocapacitors. The larger area was utilized to maintain similar capacitances between all samples for dielectric constant measurement sensitivity.

4.7 Practical Considerations

We have shown this 3D architected dielectric material possess extraordinary ultra-low k properties, with great stability over a variety of variables, but can it be practically applied to the stated problem of reducing capacitance within integrated circuits? There are several drawbacks that need to be considered. First and foremost,

the throughput of current TPL technology will likely not meet the very cost and time sensitive demands of the semiconductor industry. However, highly-specialized applications that are particularly sensitive to capacitance and maintaining mechanical stiffness may yield a cost-effective use of this technique. Additionally, future advances in AM techniques may enable fabrication of materials with similar feature sizes, but at high throughput, such as mask exposure with a roll-to-roll process. Second, a common drawback of low-k materials is their low elastic moduli, which can limit their mechanical applications and complicate the physical wafer processes such as chemical mechanical polish (CMP). SiLK, a Dow Chemical Company commercial low-k ($k \approx 2.7$) polymer that has been used in industry has been shown to exhibit a Young's modulus of around 4 GPa [109]. Others have suggested that an elastic modulus of 3 GPa or higher is necessarily for uniform planarization during CMP [110]. As described in Equation 4.5 and illustrated in Figure 4.4b-c, we can tune the effective stiffness through the relative density to meet this criteria. As shown in the figure, this scaling represents a lower k value for a given stiffness for currently available materials, which should enable better dielectric properties for a given process requirement. Third, hollow alumina nanolattices have been shown to exhibit extremely low thermal conductivity [21]. As the device spacing and metal linewidths decrease, the ability of the dielectric to carry heat away from the active layer of the circuit becomes increasingly important [111]. While lowering the k value can reduce the amount of heat generated due to capacitance, this benefit may be reduced or erased if the temperature of the devices increases during operation, which can limit their performance. Fortunately, the drive towards thinner silicon and through-silicon vias (TSVs) over the last decade provide additional pathways to remove heat from devices from the backside of the wafer [112, 113]. Finally, porosity can provide pathways for moisture and impurities to affect the fabrication and performance of ICs. In order to combat this, porous dielectric materials can be coated, such as with initiated chemical vapor deposition [114] to seal off the porosity from further processing steps. In summary, while there are drawbacks and costs to using this material in ICs, current and future technologies could be utilized to avoid or mitigate these risks, particularly in situations where capacitance and mechanical resilience are crucial. We believe this work represents not only an insight into the fundamental dielectric properties of architected materials, but a potential practical solution for reducing capacitance in specialized applications.

4.8   Summary

We demonstrate a fabrication process to create parallel plate capacitors with three-dimensional hollow alumina nanolattices as the dielectric layer. These 3D nano-architected materials, created using two-photon lithography (TPL) and atomic layer deposition (ALD), had an octet unit cell size of 4 or 8 μm, 300 nm major axis beam diameter, and 250 nm minor axis beam diameter and an alumina shell thickness of 10 nm. Directprobing electrical measurements of the capacitors revealed the dielectric constant of the nanolattices, k, to be 1.06 at a frequency of 1 MHz; uniaxial compression experiments revealed their effective Young's modulus to be 30 MPa, a value 300 times higher than that of other equivalently porous dielectrics [95]. This combination of extremely low-k and high stiffness places these 3D nano-architected materials into previously unattainable white space, outperforming all other materials that have been reported to date in the low-k and ultra low-k regimes in the 100 kHz to 10 MHz frequency range. We found the dielectric constant to be stable over -20 V to +20 V range, 100 kHz to 10 MHz frequencies, and 25-800° C temperatures. These structural meta-materials also offer mechanical resilience as revealed by their shape recoverability after being compressed by 50% strain. These hollow alumina nanolattices are also very temperature-insensitive and chemically stable, which provides them many processing advantages over other materials currently being investigated. We believe that the nanolattice capacitors described in this work provides a new efficient pathway to resolve the long-standing problem of mechanical integrity, thermal stability, and electrical reliability of ultra low-k applications.

C h a p t e r   5

FACILE TECHNIQUE FOR THE FABRICATION OF 3D ARCHITECTED PIEZOELECTRIC MATERIALS

Adapted with permission from:

1. Yee*, D. W., Lifson*, M. L. & Greer, J. R. Additive Manufacturing of 3D Architected Multifunctional Metal Oxides. *In Preparation* (2019).

The previous chapter demonstrated a promising application of 3D nano-architected materials for the passive electrical multifunctional role of ultra low-*k* dielectric materials. This chapter will shift the focus to the active electrical function of piezoelectricity and its exciting applicability to architected materials. Before delving in further, a brief summary of the piezoelectric mechanism and custom measurement system will be presented.

5.1   Piezoelectric Mechanism
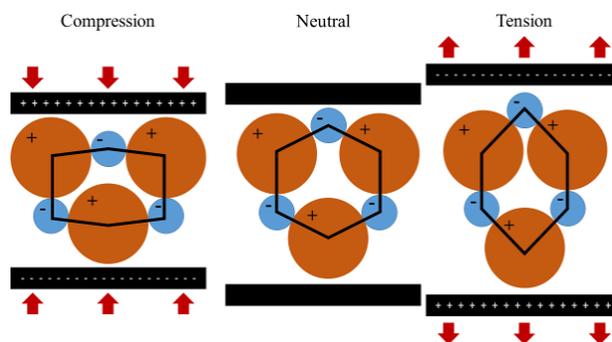
Figure 5.1: Schematic describing the piezoelectric mechanism. Piezoelectricity is caused by an anisotropy in the crystal structure. When in a neutral state, such as the middle panel, there is no net charge or polarization. Upon compression or tension, this lack of inversion symmetry causes a polarization, creating a net charge.

Piezoelectric materials are those that generate an accumulated electrical charge when a mechanical stress is applied or generate internal mechanical strain in response to an applied electrical field. These phenomena are termed the direct and converse piezoelectric effect, respectively. Piezoelectricity was first discovered by the Curie brothers in 1880, and Woldemar Voigt mathematically related the phenomena to the

20 natural crystal classes that exhibit the direct piezoelectric effect in 1910 [115]. These crystal classes exhibit no inversion symmetry, as the piezoelectric effect is caused by an anisotropic response in the charge distribution within the crystal lattice, as demonstrated in Figure 5.1.

This linear phenomena can be described as the combination of Hooke's Law for linear elastic materials:

$$S = sT \tag{5.1}$$

where S is strain, s is compliance, and T is stress, and the linear behavior of the material:

$$D = \epsilon E \tag{5.2}$$

where D is the electric charge density displacement, ϵ is permittivity, and E is the electric field strength. These equations can be combined into the two following intensive coupled equations:

$$S = s^E T + dE \tag{5.3}$$

$$D = dT + \epsilon^T E \tag{5.4}$$

where d is the piezoelectric constant, s^E indicates compliance under short circuit conditions, and ϵ^T indicates independence with stress [116].

These electromechanically coupled systems are useful in a variety of applications. Historically, piezoelectric devices were first commercially developed to generate acoustic waves in order to detect submarines at the end of WWI, and later as depth sounding devices [117]. The first frequency-stabilizing device using piezoelectric material for communications was proposed in 1921 by W. G. Cady [118]. In 1927, it was demonstrated that quartz crystals could provide a frequency standard upon which to base timing devices with significant improvement over mechanical methods [119]. These devices were predominantly used by scientific institutions and the military until semiconductor manufacturing processes had enabled economical incorporation of piezoelectric materials (initially with quartz) in the 1970s. This brought piezoelectric resonators into the household, as they became the timing standard for wristwatches [120]. As the ability to fabricate synthetic single crystalline quartz and other piezoelectric materials continued to grow, so too did their applications. Piezoelectric materials have since been used in high frequency ultrasound transducers for biomedical imaging [121], force sensors [122], resonator sensors to measure density, liquid level, film deposition thickness, and temperature [123], surface and bulk acoustic wave (SAW and BAW) filters [124], power harvesting

devices [125], and actuators for precise nanoscale positioning, such as in modern scanning probe microscopes [126]. Continuously shrinking technology has recently been shown to enable finer resolution applications, such as intravascular ultrasound, fingerprint sensors, and wireless power systems [127].

The remainder of this work will focus on the fabrication and characterization of two intrinsic piezoelectric materials. These are in contrast to ferroelectric materials, where the internal material polarization can be reversed in an external electric field. In particular, this work will discuss α quartz (SiO_2), with trigonal symmetry in point group 32 and a d_{11} of 2.3 pC N^{-1}, as well as zinc oxide (ZnO), with a wurtzite crystal structure in the 6*mm* crystal class and a d_{33} of 12.4 pC N^{-1} [116]. Before discussing these particular efforts, we will explain the piezoelectric measurement method we developed for these experiments.

5.2   Piezoelectric Measurement

Historically, the majority of piezoelectric measurements on nanomaterials have been performed using Piezoresponse Force Microscopy (PFM), which is essentially an additional electrical measurement capability built into an Atomic Force Microscope (AFM). These experiments have been performed on ZnO nanowires, for example, to measure the converse piezoelectric effect at frequencies in the double to triple digit kHz [128–130]. Since the AFM is used to profile the height variations across samples, they typically utilize very sharp Berkovich or pyramidal tips attached to the AFM cantilever. This sharp geometry can create significant concentration of both the electric and stress field on the sample and has been cited as a source of error, making reliable calibration of these experiments difficult [129]. Several studies have been performed using a quasi-static commercial nanoindentation system (Hysitron Triboindentor TI 950); however, these studies also use sharp Berkovich tips, which do not eliminate the concerns with tip geometry [131, 132]. While this technique enables attempts at measuring the direct piezoelectric response, it requires very high strain rates, which may influence the mechanical response of the material and calibration of the measurement.

In order to avoid these concerns and measure the direct piezoelectric effect at low frequency, we built a custom piezoelectric measurement system within the group's in-situ nanomechanical instrument. A schematic of this custom system can be found in Figure 5.2.

An optical image of inside the SEM chamber can be found in Figure 5.3. The sample
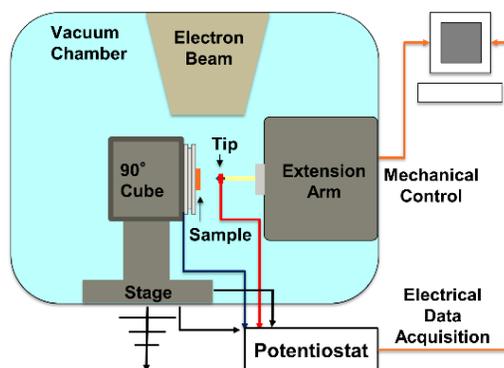
Figure 5.2: Schematic of the electromechanical experimental setup. The sample is placed on an aluminum stub, mounted at 90°, in an SEM chamber equipped with a nanoindenter arm. A potentiostat is connected to measure the open circuit voltage between the grounded stage and the indenter tip during the experiment.

is mounted onto an aluminum SEM stub using colloidal graphite (Ted Pella, Inc.), which is then mounted into a 90° SEM cube. This is attached to the stage such that the electron beam (e-beam) is viewing the cross section of the sample. The conductive flat punch tip is mounted to an SEM stub, which is in turn mounted in a rigid ceramic holder that is attached to the extension arm of the nanomechanical indenter. This extension arm can be finely controlled using its linear motor. Two coax cables are attached to an electrical port on the SEM chamber. The external cables are connected to the potentiostat (Bio-Logic SP-200). The internal coax cables are each split into a conduction wire and a shielding wire, each ending with an alligator clip. Both shielding wires (Sh1 and Sh2) are attached to the set screw of the SEM cube on the SEM stage, which is connected to ground through the SEM door. One conduction wire is attached to the tip (C2) and the other is attached to the stage (C1), to attempt to hold one side of the measurement to electrical ground. The tip can now be moved to the top of the sample under test using the sample stage and extension arm linear motor. This is configured so that the experiment is centered under the e-beam.

A typical compression test would proceed as follows: An image is taken before any displacement is applied. The e-beam and CCD camera are turned off. An open
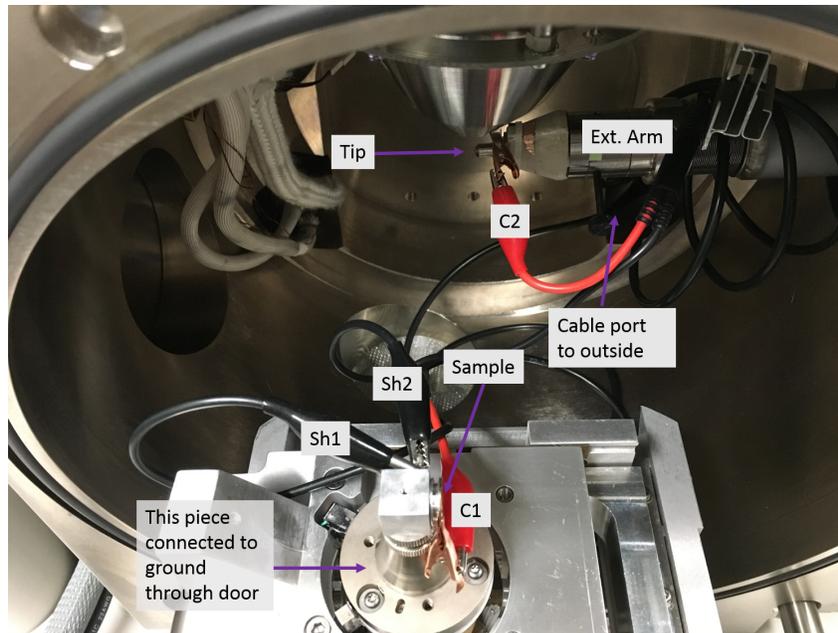
Figure 5.3: Optical image of the electromechanical experimental setup inside the SEM chamber.

circuit voltage (OCV) measurement is started on the potentiostat. With no additional stimulus, this results in a long term decaying voltage response, as seen in Figure 5.4.
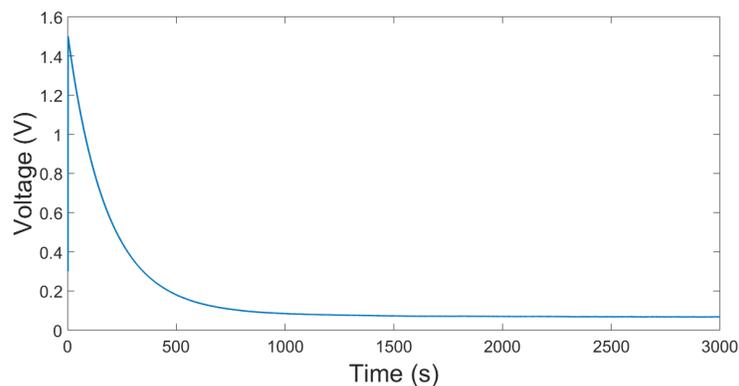
Figure 5.4: Long term open circuit voltage response of measurement system during experiment. Voltage versus time behavior of the measurement system when in contact with a sample, but no displacement is applied. The initial charge, likely built up from imaging with the electron beam, slowly discharges to a steady state value.

This response is likely due to the charge built up during imaging dissipating within the complicated system and is a topic of further characterization discussed in the following chapter. After several seconds, the extension arm linear motor is given

a command to move a specified number of microsteps, which are fractions of a revolution of the motor. When the sample is piezoelectric, this sudden displacement correlates to a sudden change in the voltage. Due to the large RC constant of the system, the background electrical response over the relatively short and consistent experiment time, typically 20 seconds after waiting 10-60 seconds after beginning the OCV measurement, can be treated as linear. This voltage change from the typical decay behavior can be identified and measured via MATLAB code. After several additional seconds, the OCV measurement is stopped, the e-beam is turned back on, and an image is taken. The difference between this image and the one taken before the compression can be used to accurately measure the applied displacement, as this experiment is fundamentally load-controlled. If the sample remains intact, another measurement can be taken in a similar manner. Data presented is always from at least the second measurement on each sample to ensure complete contact with the sample. In order to perform the experiment on the next sample, the tip displacement is reset and the sample stage is repositioned to the new location.

5.3 Introduction to Monolithic 3D architected ZnO

Multifunctional metal oxides are one of the most important classes of materials being used in modern society today. These materials exhibit unique properties such as piezoelectricity [133], superconductivity [134], and semiconductivity [135], making them ubiquitous in virtually every type of micro/nanosystem device technology to date. Unfortunately, the planar nature of traditional lithography places an inherent limitation on the geometries of the functional materials that can be achieved [136], and consequently the designs of the devices that can be fabricated. New experimental devices that have managed to circumvent this two-dimensional (2D) constraint and incorporate three-dimensional (3D) functional materials have been able to achieve greater performance [29, 137] and, in some cases, previously difficult to attain functionality [138, 139]. As a result of this, there has been an increasing amount of attention on the fabrication of these 3D metal oxide micro/nanostructures.

In particular, the remainder of this chapter will discuss the fabrication and characterization of piezoelectric zinc oxide (ZnO). ZnO is a popular piezoelectric material in current micro/nanosystems due to its relatively wide direct band gap and large piezoelectric response [140], as well as the ease in which it can be fabricated as 1D nanostructures [141] and thin films [142]. While 1D nanostructures can be patterned via templates or physically rearranged to create devices [25, 143, 144], this approach fails to achieve the complexity required for true 3D devices. ZnO nanowires have

also been successfully incorporated into polymer to create 3D nanocomposite structures using TPL [145]. While these may provide interesting optical properties, the low density (up to 5 wt %) and lack of physical contact between particles drastically reduces its potential as an electromechanical material.
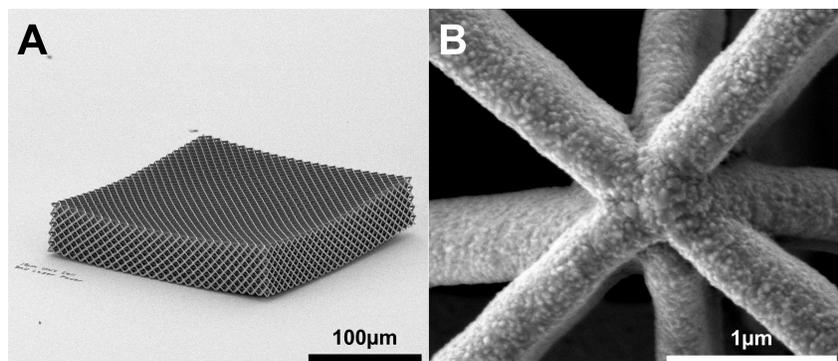
Figure 5.5: Core-shell ZnO nanolattice with A) low magnification overview and B) high magnification closeup of a lattice node. Sputtering assistance was provided by Dr. Yulia Tolstova following the procedure of Reference [146].

In the thin film realm, ZnO can be desposited using DC and RF magnetron sputtering [147, 148], chemical vapor deposition (CVD) [149], ALD [142], and pulsed laser deposition (PLD) [150], as well as other specialized techniques. In order to transform these films into 3D structures, multiple layers of lithography are required, such as in the micro-electro-mechanical systems (MEMS) field [151, 152] or an underlying sacrificial or permanent scaffold to create hollow [153, 154] or composite core-shell structures [24, 155, 156]. These approaches result in limited 3D configurations based on stacks of 2D patterns in the former case, and a composite or shell structure in the latter. An example of a core-shell nanolattice we fabricated using RF magnetron sputtering to coat the polymer nanolattice used throughout this work can be found in Figure 5.5. While these techniques can result in dense conformal coatings, the confinement to composite or hollow structures significantly limits the temperature, mechanical, electrical, and chemical optimization of devices, as well as complicates inquiries into the fundamental material properties of new or altered materials.

Additive manufacturing (AM) has recently emerged as one of the frontrunners for the fabrication of complex arbitrarily shaped monolithic three-dimensional metal oxide structures. A wide variety of AM techniques currently exist to 3D print monolithic metal oxides [157, 158], from direct processes like selective laser sintering [159, 160] and selective laser melting [161, 162], to indirect ones involving fused deposition modeling [163–165], inkjet printing [166–168], and lithography [169–

171]. In particular, processes involving photolithography are of exceptional interest as they are the closest to achieving the resolutions needed for device fabrication [172]. Currently, these photolithographic techniques typically involve the selective curing of a photosensitive resin slurry filled with metal oxide powders, followed by a high temperature treatment that burns off the organic matrix and sinters the metal oxide particles together [173–176]. While simple in its approach and versatile in the types of metal oxide powders that can be used, the scattering of light due to the high loading of particles (>50 wt%) significantly reduces the resolution of the structures that can be made [177], thus rendering it difficult to meet the feature scales needed for device fabrication. To address these limitations, recent works have investigated the use of preceramic photopolymers instead. These inorganic polymers have heteroatoms in their backbone, which are converted into their respective oxides/carbides upon pyrolysis [178–180]. The lack of scattering particles in these preceramic polymers then allows them to be used with high-resolution fabrication techniques to produce sub-micron structures [181]. However, these preceramic polymers are often not commercially available and need to be synthesized, which complicates the fabrication process and adds to its cost. Furthermore, with a few exceptions [182–185], almost all of the preceramic polymers being used today result in Si-based materials, limiting the type of oxides that can be made. There thus exists a pressing need to develop a new process that combines the best of both existing approaches, the simplicity and versatility of the slurry method, with the high resolutions afforded by the use of preceramic polymers, for the fabrication of arbitrarily shaped 3D metal oxide microstructures.

In this study, we present a new facile method for fabricating 3D metal oxides via the use of an aqueous metal-containing photoresin. By simply dissolving water-soluble metal salts in water along with other water-soluble organics, a homogenous, low viscosity aqueous photoresin can be obtained. The aqueous photoresin can then be used with any photolithography technique to produce a metal-ion containing polymer microstructure that is then subjected to a high temperature treatment in air to obtain the corresponding metal oxide. As a demonstration of this technique, a zinc-ion containing aqueous photoresin was used with two-photon lithography (TPL) to produce 3D piezoelectric microstructures of ZnO. The ability to make monolithic three-dimensional ZnO structures via this alternative slurry-free and direct write approach is thus especially exciting, as it simplifies the process significantly and enables previously impossible architectures and device designs.

5.4 Fabrication
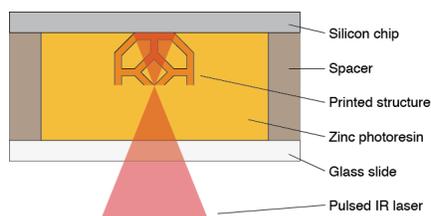
Figure 5.6: Schematic of the two-photon lithography set-up. Kapton tape approximately 100 μm thick were used as spacers between the silicon chip and the glass slide. The structures were written using two-photon lithography on the silicon chip and written down towards the glass slide.

To prepare the resin, zinc nitrate hexahydrate was first dissolved in water, and then mixed with poly(ethylene glycol) diacrylate (PEGda). A two-photon initiator, 7-diethylamino-3-thenoylcourmarin (DETC) was then dissolved in a small amount of dimethyl sulfoxide (DMSO), and then added to the zinc-PEGda solution to yield a pale orange solution. To fabricate the 3D "green" hydrogel part, a small amount of the photoresin was drop-cast onto a silicon substrate and used with TPL to directly fabricate the desired 3D structure (Figure 5.6). Pyrolysis of the cross-linked zinc-ion containing polymer 3D structure in air in an MTI OTF-1500X furnace at ambient pressure in air at 0.5° C/min to 500° C and then cooled back to room temperature at 2° C/min resulted in the final zinc oxide 3D structure. This entire process is demonstrated schematically in Figure 5.7. Three variations of the photoresin were created for characterization. Both Z1 and Z2 contained equal proportions of zinc nitrate and PEGda; however, Z1 contained the photoinitiator DETC for TPL (as described above) and Z2 contained the photoinitiator lithium phenyl-2,4,6-trimethylbenzoylphosphinate (LAP) in order to create large samples via UV curing for XRD and TGA analysis. A control resin C1 was fabricated to be identical to Z2, but without the zinc nitrate in order to understand the behavior of only the polymer in XRD and TGA.

The concept of entrapping metal ions within a polymer network prior to pyrolysis has been previously exploited in metal oxide nanoparticle synthesis methods like the Pechini process, and the polymer complex solution (PCS) method [186]. However, the lack of spatial control over the polymer network formation in those techniques precluded them from being able to fabricate more complex micro/nanostructures.
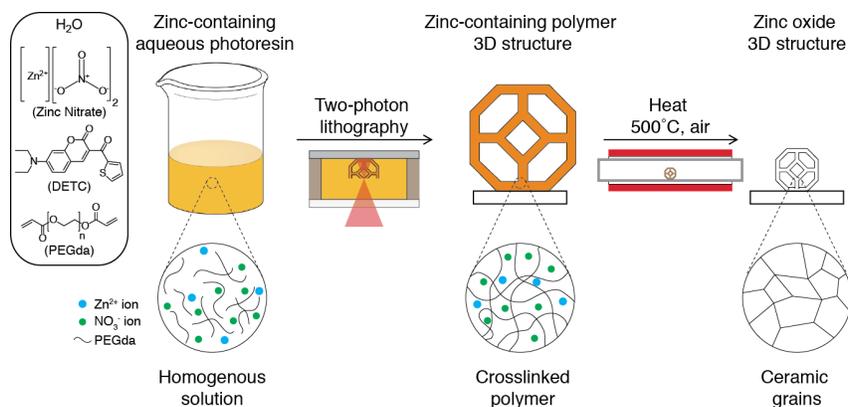
Figure 5.7: Process for microscale additive manufacturing of metal oxides. The zinc containing aqueous photoresin is prepared by mixing zinc nitrate, PEGda and DETC together. The resin is then used with TPL to obtain a crosslinked zinc-containing polymer 3D structure. Pyrolysis of the polymer structure at 500° C in air gives the final zinc oxide 3D structure.

Here, we circumvent this and achieve spatial control of the polymerization process via the use of telechelic PEGda macromonomers and a suitable photoinitiator.

As a demonstration of the compatibility of this process with additive manufacturing, structures of increasing complexity were first made via TPL, from pillars to micro-lattices of tetrakaidecahedron unit cells. Scanning electron images (SEM) of the structures before and after the heat treatment are shown in Figure 5.8. The polymeric pillar (Figure 5.8A), tetrakaidecahedron unit cell (Figure 5.8C), and microlattice of tetrakaidecahedrons (two unit cells by two unit cells by two unit cells) (Figure 5.8E) all showed fully resolved structures with smooth surfaces and uniform beams. Each structure was fabricated on top of a support structure to prevent them from coming in contact with the substrate. This is critical to the pyrolysis process as it prevents excessive stress, caused by asymmetrical shrinkage during the shrinkage process, from warping or destroying the structure. The support structure can be as simple as a pedestal (Figure 5.8C) or as complicated as another layer of tetrakaidecahedron unit cells (Figure 5.8E). The same pillar, tetrakaidecahedron unit cell and microlattice of tetrakaidecahedrons post-pyrolysis are shown in Figure 5.8B, 5.8D and 5.8F respectively. In all three cases, the support structures were completely destroyed, leaving behind the desired structure. The pyrolyzed structures all retained their net shapes, with about an 88% linear shrinkage, where the linear shrinkage LS is given by:

$$LS = \frac{(W_I - W_F)}{W_I} * 100\%$$

(5.5)
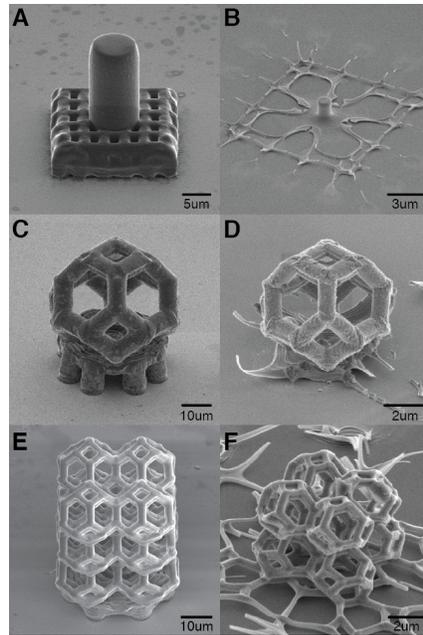
Figure 5.8: Scanning electron images of the samples before and after pyrolysis in air. Pillar geometry on top of support structure (A) as written, and (B) after heat treatment. Single tetrakaidecahedron unit cell on support structure (C) as written, and (D) after heat treatment. Tetrakaidecahedron microlattice two unit cells in each direction on top of a sacrificial tetrakaidecahedron layer (E) as written, and (F) after heat treatment. The structures all exhibited a linear shrinkage of approximately 88%.

where W_I and W_F are the initial and final widths, respectively. These pyrolyzed structures had smooth uniform beams, with no obvious cracks or macro-pores. Table 5.1 summarizes the linear shrinkage measurements and calculation according to Equation 5.5. It is important to note that the large shrinkages observed here could be exploited to provide resolutions beyond what can be typically achieved with two-photon lithography.

Structure Type	Initial Size [μm]	Final Size [μm]	Linear Shrinkage
Pillar	7.38	1.08	85.3%
Unit Cell	41.7	6.12	85.3%
Lattice	55.0	5.92	89.2%

Table 5.1: Linear shrinkage of structures after heat treatment.

The conversion from polymer to metal oxide with temperature is greatly influenced by the metal salt precursor used. Metal nitrates in particular affect the heating

process significantly, as they are also strong oxidizers. Thus, while they are a convenient source of metal cations due to their availability and high solubility limit in water, when heated with an organic fuel, a rapid, self-propagating combustion process can occur [187]. This can lead to the volatilization of the organic binder and the formation of the metal oxide at lower temperatures, i.e., the ignition temperature, as the heat of combustion released is sufficient to drive the reaction to completion [188].
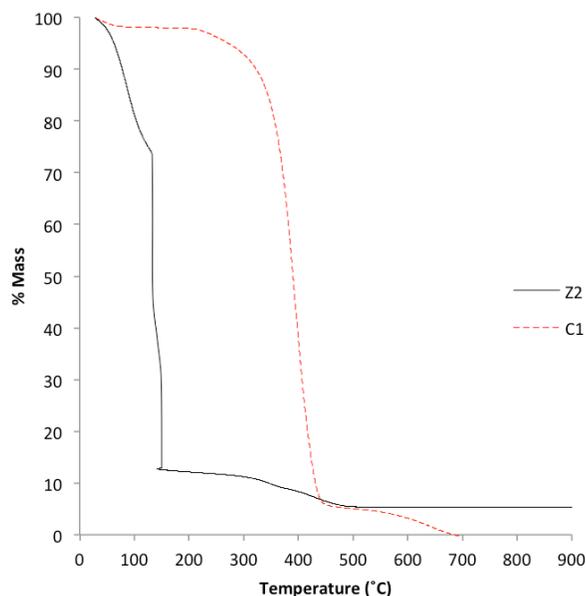
Figure 5.9: Thermogravimetric analysis of the zinc-nitrate containing polymer and its control in nitrogen. TGA data of polymers prepared from photoresin Z2 and C1. A rapid mass loss around 130° C can be observed with the zinc-nitrate containing polymer, which is absent in the control sample. This is clear evidence of the combustion process from the ignition of the zinc nitrate oxidizer and the polymer. The control C1 also exhibits complete mass loss above 700° C, whereas ZnO remains behind from the Z2 photoresin.

This is demonstrated in Figure 5.9 where thermogravimetric analysis (TGA) performed by Jong Hun Kang in the Davis lab of the zinc nitrate-containing polymers showed a rapid mass loss of about 62 wt% at around 150° C. Further heating to 500° C only showed a mass loss of about 8 wt%, with no further mass change after that. On the other hand, polymers without the zinc nitrate precursor were stable up to 200° C and only exhibited rapid mass loss, of about 90 wt%, on subsequent heating to 450° C. Further heating past 700° C resulted in the complete degradation of the sample. The difference in the TGA plots between the two is clear evidence

of the influence of the zinc nitrate precursor on the pyrolysis process. This TGA experiment was performed on a STA 6000 (PerkinElmer) from 30 to 900° C at a heating rate 5° C/min under nitrogen with a flow rate of 20 mL/min. Small samples of Z2 or C1 <100 mg were used for this analysis.

5.5   Characterization of Pyrolyzed Material

To determine the identity of the pyrolyzed material, a variety of characterization techniques were used, as shown in Figure 5.10. X-ray diffraction (XRD) was first used to determine the phase of the material. XRD (Bruker D2 Phaser) data was collected at 30kV and 10mA using a Cu source with a Lynxeye detector in the Lewis Lab at Caltech. Since a large sample is required for XRD, larger than what TPL is capable of producing, the aqueous resin Z2 was cast into a centimeter-sized mold and then photopolymerized with UV light. As a control, another polymer sample was made using the photoresin C1 where the zinc nitrate precursor was omitted. The zinc-containing polymer and the control were then heated to 500° C in air to give an off-white brittle ceramic and a grey ash, respectively. Figure 5.10A shows the XRD spectra obtained from both pyrolyzed samples. The sample made with the zinc nitrate precursor showed sharp diffraction peaks, which on further analysis were characteristic of ZnO. In contrast, the control sample only exhibited a broad halo at low angles, hinting that the sample likely only contained amorphous carbon.

Energy-dispersive X-ray spectroscopy (EDS) and transmission electron microscopy (TEM) were then conducted on the pyrolyzed 3D structures fabricated via two-photon lithography to determine its material composition. EDS maps were generated in a Zeiss 1550VP FESEM equipped with an Oxford X-Max SDD EDS system, utilizing an applied voltage of 15 kV. The elemental maps of one of the tetrakaidec-ahedron unit cells, as shown in Figure 5.10B, clearly show the homogenous distribution of zinc, oxygen and carbon throughout the printed structure, without the presence of any zinc-rich, oxygen-rich or carbon-rich phases. Since the XRD spectra only showed the presence of ZnO, without any impurities such as zinc carbonate, it is thus likely that the structures are predominantly ZnO with a small amount of carbon left behind from incomplete oxidation.

An FEI Tecnai F30 TEM at 300 kV was used to image the cross-section of a beam of one of the 3D structures that was placed on a copper half moon grid using traditional methods in a dual beam FIB (FEI Versa 3D) with a micromanipulator (EZLift) (Figure 5.11). The bright field (Figure 5.10C) and dark field (Figure
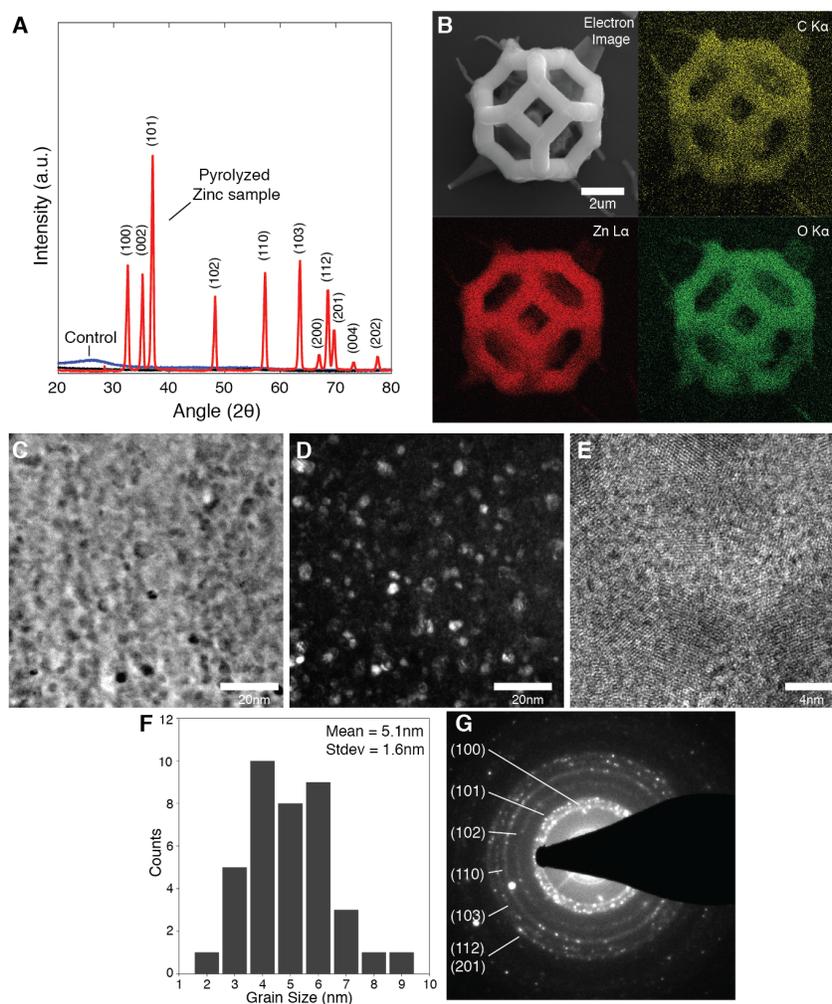
Figure 5.10: Characterization of fabricated ZnO samples. (A) XRD spectra of polymers with and without the zinc precursor after pyrolysis in air. The pyrolyzed zinc-containing polymer exhibited diffraction peaks characteristic of ZnO. (B) EDS elemental maps of a tetrakaidecahedron unit cell after pyrolysis in air. The maps showed that zinc, carbon and oxygen were homogeneously distributed throughout the structure. (C) Bright field, (D) dark field, and (E) high resolution TEM images taken from the cross-section of a pyrolyzed 3D ZnO structure show the nanocrystalline nature of the material. (F) Histogram of particle sizes measured from the dark field TEM image showed that they were 5.1 ± 1.6 nm in diameter (N=40). (G) TEM SAED of pyrolyzed ZnO with lattice planes indexed.

5.10D) TEM images clearly show the nanocrystalline nature of the material. This is further corroborated with the high-resolution TEM (HRTEM) image in Figure 5.10E, where the crystallinity within each grain can be clearly observed. In addition, measurements of the particles identified in the dark field image (Figure 5.10F)
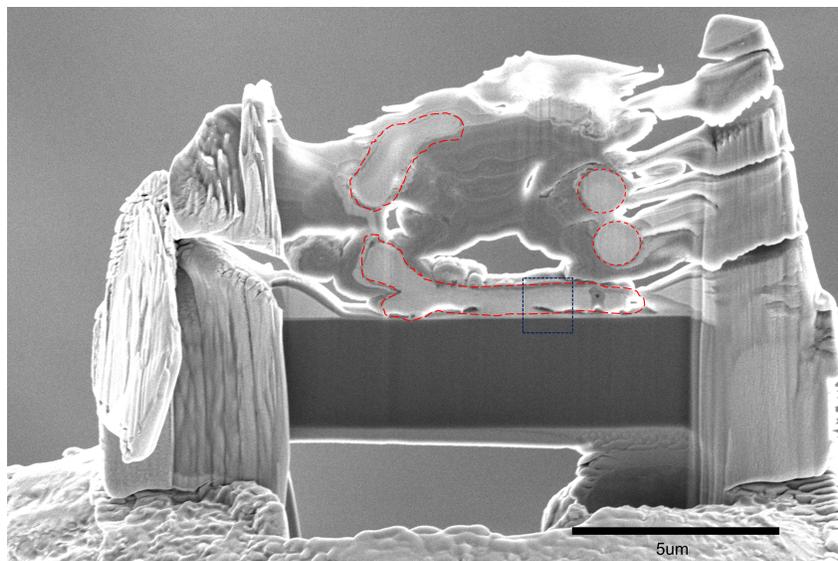
Figure 5.11: Cross section SEM image of the FIB liftout, with deposited Pt protection before final thinning. The red dashed shapes represent the captured sections of the unit cell beams. The blue dotted box indicates the area of TEM analysis, as it provided the thinnest cross section within the sample.

showed that they were 5.1 ± 1.6 nm in diameter. The selected area electron diffraction (SAED) pattern obtained from the TEM image (Figure 5.10G) also showed rings, which on further analysis, corresponded to the labeled orientations of polycrystalline ZnO. The outermost ring was labeled (112) / (201) because the spacing of the two orientations was so close that it was not possible to precisely distinguish between them or determine if both were present. The line of two large spots in the lower left quadrant was attributed to some beam overlap with the underlying silicon substrate.

5.6 Electromechanical Properties of Pyrolyzed Material

It is thus clear, from all the characterization techniques used, that pyrolysis of the zinc ion-containing polymer structures in air resulted in its conversion to monolithic polycrystalline ZnO. This ability to fabricate ZnO in such arbitrary shapes is a significant step forward from the current state of the art and could finally allow for the realization of previously inaccessible 3D piezoelectric microstructures. To demonstrate the potential of these ZnO microstructures as piezoelectric elements, we show that these 3D ZnO structures exhibit an electromechanical response during in-situ compression via the custom-built experimental setup described in the earlier section.

To verify that any electromechanical response was due to the fabricated ZnO mi-
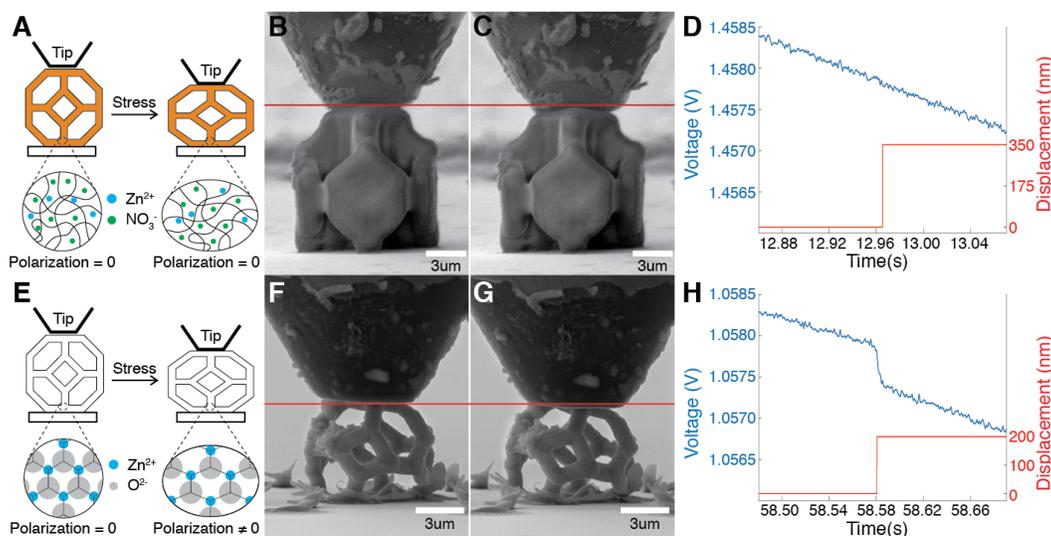
Figure 5.12: Electromechanical response of the fabricated 3D ZnO structures. (A) Schematic of the in-situ deformation of the zinc-containing tetrakaidecahedron polymer structure. No net polarization is seen before and after compression due to the amorphous nature of the polymer. Actual in-situ experiment (B) prior to compression, (C) after approximately 350 nm of compression. The red line serves as a guide to the eye. (D) The open circuit voltage data of this system depicts no measurable fluctuation in voltage from baseline system behavior. (E) Schematic of the in-situ deformation of a ZnO tetrakaidecahedron structure. Compression of the structure results in the development of an anisotropic crystal structure, and consequently a net polarization. Actual in-situ experiment (F) prior to compression, (G) after approximately 200 nm of compression. The red line serves as a guide to the eye. (H) The open circuit voltage data of this system depicts a clear negative voltage generated during this compression at 58.58s.

crostructure, we measured the open circuit voltage response during in-situ compression of both a 3D ZnO structure, and a 3D structure made of the zinc nitrate-containing polymer as a control (Figure 5.12). The printing parameters and design of the ZnO and polymer structures were kept as constant as possible for consistency and the write size of the polymer sample was chosen to compensate for the lack of shrinkage caused by thermal treatment. As shown schematically in Figure 5.12A, compression of the polymer should not result in any net polarization due to its amorphous nature and uniform charge distribution. In-situ compression of the tetrakaidecahedron polymer structure (Figure 5.12B and Figure 5.12C) showed no deviation from the long-term transient response of the measurement system in its open circuit voltage response (Figure 5.12D). This long-term response resembles the exponential decay of a discharging capacitor (as described in Figure 5.9) and

can be attributed to the experimental set-up, as described in an earlier section. With this in mind, it is thus clear that the zinc nitrate-containing polymer did not exhibit any electromechanical behavior on compression. On the other hand, the anisotropic crystal structure of ZnO leads to a net polarization on elastic deformation, and consequently electromechanical behavior (Figure 5.12E). In-situ compression of the tetrakaidecahedron ZnO structures (Figure 5.12F and Figure 5.12G) showed a large change in voltage the moment the displacement was applied at around the 58.58 seconds mark. Since this is not observed in the control experiment, this is definitive proof that the 3D ZnO microstructure exhibits electromechanical capabilities. Furthermore, the fact that the open circuit voltage measurement did not short on contact with the ZnO microstructure indicates that the carbon seen in Figure 5.10B was insufficient to form a conductive pathway. Quantification of the electromechanical response using this custom measurement system is currently underway and is the subject of a future in-depth study described in the following chapter.

5.7   Summary and Outlook

We demonstrate the successful fabrication of arbitrarily designed 3D architected metal oxide microstructures via the use of an aqueous metal ion-containing photoresin. In this proof of concept work, we focused on microstructures made from piezoelectric ZnO to highlight both the ease of approach and its ability to fabricate piezoelectric 3D microstructures, both of which are unmet needs in the microdevice community. A zinc ion-containing aqueous photoresin was first prepared and then used in conjunction with two-photon lithography to fabricate microstructures of varying complexity. These zinc ion-containing polymer microstructures were then pyrolyzed in air to give the corresponding ZnO microstructure. These ZnO microstructures exhibited near net shape, with a linear shrinkage of approximately 88%. XRD, EDS, and TEM analysis of the microstructures verified that the microstructures were composed of monolithic ZnO, with grain sizes 5.1 ± 1.6 nm in diameter. In-situ compression of a ZnO tetrakaidecahedron showed that it exhibited electromechanical capabilities.

Unlike current state of the art slurry and preceramic photopolymer approaches, our method provides a simple way of fabricating dense 3D structures of arbitrary design, while using inexpensive and commercially available reagents. This technique can easily be translated to other metal oxides: any water-soluble metal salt can be used in the preparation of the photoresin, shaped with an appropriate photolithography technique, and then pyrolyzed in air to make its corresponding metal oxide. The

versatility of this approach in fabricating 3D multifunctional metal oxides has direct implications in a variety of fields, from nano-electromechanical systems to chemical catalysis, and could allow for the production of previously impossible 3D smart devices.

QUANTIFICATION EFFORTS OF THE PIEZOELECTRIC RESPONSE OF NANO-ARCHITECTED MATERIALS

The previous chapter described an exciting fabrication method for creating mono-lithic 3D piezoelectric architectures. In order to fully characterize this material and realize its potential as an engineering multifunctional material, it is necessary to quantify its piezoelectric properties. While there are many advantages to the custom measurement system we built, it is not yet capable of providing quantitative data. This chapter will discuss the efforts at characterizing and quantifying the piezoelectric measurements from this system with the goal of quantifying new 3D architected piezoelectric materials.

6.1 Quartz Pillars as a Standard
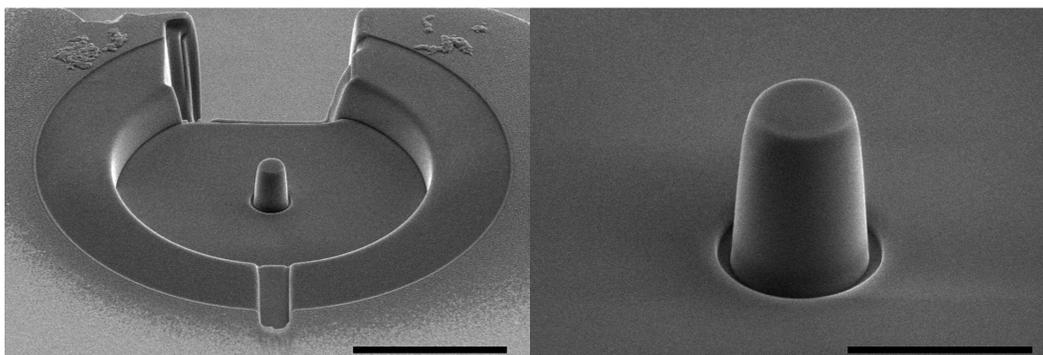
Figure 6.1: SEM images of a quartz pillar created via FIB milling at 52° at low (left) and high (right) magnification. The scalebar is 10 μm and 3 μm, respectively.

In order to calibrate or validate our electromechanical measurements, we chose to fabricate pillars out of quartz in order to perform uniaxial compression experiments. Quartz was chosen as it is a well-characterized non-ferroelectric piezoelectric material due to its extremely high mechanical quality factors and the multitude of timing, imaging, and sensing devices that have been created since its discovery as the first piezoelectric material [189, 190]. A 100 μm thick single crystal double sided polish piece of X-cut quartz was obtained from MTI Corporation, mounted onto an aluminum SEM stub with colloidal graphite, and coated with 100 nm of gold to reduce charging. Quartz pillars with diameters ranging from 4 μm to 500 nm

and aspect ratios of roughly 1:2 were fabricated via FIB milling. The FIB process involves milling cylindrical patterns of decreasing diameter until the desired pillar diameter and height is reached. The sample is then mounted at 90° to mill the top flat, as rounding can occur during the FIB process. Finally, for in-situ experiment samples, a viewing window is created to provide line of sight to the sample. For these samples, a 30 kV 1 nA ion beam was used. It was not possible to decrease the ion beam current as the diameter of the pattern was decreased, as is standard, because electronic drifting of the material prevented realigning the pattern throughout the process. A 1.6 µm diameter pillar is shown in Figure 6.1 at 52° tilt with viewing window for in-situ experiments.
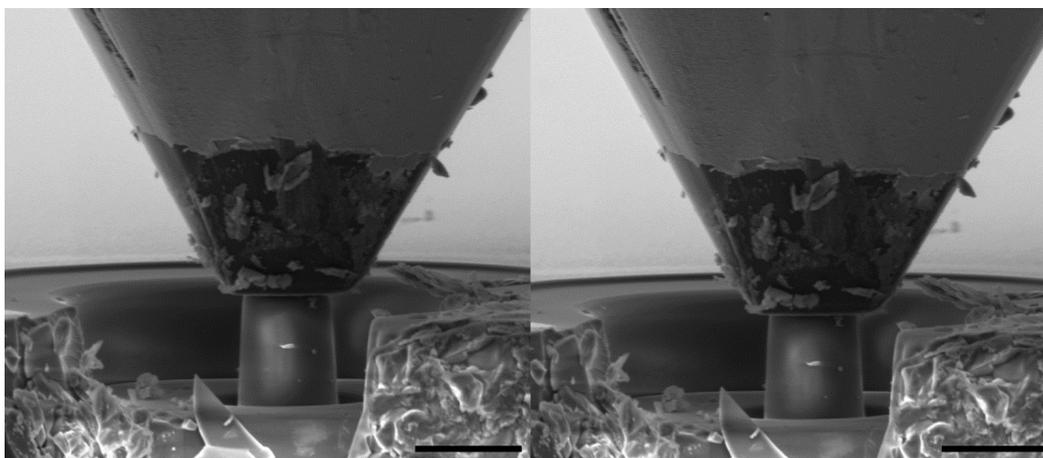
Figure 6.2: SEM image of a quartz pillar compression experiment before (left) and after (right) 300 micro steps of force from the linear motor. The scalebar is 5 µm.

Pillars of varying diameters were compressed using the experimental procedure described in Chapter 5. Figure 6.2 shows a quartz pillar sample under compression before and after a 300 micro step movement of the tip into the sample. These experiments generate a change in the baseline open circuit voltage measurement when the displacement is applied. As before, measurements are reported for at least the second displacement to ensure full contact with the sample. Figure 6.3 shows an example OCV response for a large (300 micro step) and small (50 micro step) displacement on a 4 µm diameter quartz pillar. Matlab software was created to measure the offset between the two linear regions on either side of the discontinuity (blue and orange lines) to provide a repeatable method for quantifying the piezoelectric response.
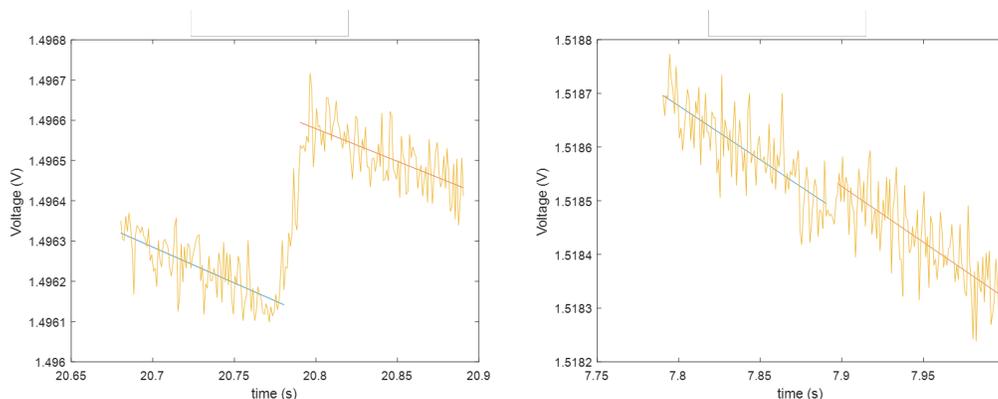
Figure 6.3: OCV response during two quartz pillar compressions on the same pillar with different applied force, 300 micro steps (left) and 50 micro steps (right). The sharp jump in voltage corresponds with the time at which the motor was actuated.

6.2 Quantification Challenges

Fortunately, this experimental method provided expected data trends on the same pillar: that is, a displacement of twice the distance typically corresponded to double the generated voltage in the OCV response. In certain cases with high strain, this value was less than what was linearly expected, which can likely be attributed to plastic deformation. Nevertheless, for an individual measurement, it was expected that the measured value of the response did not match what would be expected from the piezoelectric coefficient of quartz, as calibration is frequently needed with sensitive electronic measurements.

Figure 6.4 shows electromechanical response data for 5 roughly 4 μm diameter quartz pillars for different displacement (extension arm movement) values. The resistance through the measurement system was measured before each of these experiments by placing the conductive tip in contact with the aluminum SEM stub upon which the piece of quartz was attached and collecting a current-voltage (I-V) measurement. The inverse of the slope of this measurement was used as a rough measure of the instrumental resistance and part of the contact resistance. The values of each of these measurements is placed next to the cluster of corresponding data points. It is clear that the measured resistance value affects the corresponding voltage response measurement. Furthermore, the absolute value of these measurements may be affected by an effective voltage divider within the circuit. Therefore, the complex geometry of the experiment inside the chamber indicates the need for a thoughtful equivalent circuit and subsequent calibration.
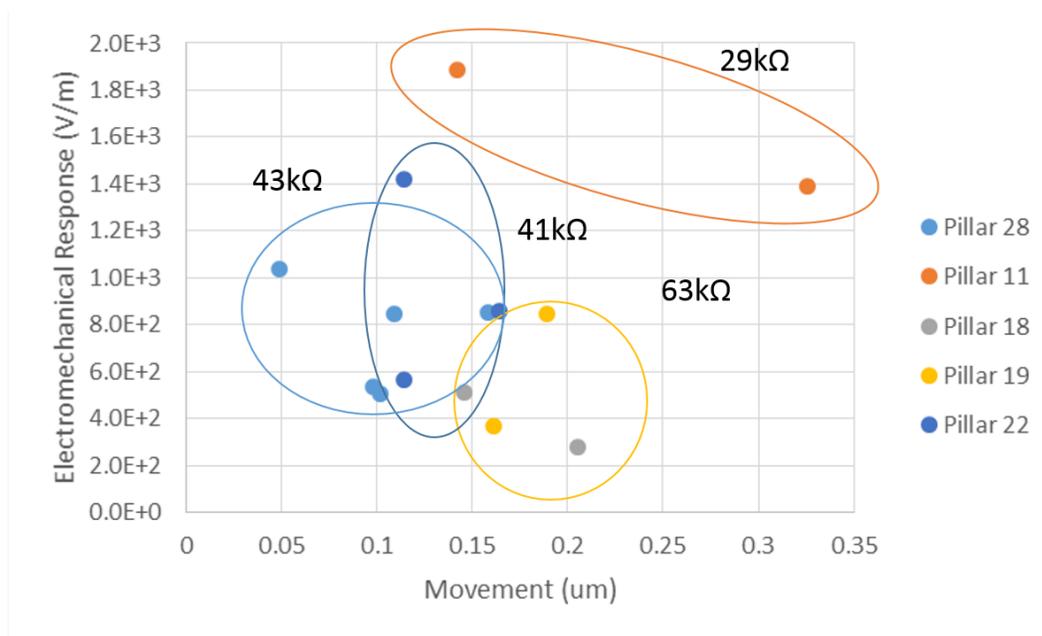
Figure 6.4: Comparison of the electromechanical response of roughly 4 μm diameter quartz pillars under different resistance of experimental measurement at different displacement values.

6.3   Equivalent Circuit Model

Components

In order to better understand the components of the measurement system and to calibrate the variety of experiments that are now enabled by this capability, we must first create an equivalent circuit model. As described earlier, the experiment is performed by measuring the open circuit voltage of our circuit using a potentiostat. This potentiostat was chosen instead of a simpler voltmeter in order to enable ultra-low current and small measurement time intervals. Moving inward from one potentiostat lead, the experimental circuit consists of an aluminum stub that holds a tungsten carbide (WC) flat punch tip. This tip is in contact with the top of the sample. The circuit runs through the sample, which is mounted on an aluminum SEM stub. This SEM stub is mounted in an aluminum 90° SEM cube, which is in turn mounted on the SEM stage. The SEM stage is connected to the SEM ground, and the second potentiostat lead is attached to the 90° cube. The shielding cables that run to the potentiostat inside the chamber are also both grounded to the 90° cube to reduce possible electrical noise.

The simplest sample to measure from an electrical perspective would be one that has both a simple geometry and fills the entire space between the tip and the SEM stub.

We chose a cylinder as our simple geometry, as will be explained in further detail in a later section, with an aspect ratio of roughly 1:2. In order to study these samples at small diameters, in the range of several microns to several hundred nanometers, the aspect ratio places a challenging restriction on sample thicknesses. While it would be simpler from an electrical perspective to thin a piece of single crystal quartz to the micron-scale before patterning, for this preliminary work we chose to relax the quartz thickness requirement to enable easier fabrication. As such, the "sample" that is under test consists of a quartz pillar with a 1:2 aspect ratio on top of a thicker bulk quartz layer. This allows for a variety of sample diameters, and subsequent heights, on the same quartz substrate and greatly speeds the fabrication time since it allows for the use of commercially-grown 100 μm thick single crystal quartz. This does also, however, complicate the sample portion of our electrical circuit. For one, we now have two quartz components in series, with different cross sectional areas. Secondly, we introduce a potential parallel pathway that can generate parallel capacitance between the sample/tip and the outer rim of the FIB circular crater that defines the cylindrical pillar shape. This parallel pathway could also introduce a conductive pathway between the bottom of the pillar and the grounded gold layer on top of the outer rim of the FIB crater.
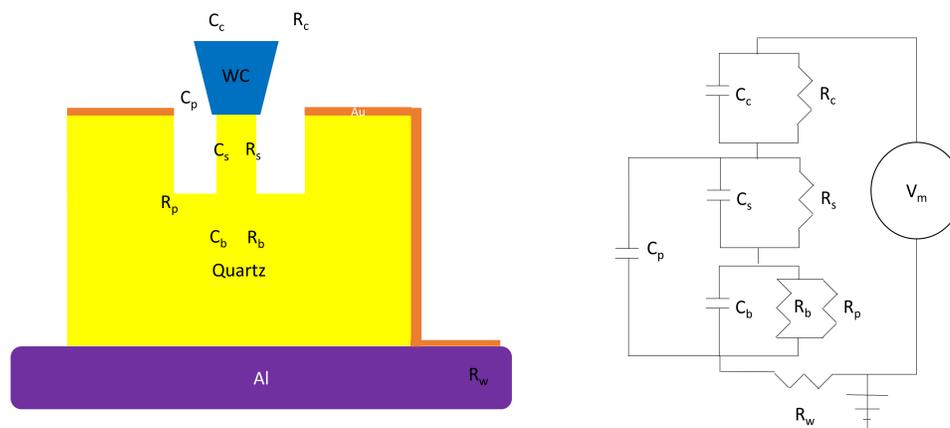
Figure 6.5: Schematic (left) and diagram (right) of experimental equivalent circuit.

Figure 6.5 shows a proposed experimental equivalent circuit. The schematic on the left shows a cross section of the experiment. The wire from the potentiostat and the aluminum stub it's connected to will have a small resistance and capacitance

value. The tungsten carbide (WC) tip will have a resistance and capacitance of the metal itself, as well as a resistance and capacitance of contact. As a simplification of this system, these values can be combined into a generalized tip resistance R_c and capacitance C_c, respectively. This tip is in contact with the sample of interest, in this case the pillar, which will have a resistance R_s and capacitance C_s. It is on this capacitor C_s that charge will accumulate via the piezoelectric effect when stress is applied to the sample. The bulk piece of quartz below the pillar has a resistance R_b and capacitance C_b. Here, again as a simplification, the resistance and capacitance of the interface between the bulk quartz and aluminum SEM stub are included in R_b and C_b. There is also a potential parallel resistive pathway, R_p, between the bottom of the pillar and the conductive layer of gold that surrounds the pillar trench. The last two potential significant components of the system are the resistance within the "wires" of the aluminum SEM stub and cube, as well as the connection to ground, which is labeled R_w, and the parallel capacitance between the tip and the conductive layer of gold that is connected to ground and surrounds the pillar C_p. The right side of Figure 6.5 shows a diagram of this equivalent circuit. The voltage measured during the open circuit voltage experiment is V_m. For this equivalent circuit model, we assume that the inductance of the components will have a minimal effect on the reactance. This is because the inductive reactance $X_L = 2\pi f L$, where f is frequency and L is inductance, and the experiment is performed at low frequencies. Similarly, we include the capacitance of the components because the capacitive reactance $X_C = -\frac{1}{2\pi f C}$. Therefore, for this model, the impedance of a component can be calculated using $Z = R + jX = R - \frac{j}{2\pi f C}$ [191].

Properties of Components

In order to populate this equivalent circuit model, we have performed several electrical measurements on our setup. By placing the WC tip in contact with the aluminum SEM stub and calculating the slope of a measured I-V curve, we can estimate a rough value for the combined resistance of the circuit from the metal components, which are contained in the terms R_c and R_w. These values are the ones reported in Figure 6.4 and span 29 kΩ - 63 kΩ. Using a simple ohmmeter, we measured the resistance of the SEM stub to the potentiostat lead, R_w, to be approximately 4 Ω. Therefore, we assume an average value of 46 kΩ for R_c. We can estimate the R_s of the pillar using the known resistivity of quartz and the geometry. The resistance can be calculated using the equation [191]:

$$R = \rho \frac{L}{A} \tag{6.1}$$

where ρ is the resistivity, L is the length, and A is the area of the pillar. Using a 4 μm diameter pillar with a 1:2 aspect ratio as an example, and a quartz resistivity $\rho = 20 \times 10^{15} \Omega-$cm perpendicular to the z axis [192], we estimate $R_s = 1.27 \times 10^{20} \Omega$. The resistance value through the bulk quartz, R_b, is challenging to determine since it is not immediately apparent which geometry to use for the conductive pathway volume. In order to accurately estimate this value, an FEA model should be created. For the purpose of illustration, we can estimate bounding values by considering two extreme cases for the 92 μm thickness. For the first case, we assume the pathway will be limited to the cross sectional area of the pillar above the bulk quartz. This results in $R_b = 1.46 \times 10^{21} \, \Omega$, which is certainly an overestimation of this resistance since the electrical pathway need not be so confined. For the lower case, we assume the pathway has a cross sectional area of the entire piece of quartz, which is 10 mm x 10 mm. This results in $R_b = 1.84 \times 10^{14} \, \Omega$, which is likely a gross underestimation since it is unlikely the charge just below the pillar will spread out through the resistive quartz to the extreme edges of the sample before meeting the bottom Al stub. Nevertheless, these values give us the property space where the true value of the bulk resistance is likely to reside.

The other possible pathway below the pillar is through the bulk laterally, connecting to the gold layer deposited on the surface of the entire quartz substrate. This represents a parallel resistance R_p. Estimating this value is difficult because the pathway is cylindrical and the effective conductive depth is unknown, preventing the simple application of Equation 6.1. Additionally, unlike R_b, where the conductive pathway is solely in the crystallographic x direction, the cylindrical pathway of R_p contains a combination of directions parallel and perpendicular to the crystallographic z axis. For comparison, the volume resistivity of quartz parallel to the z axis is $\rho = 0.1 \times 10^{13} \, \Omega-$m [192], roughly two orders of magnitude less than the value perpendicular to the z axis. In order to determine this value, an FEA model should be created or I-V measurement could possibly be performed using equipment capable of producing much higher voltages than the potentiostat used here, which has maximum supply of 10 V. For the purpose of illustration in our model, three cases for R_p will be utilized — a resistance smaller than our R_b range, a resistance roughly equal to the median R_b value, and a resistance larger than the R_b range. We have chosen R_b values of $10^{13} \, \Omega$, $10^{18} \, \Omega$, and $10^{22} \, \Omega$.

Finally, we must define the remaining capacitance values. It is difficult to calculate the expected capacitance of the pillar and the bulk quartz, C_s and C_b, respectively,

since the plate separation across the pillar and bulk is not significantly smaller than the plate length, which likely precludes the use of a parallel plate simplification. While the value is likely small, these capacitance calculation challenges are also true of the capacitance of the metal tip C_c. Similarly, the parallel capacitance between the gold thin film around the pillar and the tip, C_p, is difficult to calculate due to the unusual geometry. Therefore these four components, C_s, C_b, C_c, and C_p, would be best estimated using FEA software. For the purpose of illustration, and because they will not effect the "steady state" DC voltages within our circuit, we will simply assume a single capacitance value of 10 pF for these components. Once true estimations are made, the equivalent capacitance in the circuit can be verified by analyzing the transient electrical behavior. For example, by measuring the voltage decay with time during OCV measurement when the SEM e-beam is turned off, we can estimate the equivalent circuit capacitance by finding the RC constant and dividing by the equivalent resistance of the circuit.

SPICE Model

The measured voltage V_m represents the overall voltage response of the circuit. In order to accurately measure the electromechanical response of the sample under test, we must relate the measured voltage V_m to the voltage V_s that accumulates on the capacitor C_S, which represents the sample. One method of understanding the electrical behavior of the circuit is to use a Simulation Program with Integrated Circuit Emphasis, or SPICE, model. Utilizing LTspice XVII (Analog Devices, Inc.), we have created a circuit model using the layout proposed above. In order to simulate the electromechanical response of our sample, we have included a voltage source, V_s, in parallel with the capacitor C_s. We have also included a measurement isolation resistance R_m and capacitance C_m which sit between the measurement point V_m and ground. These values have been reported by the potentiostat manufacturer as 10 MΩ and 10 nF, respectively. Since we are performing a DC operating point simulation, creating a purely DC voltage-based illustration, we have defined all other capacitances as 10 pF. By setting V_s equal to 1 V, V_m in the model shows us the factor by which the measured voltage is reduced and $1/V_m$ shows us the multiplicative factor to convert our measured voltage to an estimated sample voltage. We will define our circuit multiplicative factor as:

$$MF_c = V_s/V_m \qquad (6.2)$$

In order to obtain the simulated V_m values, we perform the DC operating point test with $V_s = 1\ V$ in order to simplify the use of Equation 6.2. For illustration,

we have chosen to model R_b as low (1.84×10^{14} Ω), median (10^{18} Ω), and high (1.46×10^{21} Ω) for the median R_p value (10^{18} Ω), as can be seen in Figure 6.6. This results in $MF_c = 2 \times 10^7, 5 \times 10^{10}, 1 \times 10^{11}$, respectively.
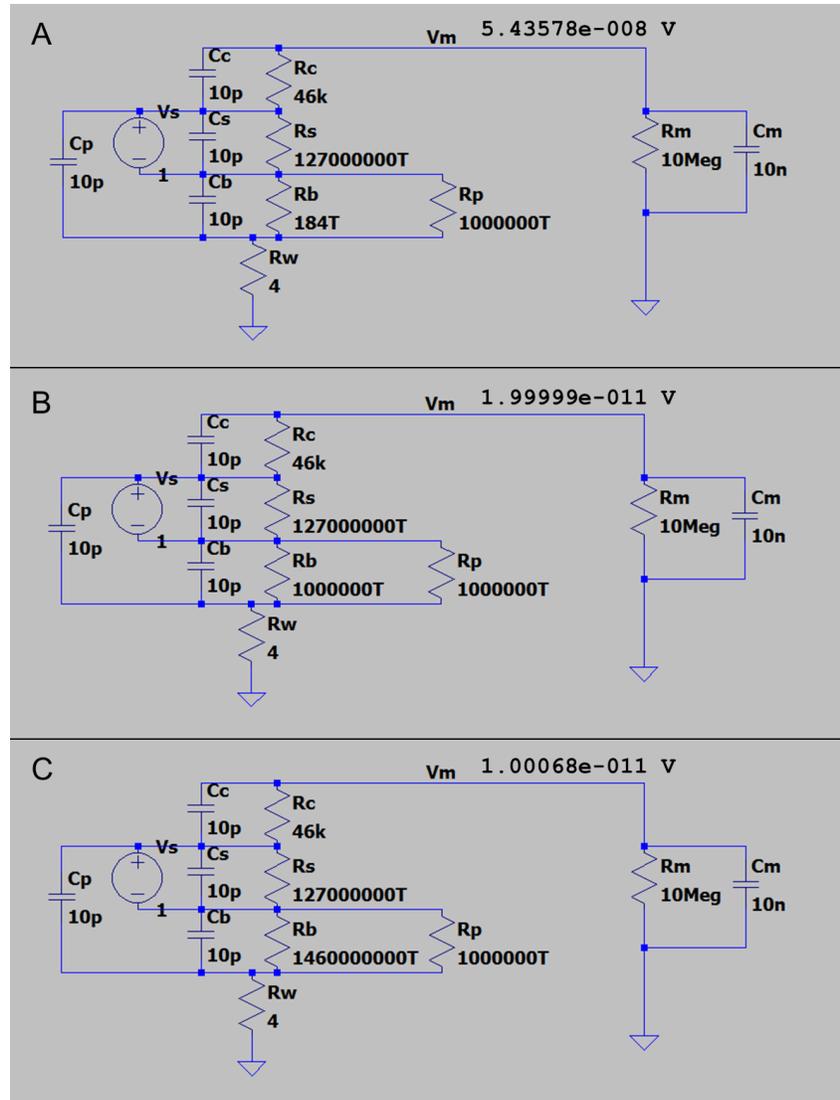
Figure 6.6: Schematic of SPICE models with A) low, B) median, and C) high R_b values.

We have also simulated the range of R_p values against a constant median R_b value. Figure 6.7 shows the corresponding graphical SPICE models. For the low R_p case $MF_c = 1 \times 10^6$, for the median case $MF_c = 5 \times 10^{10}$, and for the high R_p case $MF_c = 1 \times 10^{11}$. Table 6.1 summarizes all of the MF_c values for the chosen ranges of resistance values.
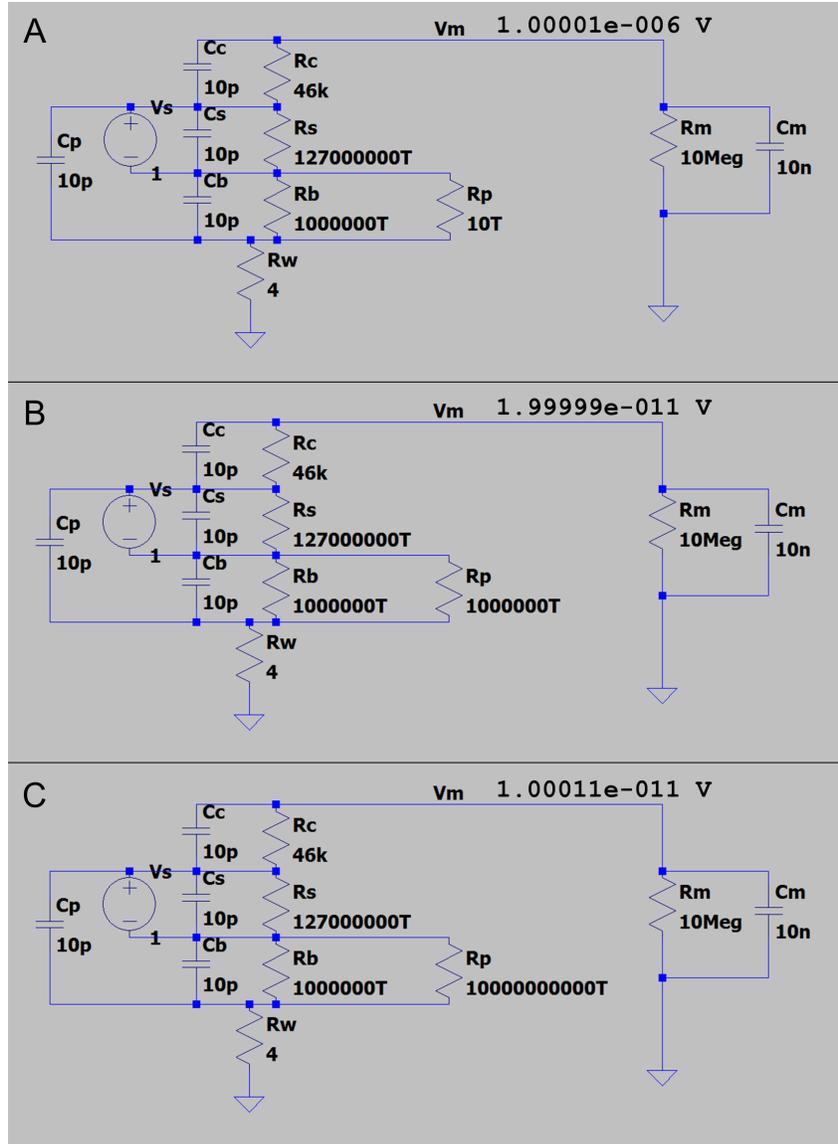
Figure 6.7: Schematic of SPICE models with A) low, B) median, and C) high R_p values.

		R_b	
	$1.84 \times 10^{14}\ \Omega$	$10^{18}\ \Omega$	$1.46 \times 10^{21}\ \Omega$
$10^{13}\ \Omega$	1×10^6	1×10^6	1×10^6
R_p $10^{18}\ \Omega$	2×10^7	5×10^{10}	1×10^{11}
$10^{22}\ \Omega$	2×10^7	1×10^{11}	1×10^{14}

Table 6.1: MF_c multiplicative factors for the range of R_b and R_p values.

From this data, we can get a sense of how the values in these parallel pathways behave as a voltage divider within this circuit. Once the values are determined via

experiment or more complete simulation, this table can act as a guide for a first order multiplicative factor to convert between the measured voltage and the voltage at sample. Examining the order of magnitudes, we see that when either R_b or R_p is at the lowest end of the range, the MF_c is fairly independent of the other value. This behavior is quite different when one term is constant for the other values in the range, spanning 7-8 orders of magnitude when either resistance is at the highest value, for instance.

By analyzing the sensitivity of the model to the values of the components, we can learn where to best focus future efforts in order to improve the accuracy of the results. First, there appears to be no sensitivity of the static voltage response to the capacitance values, as expected for this DC measurement. Second, the circuit is not very sensitive to R_c or R_s. This was observed by holding all other values constant at their median value and inputting a R_c or R_s value two orders of magnitude larger and smaller than the chosen value. The observed impact on V_m was negligible. Third, the circuit is quite sensitive to R_p, R_b, and R_m. This has two implications — 1. accurate estimation or measurement of R_p and R_b is critical to future accuracy of the experiment in this configuration and 2. the resistance of the measuring device has a large effect on the circuit response and may suggest the use of a different measurement scheme. For these reasons, significant care should be given to understanding or optimizing R_p, R_b, and R_m. Moving beyond understanding this particular configuration of this experiment, one could arrange the experiment in a way such as to eliminate the conductive pathways of R_p and R_b. This will be discussed in a later section.

6.4 Piezoelectric Quantification

Once a suitable electrical model is confirmed for a given measurement, we can begin to correlate the voltage responses to a piezoelectric coefficient. In the experiment's current configuration, a displacement is applied and a voltage is recorded. The resultant V/m response can be used as a practical measure of the particular sample under test. In order to obtain the geometry-independent material property, we must calculate its piezoelectric coefficient. The most commonly used and reported piezoelectric coefficient is d. Following the notation of T. Ikeda [116]:

$$d^\theta_{nij} = \left[\frac{\partial D_n}{\partial T_{ij}}\right]_{E,\theta} = \left[\frac{\partial S_{ij}}{\partial E_n}\right]_{T,\theta} \tag{6.3}$$

where D, T, E, and S are defined as in Chapter 5, and θ is temperature. The first definition of d represents the partial derivative of the electric charge density displacement with respect to stress at constant electric field and temperature, which is a direct piezoelectric effect. The second definition represents the partial derivative of strain with respect to electric field at constant stress and temperature, which corresponds to a converse piezoelectric effect. The piezoelectric coefficient d is typically represented by a matrix that looks like:

$$d = \left\{ \begin{array}{cccccc} d_{11} & d_{12} & d_{13} & d_{14} & d_{15} & d_{16} \\ d_{21} & d_{22} & d_{23} & d_{24} & d_{25} & d_{26} \\ d_{31} & d_{32} & d_{33} & d_{34} & d_{35} & d_{36} \end{array} \right\}$$

where the last subscript number is an abbreviation for interchangeable i and j values, as follows:

$$11 \rightarrow 1. \quad 22 \rightarrow 2. \quad 33 \rightarrow 3. \quad 23 \rightarrow 4. \quad 31 \rightarrow 5. \quad 12 \rightarrow 6.$$

The d matrix above represents values for all possible orientations. In reality, d tensors can have geometrical symmetry. Quartz, which is trigonal and in point group 32, for instance, has the following symmetry properties [116]:

$$d_{11} = -d_{12}$$

$$d_{14} = -d_{25}$$

$$d_{26} = -2d_{11}$$

with all other d values equal to zero.

In our current measurement, we measure the electrical response while applying mechanical strain. This can be captured using another piezoelectric constant, h. Extending the analysis by T. Ikeda, h can be defined as:

$$h^{\theta}_{nij} = \left[\frac{\partial E_n}{\partial S_{ij}} \right]_{D,\theta} = \left[\frac{\partial T_{ij}}{\partial D_n} \right]_{S,\theta} \tag{6.4}$$

Since we are performing a direct piezoelectric effect experiment, we can examine the first definition, which is the partial derivative of the electric field with respect to strain, at constant electric charge density displacement and temperature. Due to

the simple geometry of a pillar under uniaxial compression, we are able to translate our practical V/m sample measurement into a material property measurement. In this experiment, if we assume the electric field is roughly constant within the pillar, ignoring edge effects, we can simplify the partial derivative of the electric field in one direction to the change in E_1 with the applied strain S_{11}. Similarly, with our simplified geometric argument, we can divide our voltage measurements by the sample height to estimate E_1 and calculate the applied strain by dividing the displacement by the sample height. This solves the equation:

$$E_1 = h_{11}^* S_{11} \tag{6.5}$$

where in the case of our pillar, E_1 is the electric field in the loading direction, S_{11} is the uniaxial pillar strain, and h_{11}^* is the effective h_{11} value.

We have made many order of magnitude assumptions in configuring our SPICE model and obtaining the resulting MF_c values. Keeping this in mind, and the geometric assumptions made in order to use Equation 6.5, it's interesting to examine a calculated h_{11}^* when we assume $MF_c = 1 \times 10^6$. If we look to the 4 μm pillar example, a roughly 0.45 mV response was recorded for a 320 nm displacement. $V_m = 0.45$ mV corresponds to a $V_s = 450$ V using the multiplicative factor of 1×10^6. Dividing by 320 nm of displacement, this results in an h_{11}^* estimate of 1.4 V/nm or N/nC. For the broad assumptions made to obtain this value, the order-of-magnitude matches remarkably well for the reported value for quartz of $h_{11} = 4.36$ N/nC [193]. This gives us a possible indication that R_p tends towards the lower end of the range we explored, assuming the rest of our assumptions are valid. This observation again highlights the critical importance of accurately determining the resistance values in the circuit, which needs to be completed via FEA modeling.

While this **h** analysis gives one standardized quantified value of the piezoelectric performance of our material, redesigning the experiment to measure the **d** piezo-electric constant will enable comparison with a more frequently reported value. Similarly, redesigning the experiment can reduce the number of model components, reducing potential sources of error.

Redesigning for *d* Measurement

In order to produce this quantified material property data that can be universally compared to literature values, we propose an alternative experimental method. The data presented so far has been generated by simply attaching the tip to the rigid
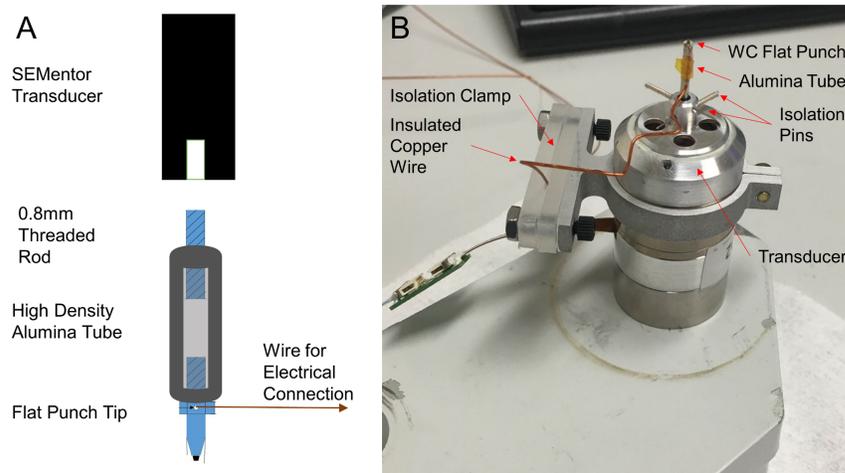
Figure 6.8: (A) Schematic of custom electrically-insulated flat punch tip with wire connection. (B) Optical image of an attempt to make electrical connection to a tip in the SEMentor nanomechanical transducer.

extension arm and applying a displacement using the linear motor. This method only allows us to apply a displacement and measure a voltage. If it were possible to attach the connection to a tip that can work with the displacement transducer, we could maintain a constant small force on the sample, on the order of several μN, apply a voltage to the sample, and measure the resultant displacement. In order to attempt this, special care was required to ensure electrical insulation between the tip and the sensitive electronics of the transducer, as shown in Figure 6.8A. The flat punch tip was secured in a hollow alumina tube using epoxy. The tip of a 0.8 mm hex nut screw was removed and the remaining threaded rod was epoxied into the other end of the alumina tube. This three piece assembly allowed for electrical insulation of the tip, while maintaining the ability to screw into the transducer assembly. Figure 6.8B shows an optical image of this attempt to attach an electrical connection to a flat punch tip. A 30 AWG Kapton-coated copper wire was stripped at the end, carefully wrapped tightly around the hexagonal nut base of the flat punch tip, and secured with silver epoxy. The copper wire was then attached to a plug that fit the SEM chamber port. This wire was bent near the tip and secured using a mechanical isolation clamp. This clamp prevented damage to the transducer due to any movement of the wire below the clamp when the isolation pins are removed during operation. Despite multiple applications of silver epoxy over time, the electrical connection of this

configuration was highly unstable. Ultimately, it was decided that this variation was counterproductive to quantifying this system and the initial experiments discussed throughout this work were performed without the transducer. The main challenge in achieving this configuration is attaching a mm-scale wire to a mm-scale tip in a way that is both reliable and prevents possible damage to the transducer, which is incredibly sensitive to transverse strain.

If it becomes possible to make a solid electrical connection and run the experiment in this configuration, the simple pillar geometry allows us to utilize the equation [131]:

$$\Delta L = d_{11}^* \Delta V_1 \tag{6.6}$$

As the transducer holds a small constant stress on the sample, we can apply a voltage V_1 and measure the resulting change in displacement, or length, L. These values allow us to directly measure the effective d_{11}^* in units of m/V.

It should be noted here that as with Equation 6.5, Equation 6.6 is a simplification of Equation 6.3 in that it assumes the electric field of the sample can be easily reduced to voltage through $E = V/t$, where t is the sample thickness. Due to the unusual geometry of this experiment with the bulk quartz below the pillar, this assumption should be verified using FEA. Alternatively, this experiment can be designed without the underlying bulk material in order to better directly measure the sample under test. An example pathway for this experiment is given in the following section.

Redesigning for Simplified Geometry

In order to reduce the complexity of this circuit, we propose an alternative configuration. If it is possible to polish the substrate to the desired thickness before using the FIB to create a pillar, we can remove R_b, C_b, and R_p from our equivalent circuit. Figure 6.9 shows a schematic and diagram of this configuration.

Maintaining planarity of this single crystal substrate down to the micron-scale presents a significant manufacturing challenge. One potential way to increase the efficiency and cost-effectiveness of this process is to planarize the substrate at a slight angle, so that one can create a variety of pillar sizes on the same substrate while maintaining a common aspect ratio. The tops of the pillars can be made parallel to the underlying SEM stub after creation using the FIB. In this approach, a technique for estimating or tracking the depth spatially across the sample would be helpful, as milling pillars by trial and error would be quite time consuming. Another
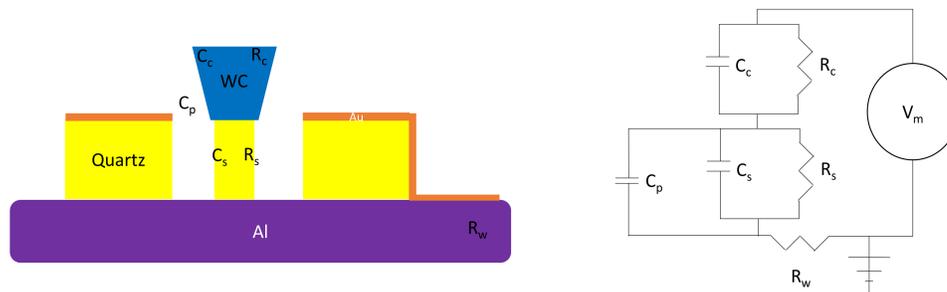
Figure 6.9: Schematic (left) and diagram (right) of geometrically simplified experimental equivalent circuit.

approach is a bottom-up one, where the pillars are grown via a deposition technique. An example of this method will be given in the following section.
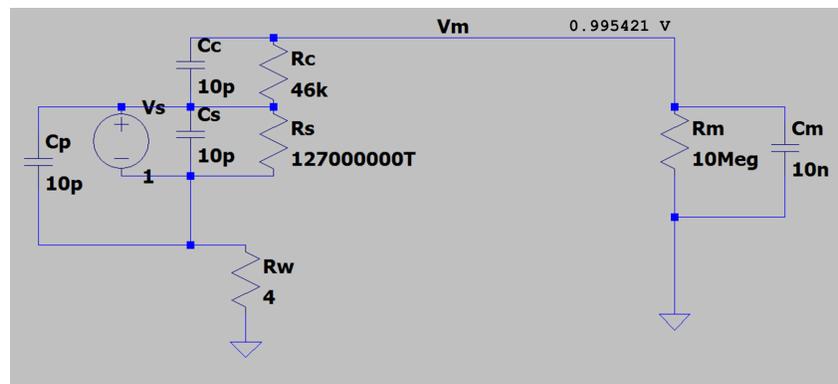
Figure 6.10: Schematic of a SPICE model for the simplified geometry.

While the thinner substrate requirement complicates the sample fabrication, the benefit of this configuration is that it drastically simplifies the equivalent circuit and subsequent multiplicative factor. Figure 6.10 shows a SPICE model diagram for this configuration. When the parallel pathways of R_b and R_p are removed, the voltage divider becomes many orders of magnitude less severe. So much so, that if we assume the same values from earlier for the remaining circuit, the $MF_c \approx 1$. Subsequently, this means that $V_m \approx V_s$, likely removing the need to account for the

measurement circuit when examining DC voltage. It should be noted that the MF_c value of this circuit is very dependent on the value of R_m. As R_m increases, V_m approaches V_s. As the order of magnitude of R_m shrinks, MF_c drastically increases. While providing a simpler circuit in this configuration, this point highlights that the resistance of the measurement equipment itself remains an important factor. In particular, the benefit of this simplification is maximized when R_m is large.

This section discussed the piezoelectric quantification of the initial experiments on quartz pillars. It highlighted some of the challenges with performing these calculations and proposed several changes in order to aid the analysis and produce more relatable results. The following section will describe how these techniques can be applied to characterizing ZnO and what a simplified geometry experiment could practically look like.

6.5 ZnO Characterization

Once the quantification analysis is completed, we can utilize this custom measurement system to study a variety of materials and architectures. We have chosen ZnO as our first material beyond our quartz calibration studies, and present three avenues of investigation using different fabrication techniques. Before doing so, let us review the piezoelectric properties of this material. ZnO, with a wurtzite crystal structure in point group 6mm, has the following symmetry properties [116]:

$$d_{31} = d_{32}$$

$$d_{15} = d_{24}$$

with all other d values besides d_{33} equal to zero. As with quartz, we are interested in the uniaxial properties of this material. In this case, the uniaxial piezoelectric axis is the z axis —therefore we would like to measure the d_{33} value, which has been reported as 12.4 pC/N [116]. The following three sections will describe proposed experiments on ZnO using three different fabrication techniques, along with their unique advantages.

- **Single Crystal FIB Pillars**

Following the method described above for quartz pillars, we have fabricated nanopillars from a 200 μm thick (0001) single crystal plate of ZnO (MTI Corp.) for uniaxial testing. These single-crystalline pillars can help provide a baseline that we can use to deconvolute the effects of grain size and porosity for more complicated structures
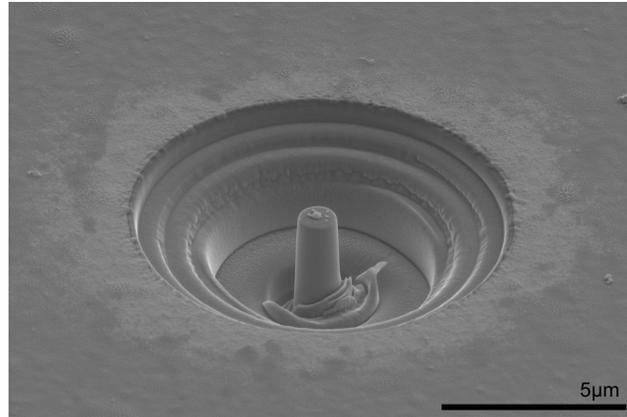
Figure 6.11: SEM image of a single-crystalline ZnO nanopillar with a 1 μm diameter and 3 μm height created via FIB milling.

in the future. Mechanical data from these pillars can also be used to compare to that of the quartz pillars to highlight any size effect trends or lack thereof. As with the quartz pillars, this experimental configuration requires the use of a MF_c and careful determination of R_b and R_p. It should also be noted that surface damage from the FIB may influence the mechanical and electrical response of pillars fabricated in this way. To combat and quantify any of these effects, as well as simplify the electrical circuit, we propose the method in the following section to produce single crystal faceted ZnO nanowires.

- **Single Crystal Hydrothermal Electrodeposition**

In order to better understand the piezoelectric properties of ZnO itself, we have also begun growing ZnO nanowires. ZnO possesses the fascinating ability to create 1D nanostructures via simple hydrothermal synthesis that is characterized by the following equations [141, 194]:

$$NO_3 + H_2O + 2e^- \rightarrow NO_2^- + 2OH^- \tag{6.7}$$

$$O_2 + 2H_2O + 4e^- \rightarrow 4OH^- \tag{6.8}$$

$$Zn^2 + OH^- + * \rightarrow Zn(OH)^+_{ad}/substrate \tag{6.9}$$

$$Zn(OH)^+_{ad}/substrate + OH^- \rightarrow ZnO + H_2O \tag{6.10}$$
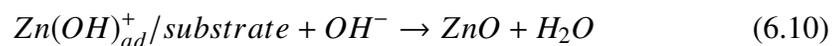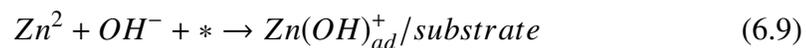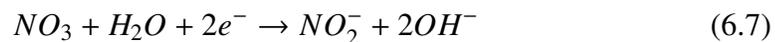
where $*$ indicates the vacancy site of the surface and ad indicates the adsorption onto the surface. The applied voltage during electrodeposition increases the local pH, which drives the reaction to deposit ZnO. Due to this mechanism, this fabrication

approach lends ZnO as an attractive candidate for templated 1D growth, without any of the potential surface effects generated from FIB use.
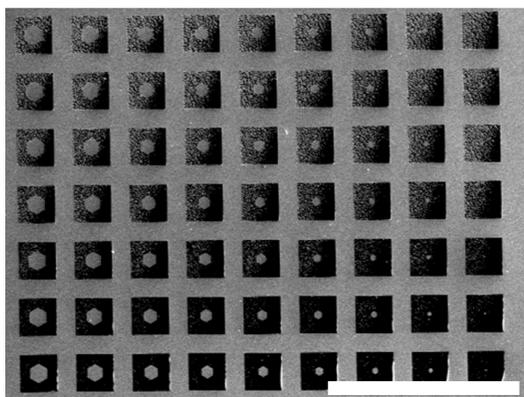
Figure 6.12: SEM image of a template array for hydrothermal growth power sweep. Scalebar 500 μm

In particular, TPL can be used to create "maskless lithography" templates of any shape. Figure 6.12 shows a diagnostic template array sweeping across different laser power and hole openings for hexagonal windows for a hydrothermal growth template. The laser power increases from bottom to top and the hole diameter increases from right to left. Once the laser power is optimized, for example here, in the row second from the bottom, a substrate can be covered with a continuous sheet of templates for electrodeposition.
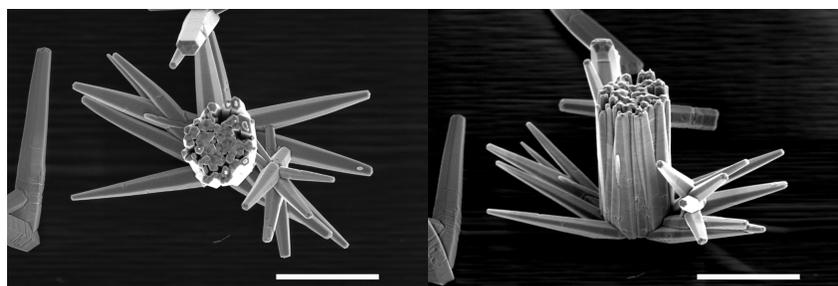
Figure 6.13: SEM images of a templated hydrothermally grown ZnO nanopillar top down (left) and at 52° (right). Scalebar is 5 μm.

Figure 6.13 shows a top down and tilted SEM image of a bundled ZnO nanowire pillar. One major advantage of this approach is that it drastically simplifies the electrical circuit of the measurement — the only object between the conductive electrodes is the ZnO nanowire pillar. This means that an equivalent circuit such as the one depicted in Figure 6.9 can be used. A further simplification of eliminating

C_p is likely valid, as the spacing between pillars can be made large by alternating templates with and without holes. Importantly, these bundles of single-crystalline nanowires provide an interesting stepping stone to understanding the electromechanical properties of more complicated polycrystalline materials. Putting it all together, nanostructures of this nature can provide important piezoresponse data for calibration and referencing, as well as provide a comparison between FIB fabricated ZnO pillars, grown nanowires, and pillars fabricated via the photoresin approach discussed in the previous chapter and the following section.

- **TPL Pillars**

While the fabricated 3D ZnO structures described in the last chapter represent an exciting possibility for new devices and applications, understanding the fundamental effects of grain size, porosity, and architecture on the piezoelectric response of the material is challenging in complex geometries. In order to quantify these material properties, we have utilized the technique to fabricate pillars for electromechanical characterization. Once the measurement is calibrated, this will allow us to assign a piezoelectric coefficient to this material using Equation 6.5 or 6.6 and probe any fabrication or architecture size dependence. As with the case of nanowires, this configuration represents a practical application of simplifying the circuit, as only the structure under test exists between the experiment's electrodes. Beyond aiding in our fundamental understanding of polycrystalline piezoelectricity at the nanoscale, this data will allow us to subsequently optimize 3D architectures for various applications. While it would be possible to study the electromechanical properties of the resultant material from this novel fabrication method using a more traditional technique, such as PFM, this custom measurement system allows us to study these properties at low frequency, with flat punch geometry, and in a reconfigurable setup that can be made to best match application circumstances for devices. Understanding both the measurement system and effect of the microstructure on the electromechanical experiments will be particularly important for more complex 3D architectures, as they are difficult to model. In this way, the technique of extending material characterization on simple geometries to architectures provides a practical approach to characterizing devices with complex geometries.

6.6   Summary and Outlook

The low frequency measurement system built for this work provides a promising route for characterizing nanoscale piezoelectric materials. In particular, the in-

situ capability of this technique enables detailed study of the electromechanical properties of 3D architected piezoelectric materials. It has been shown that this measurement is particularly sensitive to the resistance values of the components in series with the sample. As such, it is important to understand the equivalent circuit of the experiment and to model the remaining resistance and capacitance values using FEA in order to provide accurate multiplicative factor scaling. Further, techniques for performing a d measurement and simplifying the geometry have been suggested in order to increase the relatability and accuracy of the piezoelectric coefficient measurements generated by this experiment. From this groundwork, several avenues for calibrating and quantifying the piezoresponse have been proposed and are currently in progress. In particular, multiple ZnO systems can be characterized via this experiment, providing crucial insight into the effects of surface state, ion implantation, crystallinity, and sample size on the piezoelectric response. Looking to the future, this system can provide a powerful characterization tool for understanding the electromechanical properties of new materials and architectures.

Chapter 7

SUMMARY AND OUTLOOK

Throughout this thesis, we have explored exciting new applications of porous 3D nano-architected materials produced by TPL for electromechanical multifunctional applications. In particular, we have shown the advantages of utilizing architected materials for these functions over stochastic foams and have explored their promising applications as novel materials to provide tunable deformation, ultra low-k dielectric properties, and complex 3D piezoelectric devices.

As the field of TPL-produced nano-architected materials has grown, many efforts have been made to understand the effects of the unit cell and structural geometry, the node and beam sizes and shapes, and the constituent material. We took a pause from these endeavors to ask how a nanolattice would behave if it was constructed with two different unit cell sizes to simply create two distinct density regions. It was interesting to observe that the recoverable varied density structures behave as a superposition of the two uniform density components. That is, the low density region compresses fully first until there is a transition to the high density region. This causes the low density regions to exhibit effective Young's moduli that are similar and high density regions characterized by what would be expected for two springs in series. By changing the configuration from bi-phase to alternating layers, we show that the deformation behavior changes from a binary deformation to one that is more uniform throughout the structure, similar to an accordion. Additionally, the stiffness of the high density segment of the alternating structure was larger, likely due to improved contact between the layers and the substrate compared to the bi-phase case. This continues the narrative within the field of nano-architected materials that the boundary conditions are incredibly important and influence both their practical and experimental behavior. To understand the effect of interface angle, we fabricated and characterized a bi-phase structure with a 45° interface. This experiment taught us that it is possible to delay the onset of the effects of the high density region, which opens the door for tuning this response. Additionally, the architectural roughness of these structures controlled the local stress state to selectively shell buckle certain beams before others, which can provide a finer level or tunability. The drastic difference in density and angle lent a slight moment to this deformation, which may indicate potential deflection capabilities. In sum,

these observations provide us new tools to match the mechanical and deformation properties of recoverable nano-architected materials to a larger and more complex set of parameters.

Continuing the investigation into the multifunctional capabilities of hollow nano-architected nanolattices, we explored their use as ultra low-k dielectrics. The continuing advancement of integrated circuits depends on lowering the k value of its dielectric material, as the deleterious effects of capacitance between the metal wiring increase as the technology node decreases. We show that it's possible to fabricate a hollow alumina nanolattice near 1% density with a top plate to create a nanocapacitor whose interior material has a k value of 1.06 and low dielectric loss. This not only represents a huge improvement over the current technology, enabling new and more powerful devices, but to our knowledge at this time, represents a record effective stiffness to dielectric constant ratio at this frequency. In addition to its improved stiffness at low density due to its superior scaling factor and its recoverability due to its low t/a ratio, this material has a constant k across a significant voltage, frequency, and temperature range. Using cyclic testing, we also began an examination of the effect of strain on the dielectric breakdown strength. The observed mechanical and electrical resilience and recovery of these architectures are particularly impressive when we consider the constituent material is (typically brittle) ceramic alumina. All of these factors build a case for this tunable 3D nano-architected material as a practical solution for this problem — one that can address both the mechanical and electrical demands of the application.

Frustrated by the dearth of low frequency methods to observe the piezoresponse of materials, we designed, modified, built, and characterized a custom in-situ measurement system to collect electrical data from the existing SEMentor instrumentation. Similarly frustrated and intrigued by the limitations of current methods to fabricate monolithic piezoelectric materials at the nano and microscale, we developed a new technique to easily convert a metal salt-containing photoresin to 3D architected metal oxides via TPL followed by pyrolysis in air. In particular, we investigated ZnO and successfully fabricated pillars, unit cells of tetrakaidecahedrons, and lattices of tetrakaidecahedrons as a demonstration of the technique's versatility. These structures showed near net shape after 85% linear shrinkage with smooth uniform beams and no obvious cracks or macro-pores. We characterized this material using XRD, EDS, and TEM, all of which confirmed its identity as ZnO and provided insights into its microstructure. Furthermore, we observed the definitive electrome-

chanical response of this material in contrast to the non-piezoelectric response of the photoresin after curing, but before pyrolysis in air. As a byproduct of this experiment, we learned that this process does not leave behind enough carbon to create a conductive pathway through the structure. This conductive pathway of carbon represents a potential fatal flaw for similar photolithographic processes that would limit the applicability for piezoelectric applications, as no voltage difference could be supported by the material. This portion of the work demonstrates that it is possible to utilize TPL to create arbitrary 3D piezoelectric architectures at the sub-micron scale. Furthermore, this technique provides a pathway to create additional metal oxide structures using TPL and other photolithographic techniques that can enable a variety of new multifunctional devices and materials.

Beyond experiments on 3D architectures, this work has described the beginning of efforts to quantify the results from these electro-nanomechanical techniques for the materials described in this work and others. We have proposed three distinct avenues to achieve this. First, we have created a basic equivalent circuit and have utilized a SPICE model to examine the effect and sensitivity of the component values on the correlation between the measured voltage and the voltage generated by the sample under test. In doing so, we identified the critical components to examine further using FEA in order to accurately model the electrical circuit properties of our custom instrument and to validate the expected electromechanical response from our experiment. Second, we have fabricated quartz pillars in order to provide an internal reference for calibration by providing a simple geometry for uniaxial compression. Third, we have fabricated ZnO pillars via FIB, hydrothermally-grown nanowires, and TPL, to better understand the role of surface, grain size, and constituent material in determining the piezoelectric response of more complex geometries, such as those created in Chapter 5. These methods represent a potential framework for characterizing novel piezoelectric materials in the future, in structures of increasing complexity for new and improved electromechanical devices.

Putting this all together, we show that 3D nano-architected materials have significant potential as electromechanical multifunctional materials. TPL can enable not only these particular structures, but also can allow for the optimization of future improved materials and for creative alternative applications for materials research, such as maskless lithography. While increasing the porosity of materials directly reduces their weight and increases their surface area, this work contributes to the argument that directed architectural design of these materials can provide both improved

desired property-to-weight ratios and considerable tunability. By making use of improved additive manufacturing techniques, we can push our understanding of materials and composites to smaller length scales and more complex architectures.

BIBLIOGRAPHY

1. Jack, D. & Jack, K. Invited review: Carbides and nitrides in steel. *Materials Science and Engineering* **11,** 1–27. ISSN: 0025-5416 (1973).

2. Dwivedi, D., Lepková, K. & Becker, T. Carbon steel corrosion: a review of key surface properties and characterization methods. *RSC Adv.* **7,** 4580–4610 (2017).

3. Guthrie, F. On Eutexia. *Proceedings of the Physical Society of London* **6,** 124 (1884).

4. Chapman, P. W., Tufte, O. N., Zook, J. D. & Long, D. Electrical Properties of Heavily Doped Silicon. *Journal of Applied Physics* **34,** 3291–3295 (1963).

5. Ashby, M. Designing architectured materials. *Scripta Materialia* **68.** Architectured Materials, 4–7. ISSN: 1359-6462 (2013).

6. King, R. L. A Production Engineers View of Advanced Composite Materials. *Materials & Design* **3,** 515–522 (Aug. 1982).

7. Tertuliano, O. A. & Greer, J. R. The nanocomposite nature of bone drives its strength and damage resistance. *Nature Materials* **15,** 1195 (Aug. 2016).

8. *787 Dreamliner By Design - Advanced Composite Use* `https://www.boeing.com/commercial/787/by-design/#/advanced-composite-use`.

9. Smith, B., Szyniszewski, S., Hajjar, J., Schafer, B. & Arwade, S. Steel foam for structures: A review of applications, manufacturing and material properties. *Journal of Constructional Steel Research* **71,** 1–10. ISSN: 0143-974X (2012).

10. Qin, J., Chen, Q., Yang, C. & Huang, Y. Research process on property and application of metal porous materials. *Journal of Alloys and Compounds* **654,** 39–44. ISSN: 0925-8388 (2016).

11. Gibson, L. & Ashby, M. *Cellular solids: structure and properties* (Cambridge Univ Pr, 1999).

12. Gibson, L. J., Ashby, M. F., Schajer, G. S. & Robertson, C. I. The Mechanics of Two-Dimensional Cellular Materials. *Proceedings of the Royal Society of London. Series A, Mathematical and Physical Sciences* **382,** 25–42. ISSN: 00804630 (1982).

13. Ukken, E. T. & B.R., B. REVIEW ON STRUCTURAL PERFORMANCE OF HONEYCOMB SANDWICH PANEL. *International Research Journal of Engineering and Technology* **4,** 2558–2562. ISSN: 2395-0056 (6 2017).

14. Fleck, N. A., Deshpande, V. S. & Ashby, M. F. Micro-architectured materials: past, present and future. *Proceedings of the Royal Society of London A: Mathematical, Physical and Engineering Sciences* **466,** 2495–2516. ISSN: 1364-5021 (2010).

15. Ma, H.-S., Prévost, J.-H., Jullien, R. & Scherer, G. W. Computer simulation of mechanical structure–property relationship of aerogels. *Journal of Non-Crystalline Solids* **285,** 216–221. ISSN: 0022-3093 (2001).

16. Schaedler, T. A. *et al.* Ultralight Metallic Microlattices. *Science* **334,** 962–965. ISSN: 0036-8075 (2011).

17. Portela, C. M., Greer, J. R. & Kochmann, D. M. Impact of node geometry on the effective stiffness of non-slender three-dimensional truss lattice architectures. *Extreme Mechanics Letters* **22,** 138–148. ISSN: 2352-4316 (2018).

18. Meza, L. R., Das, S. & Greer, J. R. Strong, lightweight, and recoverable three-dimensional ceramic nanolattices. *Science* **345,** 1322–1326. ISSN: 0036-8075 (2014).

19. Maggi, A., Li, H. & Greer, J. R. Three-dimensional nano-architected scaffolds with tunable stiffness for efficient bone tissue growth. *Acta Biomaterialia* **63,** 294–305. ISSN: 1742-7061 (2017).

20. Yee, D. W., Schulz, M. D., Grubbs, R. H. & Greer, J. R. Functionalized 3D Architected Materials via Thiol-Michael Addition and Two-Photon Lithography. *Advanced Materials* **29,** 1605293 (2017).

21. Dou, N. G., Jagt, R. A., Portela, C. M., Greer, J. R. & Minnich, A. J. Ultralow Thermal Conductivity and Mechanical Resilience of Architected Nanolattices. *Nano Letters* **18,** 4755–4761 (2018).

22. Román-Manso, B. *et al.* Electrically functional 3D-architectured graphene/SiC composites. *Carbon* **100,** 318–328. ISSN: 0008-6223 (2016).

23. Xu, L. *et al.* Micro/Nano gas sensors: a new strategy towards in-situ wafer-level fabrication of high-performance gas sensing chips. *Sci Rep* **5,** 10507–10507. ISSN: 2045-2322 (May 2015).

24. Stano, K. L. *et al.* Ultralight Interconnected Metal Oxide Nanotube Networks. *Small* **12,** 2432–2438 (2016).

25. Xu, S. *et al.* Self-powered nanowire devices. *Nature nanotechnology* **5,** 366–73 (May 2010).

26. Salonitis, K., Pandremenos, J., Paralikas, J. & Chryssolouris, G. Multifunctional materials: engineering applications and processing challenges. *The International Journal of Advanced Manufacturing Technology* **49,** 803–826. ISSN: 1433-3015 (July 2010).

27. Ferreira, A. D. B., Nóvoa, P. R. & Marques, A. T. Multifunctional Material Systems: A state-of-the-art review. *Composite Structures* **151.** Smart composites and composite structures In honour of the 70th anniversary of Professor Carlos Alberto Mota Soares, 3–35. ISSN: 0263-8223 (2016).

28. Tandon, B., Blaker, J. J. & Cartmell, S. H. Piezoelectric materials as stimulatory biomedical materials and scaffolds for bone repair. *Acta Biomaterialia* **73,** 1–20. ISSN: 1742-7061 (2018).

29. Nistorica, C., Latev, D., Gardner, D., Imai, D. & Daft, C. *Characterization of a 3D-MEMS piezoelectric transducer for portable imaging systems* in *2015 IEEE International Ultrasonics Symposium (IUS)* (Oct. 2015), 1–4. doi:`10.1109/ULTSYM.2015.0373`.

30. Jacobsen, A. J., Barvosa-Carter, W. & Nutt, S. Micro-scale Truss Structures formed from Self-Propagating Photopolymer Waveguides. *Advanced Materials* **19,** 3892–3896 (2007).

31. Campbell, M., Sharp, D. N., Harrison, M. T., Denning, R. G. & Turberfield, A. J. Fabrication of photonic crystals for the visible spectrum by holographic lithography. *Nature* **404,** 53 (Mar. 2000).

32. Bertsch, A., Lorenz, H. & Renaud, P. 3D microfabrication by combining microstereolithography and thick resist UV lithography. *Sensors and Actuators A: Physical* **73,** 14–23. ISSN: 0924-4247 (1999).

33. Sun, H.-B., Matsuo, S. & Misawa, H. Three-dimensional photonic crystal structures achieved with two-photon-absorption photopolymerization of resin. *Applied Physics Letters* **74,** 786–788 (1999).

34. Xia, Q., Zhong, C.-W. & Luo, J. Low temperature sintering and characteristics of K2O–B2O3–SiO2–Al2O3 glass/ceramic composites for LTCC applications. *Journal of Materials Science: Materials in Electronics* **25,** 4187–4192. ISSN: 1573-482X (Oct. 2014).

35. Chernow, V. F., Alaeian, H., Dionne, J. A. & Greer, J. R. Polymer lattices as mechanically tunable 3-dimensional photonic crystals operating in the infrared. *Applied Physics Letters* **107,** 101905 (2015).

36. Deshpande, V., Fleck, N. & Ashby, M. Effective properties of the octet-truss lattice material. *Journal of the Mechanics and Physics of Solids* **49,** 1747–1769. ISSN: 0022-5096 (2001).

37. Meza, L. R. *Design, Fabrication, and Mechanical Property Analysis of 3D Nanoarchitected Materials* PhD thesis (California Institute of Technology, 2016). doi:`10.7907/Z9154F1K`.

38. Saha, S. K., Divin, C., Cuadra, J. A. & Panas, R. M. *Part Damage due to Proximity Effects During Sub-Micron Additive Manufacturing via Two-Photon Lithography* in *ASME. International Manufacturing Science and Engineering Conference* (2016). doi:`10.1115/MSEC2016-8793`.

39. Thomas, R., Li, J., Ladak, S., Barrow, D. & Smowton, P. M. In situ fabricated 3D micro-lenses for photonic integrated circuits. *Opt. Express* **26,** 13436–13442 (2018).

40. Rashidi, S., Esfahani, J. A. & Karimi, N. Porous materials in building energy technologies—A review of the applications, modelling and experiments. *Renewable and Sustainable Energy Reviews* **91,** 229–247. ISSN: 364-0321 (2018).

41. Galstyan, V. Porous TiO2-Based Gas Sensors for Cyber Chemical Systems to Provide Security and Medical Diagnosis. *Sensors* **17.** ISSN: 1424-8220. doi:`10.3390/s17122947` (2017).

42. Nitta, N., Wu, F., Lee, J. T. & Yushin, G. Li-ion battery materials: present and future. *Materials Today* **18,** 252–264. ISSN: 1369-7021 (2015).

43. Shobana, M. & Kim, Y. Improved electrode materials for Li-ion batteries using microscale and sub-micrometer scale porous materials - A review. *Journal of Alloys and Compounds* **729,** 463–474. ISSN: 0925-8388 (2017).

44. Perego, C. & Millini, R. Porous materials in catalysis: challenges for mesoporous materials. *Chem. Soc. Rev.* **42,** 3956–3976 (9 2013).

45. Liang, J., Liang, Z., Zou, R. & Zhao, Y. Heterogeneous Catalysis in Zeolites, Mesoporous Silica, and Metal–Organic Frameworks. *Advanced Materials* **29,** 1701139 (2017).

46. Badawy, W. A. A review on solar cells from Si-single crystals to porous materials and quantum dots. *Journal of Advanced Research* **6,** 123–132. ISSN: 2090-1232 (2015).

47. Zheng, X. *et al.* Multiscale metallic metamaterials. *Nat. Mater.* **15,** 1100 (2016).

48. Bauer, J., Schroer, A., Schwaiger, R. & Kraft, O. Approaching theoretical strength in glassy carbon nanolattices. *Nat. Mater.* **15,** 438 (2016).

49. Lee, S.-W., Jafary-Zadeh, M., Chen, D. Z., Zhang, Y.-W. & Greer, J. R. Size Effect Suppresses Brittle Failure in Hollow Cu60Zr40 Metallic Glass Nanolattices Deformed at Cryogenic Temperatures. *Nano Lett.* **15,** 5673 (2015).

50. Liontas, R. & Greer, J. R. 3D nano-architected metallic glass: Size effect suppresses catastrophic failure. *Acta Mater.* **133,** 393. ISSN: 1359-6454 (2017).

51. Montemayor, L. C., Wong, W. H., Zhang, Y.-W. & Greer, J. R. Insensitivity to Flaws Leads to Damage Tolerance in Brittle Architected Meta-Materials. *Sci. Rep.* **6,** 20570 (2016).

52. Meza, L. R. *et al.* Resilient 3D hierarchical architected metamaterials. *Proceedings of the National Academy of Sciences* **112,** 11502–11507. ISSN: 0027-8424 (2015).

53. Lifson*, M. L., Kim*, M.-W., Greer, J. R. & Kim, B.-J. Enabling Simultaneous Extreme Ultra Low-k in Stiff, Resilient, and Thermally Stable Nano-Architected Materials. *Nano Letters* **17.** doi: 10.1021/acs.nanolett.7b03941, 7737–7743 (2017).

54. Frenzel, T., Findeisen, C., Kadic, M., Gumbsch, P. & Wegener, M. Tailored Buckling Microlattices as Reusable Light-Weight Shock Absorbers. *Advanced Materials* **28,** 5865–5870 (2016).

55. Frenzel, T., Kadic, M. & Wegener, M. Three-dimensional mechanical metamaterials with a twist. *Science* **358,** 1072–1074. ISSN: 0036-8075 (2017).

56. Sun, S. *et al.* A Compact Variable Stiffness and Damping Shock Absorber for Vehicle Suspension. *IEEE/ASME Transactions on Mechatronics* **20,** 2621–2629. ISSN: 1083-4435 (Oct. 2015).

57. Konow, N. & Roberts, T. J. The series elastic shock absorber: tendon elasticity modulates energy dissipation by muscle during burst deceleration. *Proc Biol Sci* **282,** 20142800 (1804 2015).

58. Roberts, T. J. & Azizi, E. The series-elastic shock absorber: tendons attenuate muscle power during eccentric actions. *Journal of Applied Physiology* **109,** 396–404 (2010).

59. Knoefel, F., Patrick, L., Taylor, J. & Goubran, R. Dual-Stiffness Flooring: Can It Reduce Fracture Rates Associated With Falls? *Journal of the American Medical Directors Association* **14,** 303–305. ISSN: 1525-8610 (2013).

60. Matus, D. A. & Klamecki, B. E. Improved elastomeric seal design based on nonhomogeneous material properties. *Proceedings of the Institution of Mechanical Engineers, Part L: Journal of Materials: Design and Applications* **227,** 279–292 (2013).

61. Duncan, O. *et al.* Review of Auxetic Materials for Sports Applications: Expanding Options in Comfort and Protection. *Applied Sciences* **8.** ISSN: 2076-3417. doi:`10.3390/app8060941` (2018).

62. Center, P. R. *mobile fact sheet* `http://www.pewinternet.org/fact-sheet/mobile/`.

63. Lee, H. S., Lee, A. S., Baek, K.-Y. & Hwang, S. S. in *Dielectric Material* (ed Silaghi, M. A.) chap. 3 (IntechOpen, Rijeka, 2012). doi:`10.5772/51499`.

64. Kasap, S. *Principles of Electronic Materials and Devices* 3rd ed. ISBN: 0073104647 (McGraw-Hill, Inc., New York, NY, USA, 2006).

65. Baker, R. J. *CMOS: Circuit design, layout, and simulation* Third Edition (Wiley-IEEE Press, Piscataway, NJ, USA, 2010).

66. Plummer, J. D., Deal, M. & Griffin, P. *Silicon VLSI Technology: Fundamentals, Practice, and Modeling* (Pearson, Upper Saddle River, NJ, USA, 2000).

67. Sebastian, M. T. *Dielectric Materials for Wireless Communication* (Elsevier, 2010).

68. Dernovsek, O. *et al.* LTCC glass-ceramic composites for microwave application. *Journal of the European Ceramic Society* **21,** 1693–1697. ISSN: 0955-2219 (2001).

69. Ren, L., Zhou, H., Li, X., Xie, W. & Luo, X. Synthesis and characteristics of borosilicate-based glass–ceramics with different SiO2 and Na2O contents. *Journal of Alloys and Compounds* **646,** 780–786. ISSN: 0925-8388 (2015).

70. Sturdivant, R. *Millimeter-wave characterization of several substrate materials for automotive applications* in *Proceedings of Electrical Performance of Electronic Packaging* (Oct. 1995), 137–139. ISBN: 0-7803-3034-X. doi:`10.1109/EPEP.1995.524876`.

71. Croes, K. *et al. Comparison between intrinsic and integrated reliability properties of low-k materials* in *2011 International Reliability Physics Symposium* (Apr. 2011), 2F.3.1–2F.3.7. doi:`10.1109/IRPS.2011.5784467`.

72. Gupta, T. *Copper Interconnect Technology* (Springer Science & Business Media, 2010).

73. Maex, K. *et al.* Low dielectric constant materials for microelectronics. *Journal of Applied Physics* **93,** 8793–8841 (2003).

74. Luo, X. *et al.* Microstructure, sintering and properties of CaO–Al2O3–B2O3–SiO2 glass/Al2O3 composites with different CaO contents. *Journal of Materials Science: Materials in Electronics* **27,** 5446–5451. ISSN: 1573-482X (May 2016).

75. Heunisch, A., Dellert, A. & Roosen, A. Effect of powder, binder and process parameters on anisotropic shrinkage in tape cast ceramic products. *Journal of the European Ceramic Society* **30,** 3397–3406. ISSN: 0955-2219 (2010).

76. Pribetich, J., Ledee, R., Kennis, P., Pribetich, P. & Chive, M. Modelling of microstrip antenna with dielectric protective layer for lossy medium. English. *Electronics Letters* **24,** 1464–1465(1). ISSN: 0013-5194 (23 Nov. 1988).

77. Lee, B. *et al.* Ultralow-k nanoporous organosilicate dielectric films imprinted with dendritic spheres. *Nat. Mater.* **4,** 147 (2005).

78. Fu, G.-D., Shang, Z., Hong, L., Kang, E.-T. & Neoh, K.-G. Nanoporous, Ultralow-Dielectric- Constant Fluoropolymer Films from Agglomerated and Crosslinked Hollow Nanospheres of Poly(pentafluorostyrene)-block-Poly(divinylbenzene). *Advanced Materials* **17,** 2622–2626 (2005).

79. Li, S., Li, Z. & Yan, Y. Ultra-Low-k Pure-Silica Zeolite MFI Films Using Cyclodextrin as Porogen. *Adv. Mater.* **15,** 1528 (2003).

80. Huang, Q. R. *et al.* Structure and Interaction of Organic/Inorganic Hybrid Nanocomposites for Microelectronic Applications. 1. MSSQ/P(MMA-co-DMAEMA) Nanocomposites. *Chem. Mater.* **14,** 3676 (2002).

81. Krause, B. *et al.* Ultralow-k Dielectrics Made by Supercritical Foaming of Thin Polymer Films. *Adv. Mater.* **14,** 1041 (2002).

82. Yang, C. M., Cho, A. T., Pan, F. M., Tsai, T. G. & Chao, K. J. Spin-on Mesoporous Silica Films with Ultralow Dielectric Constants, Ordered Pore Structures, and Hydrophobic Surfaces. *Adv. Mater.* **13,** 1099 (2001).

83. Baskaran, S. *et al.* Low Dielectric Constant Mesoporous Silica Films Through Molecularly Templated Synthesis. *Adv. Mater.* **12,** 291 (2000).

84. Volksen, W., Lionti, K., Magbitang, T. & Dubois, G. Hybrid low dielectric constant thin films for microelectronics. *Scr. Mater.* **74,** 19. ISSN: 1359-6462 (2014).

85. Calas, S., Despetis, F., Woignier, T. & Phalippou, J. Mechanical Strength Evolution from Aerogels to Silica Glass. *J. Porous Mater.* **4,** 211. ISSN: 1573-4854 (1997).

86. Usman, M. *et al.* Intrinsic low dielectric behaviour of a highly thermally stable Sr-based metal–organic framework for interlayer dielectric materials. *J. Mater. Chem. C* **2,** 3762 (2014).

87. Chiang, C.-C. *et al.* Improvement in Leakage Current and Breakdown Field of Cu-Comb Capacitor Using a Silicon Oxycarbide Dielectric Barrier. *J. Electrochem. Soc.* **151,** G606 (2004).

88. Penn, S. J. *et al.* Effect of Porosity and Grain Size on the Microwave Dielectric Properties of Sintered Alumina. *J. Am. Ceram. Soc.* **80,** 1885 (1997).

89. Farrell, R., Goshal, T., Cvelbar, U., Petkov, N. & Morris, M. A. Advances in Ultra Low Dielectric Constant Ordered Porous Materials. *Electrochem. Soc. Interface* **20,** 39 (2011).

90. Meador, M. A. B. *et al.* Low Dielectric Polyimide Aerogels As Substrates for Lightweight Patch Antennas. *ACS Appl. Mater. Interfaces* **4,** 6346 (2012).

91. Meador, M. A. B. *et al.* Dielectric and Other Properties of Polyimide Aerogels Containing Fluorinated Blocks. *ACS Appl. Mater. Interfaces* **6,** 6062 (2014).

92. Padmanabhan, R., Bhat, N. & Mohan, S. High-Performance Metal–Insulator–Metal Capacitors Using Europium Oxide as Dielectric. *IEEE Trans. Electron Devices* **59,** 1364. ISSN: 0018-9383 (2012).

93. Kittel, C. *Introduction to solid state physics* (Wiley New York, 1986).

94. Tapily, K. *et al.* Nanoindentation Investigation of HfO2 and Al2O3 Films Grown by Atomic Layer Deposition. *J. Electrochem. Soc.* **155,** H545 (2008).

95. Tillotson, T. & Hrubesh, L. Transparent ultralow-density silica aerogels prepared by a two-step sol-gel process. *Journal of Non-Crystalline Solids* **145,** 44–50. ISSN: 0022-3093 (1992).

96. Rathore, J. S., Interrante, L. V. & Dubois, G. Ultra Low-k Films Derived from Hyperbranched Polycarbosilanes (HBPCS). *Adv. Funct. Mater.* **18,** 4022 (2008).

97. Murray, C. *et al.* Comparison of techniques to characterise the density, porosity and elastic modulus of porous low-k SiO2 xerogel films. *Microelectron. Eng.* **60.** Materials for Advanced Metallization, 133. ISSN: 0167-9317 (2002).

98. Flannery, C. M., Murray, C., Streiter, I. & Schulz, S. E. Characterization of thin-film aerogel porosity and stiffness with laser-generated surface acoustic waves. *Thin Solid Films* **388,** 1. ISSN: 0040-6090 (2001).

99. Kohl, P. A. Low–Dielectric Constant Insulators for Future Integrated Circuits and Packages. *Annu. Rev. Chem. Biomol. Eng.* **2,** 379 (2011).

100. Foeller, P. Y., Dean, J. S., Reaney, I. M. & Sinclair, D. C. Design of a bilayer ceramic capacitor with low temperature coefficient of capacitance. *Appl. Phys. Lett.* **109,** 082904 (2016).

101. Azad, A.-M., Pang, T. Y. & Alim, M. Ultra-Low Temperature Coefficient of Capacitance (Tcc) of the SrSnO3-Based Electrical Components. *Act. Passive Electron. Compon.* **26,** 151 (2003).

102. Antula, J. Temperature dependence of dielectric constant of Al2O3. *Phys. Lett. A* **25,** 308. ISSN: 0375-9601 (1967).

103. Lazarouk, S. *et al.* Reliability of built in aluminum interconnection with low-ϵ dielectric based on porous anodic alumina. *Solid-State Electron.* **44,** 815. ISSN: 0038-1101 (2000).

104. Gutmann, R. J. *et al.* Low Dielectric Constant Polymers For On-Chip Inter-level Dielectrics With Copper Metallization. *MRS Online Proc. Libr.* **381,** 381 (1995).

105. Chow, S. W., Loeb, W. E. & White, C. E. Poly($\alpha, \alpha, \alpha', \alpha'$-tetrafluoro-p-xylylene). *J. Appl. Polym. Sci.* **13,** 2325 (1969).

106. Lang, C.-I., Yang, G.-R., Moore, J. A. & Lu, T.-M. Vapor Deposition Of Very Low K Polymer Films, Poly(Naphthalene), Poly(Fluorinated Naphthalene). *MRS Online Proc. Libr. Arch.* **381,** 45 (1995).

107. Talbi, F., Lalam, F. & Malec, D. DC conduction of Al 2 O 3 under high electric field. *Journal of Physics D: Applied Physics* **40,** 3803 (2007).

108. Neusel, C. *et al.* Thickness-dependence of the breakdown strength: Analysis of the dielectric and mechanical failure. *Journal of the European Ceramic Society* **35,** 113–123. ISSN: 0955-2219 (2015).

109. Sikder, A. K., Irfan, I. M., Kumar, A. & Anthony, J. M. Nano-indentation studies of xerogel and SiLK low-K dielectric materials. *J. Electron. Mater.* **30,** 1527. ISSN: 1543-186X (2001).

110. Uhlig, M. & Gessner, T. in *Interlayer Dielectrics for Semiconductor Technologies* (eds Murarka, S., Eizenberg, M. & Sinha, A.) 201–225 (Academic Press, San Diego, 2003). ISBN: 978-0-12-511221-5. doi:`https://doi.org/10.1016/B978-012511221-5/50009-X`.

111. Leung, C. & Ong, E. in *Interlayer Dielectrics for Semiconductor Technologies* (eds Murarka, S., Eizenberg, M. & Sinha, A.) 121–156 (Academic Press, San Diego, 2003). ISBN: 978-0-12-511221-5. doi:`https://doi.org/10.1016/B978-012511221-5/50007-6`.

112. Motoyoshi, M. Through-Silicon Via (TSV). *Proceedings of the IEEE* **97,** 43–48. ISSN: 0018-9219 (Jan. 2009).

113. Gupta, S., Navaraj, W. T., Lorenzelli, L. & Dahiya, R. Ultra-thin chips for high-performance flexible electronics. *npj Flexible Electronics* **2,** 8. ISSN: 2397-4621 (2018).

114. Yoon, S. J. *et al.* Surface-Localized Sealing of Porous Ultralow-k Dielectric Films with Ultrathin (<2 nm) Polymer Coating. *ACS Nano* **11,** 7841–7847 (2017).

115. Manbachi, A. & Cobbold, R. S. C. Development and Application of Piezoelectric Materials for Ultrasound Generation and Detection. *Ultrasound* **19,** 187–196 (2011).

116. Ikeda, T. *Fundamentals of Piezoelectricity* ISBN: 0-19-856339-6 (Oxford University Press, 1990).

117. Mason, W. P. Piezoelectricity, its history and applications. *The Journal of the Acoustical Society of America* **70,** 1561–1566 (1981).

118. Cady, W. G. The Piezo-Electric Resonator. *Proceedings of the Institute of Radio Engineers* **10,** 83–114. ISSN: 0731-5996 (Apr. 1922).

119. Horton, J. W. & Marrison, W. A. Precision Determination of Frequency. *Proceedings of the Institute of Radio Engineers* **16,** 137–154. ISSN: 0731-5996 (Feb. 1928).

120. Stephens, C. & Dennis, M. Engineering Time: Inventing the Electronic Wristwatch. *The British Journal for the History of Science* **33,** 477–497. ISSN: 00070874, 1474001X (2000).

121. Zhou, Q., Lau, S., Wu, D. & Shung, K. K. Piezoelectric films for high frequency ultrasonic transducers in biomedical applications. *Progress in Materials Science* **56,** 139–174. ISSN: 0079-6425 (2011).

122. Lee, C., Itoh, T. & Suga, T. Micromachined piezoelectric force sensors based on PZT thin films. *IEEE Transactions on Ultrasonics, Ferroelectrics, and Frequency Control* **43,** 553–559. ISSN: 0885-3010 (July 1996).

123. Langdon, R. M. Resonator sensors-a review. *Journal of Physics E: Scientific Instruments* **18,** 103 (1985).

124. Aigner, R. *SAW and BAW technologies for RF filter applications: A review of the relative strengths and weaknesses* in *2008 IEEE Ultrasonics Symposium* (Nov. 2008), 582–589. doi:`10.1109/ULTSYM.2008.0140`.

125. Anton, S. R. & Sodano, H. A. A review of power harvesting using piezoelectric materials (2003–2006). *Smart Materials and Structures* **16,** R1 (2007).

126. Moheimani, S. O. R. Invited Review Article: Accurate and fast nanopositioning with piezoelectric tube scanners: Emerging trends and future challenges. *Review of Scientific Instruments* **79,** 071101 (2008).

127. Jung, J. *et al.* Review of piezoelectric micromachined ultrasonic transducers and their applications. *Journal of Micromechanics and Microengineering* **27,** 113001 (2017).

128. Scrymgeour, D. A. & Hsu, J. W. P. Correlated Piezoelectric and Electrical Properties in Individual ZnO Nanorods. *Nano Letters* **8,** 2204–2209 (2008).

129. Scrymgeour, D. A., Sounart, T. L., Simmons, N. C. & Hsu, J. W. P. Polarity and piezoelectric response of solution grown zinc oxide nanocrystals on silver. *Journal of Applied Physics* **101,** 014316 (2007).

130. Lee, H. *et al.* The stress-dependent piezoelectric coefficient of ZnO wire measured by piezoresponse force microscopy. *Scripta Materialia* **66,** 101–104. ISSN: 1359-6462 (2012).

131. Broitman, E., Soomro, M. Y., Lu, J., Willander, M. & Hultman, L. Nanoscale piezoelectric response of ZnO nanowires measured using a nanoindentation technique. *Phys. Chem. Chem. Phys.* **15,** 11113–11118 (26 2013).

132. Nour, E. S. *et al.* Piezoelectric and opto-electrical properties of silver-doped ZnO nanorods synthesized by low temperature aqueous chemical method. *AIP Advances* **5,** 077163 (2015).

133. Bowen, C., Kim, H., Weaver, P. & Dunn, S. Piezoelectric and ferroelectric materials and structures for energy harvesting applications. *Energy & Environmental Science* **7,** 25–44 (2014).

134. Cava, R. J. Oxide superconductors. *Journal of the American Ceramic Society* **83,** 5–28 (2000).

135. Zhai, T. *et al.* A comprehensive review of one-dimensional metal-oxide nanostructure photodetectors. *Sensors* **9,** 6504–6529 (2009).

136. Geissler, M. & Xia, Y. Patterning: Principles and some new developments. *Advanced Materials* **16,** 1249–1269 (2004).

137. Sun, K. *et al.* 3D printing of interdigitated Li-Ion microbattery architectures. *Advanced Materials* **25,** 4539–4543 (2013).

138. Yu, M. *et al.* Semiconductor nanomembrane tubes: three-dimensional confinement for controlled neurite outgrowth. *ACS nano* **5,** 2447–2457 (2011).

139. Schumann, M., Bückmann, T., Gruhler, N., Wegener, M. & Pernice, W. Hybrid 2D–3D optical devices for integrated optics by direct laser writing. *Light: Science & Applications* **3,** e175 (2014).

140. Dal Corso, A., Posternak, M., Resta, R. & Baldereschi, A. Ab initio study of piezoelectricity and spontaneous polarization in ZnO. *Phys. Rev. B* **50,** 10715–10721 (15 Oct. 1994).

141. Lifson, M. L., Levey, C. G. & Gibson, U. J. Diameter and location control of ZnO nanowires using electrodeposition and sodium citrate. *Applied Physics A* **113,** 243–247. ISSN: 1432-0630 (Oct. 2013).

142. Tynell, T. & Karppinen, M. Atomic layer deposition of ZnO: a review. *Semiconductor Science and Technology* **29,** 043001 (2014).

143. Wu, W., Wen, X. & Wang, Z. L. Taxel-Addressable Matrix of Vertical-Nanowire Piezotronic Transistors for Active and Adaptive Tactile Imaging. *Science* **340,** 952–957. ISSN: 0036-8075 (2013).

144. Chang, P.-C. *et al.* High-performance ZnO nanowire field effect transistors. *Applied Physics Letters* **89,** 133113 (2006).

145. Fonseca, R. D. *et al.* Fabrication of zinc oxide nanowires/polymer composites by two-photon polymerization. *Journal of Polymer Science Part B: Polymer Physics* **52,** 333–337 (2014).

146. Tolstova, Y., Omelchenko, S. T., Blackwell, R. E., Shing, A. M. & Atwater, H. A. Polycrystalline Cu2O photovoltaic devices incorporating Zn(O,S) window layers. *Solar Energy Materials and Solar Cells* **160,** 340–345. ISSN: 0927-0248 (2017).

147. Arakelova, E., Khachatryan, A., Kteyan, A., Avjyan, K. & Grigoryan, S. ZnO film deposition by DC magnetron sputtering: Effect of target configuration on the film properties. *Thin Solid Films* **612,** 407–413. ISSN: 0040-6090 (2016).

148. Chandra, S., Bhatt, V. & Singh, R. RF sputtering: A viable tool for MEMS fabrication. *Sadhana* **34,** 543. ISSN: 0973-7677 (Oct. 2009).

149. Kumar, G., Kumar, R. & Kumar, A. ZnO Thin Films: Chemical Vapour Deposition, Growth and Functional Properties. *Reviews in Advanced Sciences and Engineering* **5,** 150–160. ISSN: 2157-9121 (2016).

150. Kumar, R., Kumar, G. & Umar, A. Pulse Laser Deposited Nanostructured ZnO Thin Films: A Review. *Journal of Nanoscience and Nanotechnology* **14,** 1911–1930. ISSN: 1533-4880 (2014).

151. Shen, D. *et al.* The design, fabrication and evaluation of a MEMS PZT cantilever with an integrated Si proof mass for vibration energy harvesting. *Journal of Micromechanics and Microengineering* **18,** 055017 (2008).

152. Han, Z., Salmi, E., Vehkamäki, M., Leskelä, M. & Ritala, M. Metal oxide multilayer hard mask system for 3D nanofabrication. *Nanotechnology* **29,** 055301 (2018).

153. Araki, S. *et al.* Fabrication of Nanoshell-Based 3D Periodic Structures by Templating Process using Solution-derived ZnO. *Nanoscale research letters* **12,** 419 (2017).

154. Liu, Z. *et al.* Synthesis and cathodoluminescence properties of porous wood (fir)-templated zinc oxide. *Ceramics International* **34,** 69–74 (2008).

155. Giakoumaki, A. N. *et al.* 3D micro-structured arrays of ZnO nanorods. *Scientific Reports* **7,** 2100 (2017).

156. Bagal, A. *et al.* Large-Area Nanolattice Film with Enhanced Modulus, Hardness, and Energy Dissipation. *Scientific Reports* **7,** 9145 (2017).

157. Zhou, X. & Liu, C. Three-dimensional Printing for Catalytic Applications: Current Status and Perspectives. *Advanced Functional Materials* **27,** 1701134 (2017).

158. Ruiz-Morales, J. *et al.* Three dimensional printing of components and functional devices for energy and environmental applications. *Energy & Environmental Science* **10,** 846–859 (2017).

159. Bertrand, P., Bayle, F., Combe, C., Gœuriot, P. & Smurov, I. Ceramic components manufacturing by selective laser sintering. *Applied Surface Science* **254,** 989–992 (2007).

160. Exner, H. *et al.* Laser micro sintering: A new method to generate metal and ceramic parts of high resolution with sub-micrometer powder. *Virtual and physical prototyping* **3,** 3–11 (2008).

161. Wilkes, J., Hagedorn, Y.-C., Meiners, W. & Wissenbach, K. Additive manufacturing of ZrO2-Al2O3 ceramic components by selective laser melting. *Rapid Prototyping Journal* **19,** 51–57 (2013).

162. Yves-Christian, H., Jan, W., Wilhelm, M., Konrad, W. & Reinhart, P. Net shaped high performance oxide ceramic parts by selective laser melting. *Physics Procedia* **5,** 587–594 (2010).

163. Salea, A., Prathumwan, R., Junpha, J. & Subannajui, K. Metal oxide semiconductor 3D printing: Preparation of copper (II) oxide by fused deposition modelling for multi-functional semiconducting applications. *Journal of Materials Chemistry C* **5,** 4614–4620 (2017).

164. Chen, K., Chen, Y. & Wei, W. *3D printed ZnO absorbent for desulfurization of syngas fuel* in *System Integration (SII), 2017 IEEE/SICE International Symposium on* (IEEE, 2017), 115–120.

165. Zhang, J. *et al.* 3D-printed magnetic Fe 3 O 4/MBG/PCL composite scaffolds with multifunctionality of bone regeneration, local anticancer drug delivery and hyperthermia. *Journal of Materials Chemistry B* **2,** 7583–7595 (2014).

166. Wang, J. & Shaw, L. L. Fabrication of functionally graded materials via inkjet color printing. *Journal of the American Ceramic Society* **89,** 3285–3289 (2006).

167. Saleh, E. *et al.* 3D inkjet-printed UV-curable inks for multi-functional electromagnetic applications. *Additive Manufacturing* **13,** 143–148 (2017).

168. Liu, X., Tarn, T.-J., Huang, F. & Fan, J. Recent advances in inkjet printing synthesis of functional metal oxides. *Particuology* **19,** 1–13 (2015).

169. Wu, H. *et al.* Fabrication of dense zirconia-toughened alumina ceramics through a stereolithography-based additive manufacturing. *Ceramics International* **43,** 968–972 (2017).

170. Schwentenwein, M. & Homa, J. Additive manufacturing of dense alumina ceramics. *International Journal of Applied Ceramic Technology* **12,** 1–7 (2015).

171. Mitteramskogler, G. *et al.* Light curing strategies for lithography-based additive manufacturing of customized ceramics. *Additive Manufacturing* **1,** 110–118 (2014).

172. Manapat, J. Z., Chen, Q., Ye, P. & Advincula, R. C. 3D printing of polymer nanocomposites via stereolithography. *Macromolecular Materials and Engineering* **302,** 1600553 (2017).

173. Tesavibul, P. *et al.* Processing of 45S5 Bioglass® by lithography-based additive manufacturing. *Materials Letters* **74,** 81–84 (2012).

174. Zocca, A., Colombo, P., Gomes, C. M. & Günster, J. Additive manufacturing of ceramics: issues, potentialities, and opportunities. *Journal of the American Ceramic Society* **98,** 1983–2001 (2015).

175. Hinczewski, C., Corbel, S. & Chartier, T. Ceramic suspensions suitable for stereolithography. *Journal of the European Ceramic Society* **18,** 583–590 (1998).

176. Kotz, F. *et al.* Three-dimensional printing of transparent fused silica glass. *Nature* **544,** 337 (2017).

177. Chartier, T., Chaput, C., Doreau, F. & Loiseau, M. Stereolithography of structural complex ceramic parts. *Journal of materials science* **37,** 3141–3147 (2002).

178. Zanchetta, E. *et al.* Stereolithography of SiOC ceramic microcomponents. *Advanced Materials* **28,** 370–376 (2016).

179. Eckel, Z. C. *et al.* Additive manufacturing of polymer-derived ceramics. *Science* **351,** 58–62 (2016).

180. Colombo, P., Mera, G., Riedel, R. & Soraru, G. D. Polymer-derived ceramics: 40 years of research and innovation in advanced ceramics. *Journal of the American Ceramic Society* **93,** 1805–1837 (2010).

181. Brigo, L. *et al.* 3D Nanofabrication of SiOC Ceramic Structures. *Advanced Science,* 1800937 (2018).

182. Vyatskikh, A., Kudo, A., Delalande, S. & Greer, J. R. Additive manufacturing of polymer-derived titania for one-step solar water purification. *Materials Today Communications* **15,** 288–293 (2018).

183. Padolskytė, V. *et al. 3D opto-structuring of ceramics at nanoscale* in *3D Printed Optics and Additive Photonic Manufacturing* **10675** (International Society for Optics and Photonics, 2018), 106750U. doi:`10.1117/12.2306883`.

184. Yu, S. *et al.* Direct Laser Writing of Crystallized TiO2 and TiO2/Carbon Microstructures with Tunable Conductive Properties. *Advanced Materials,* 1805093 (2018).

185. Yeh, C.-C. *et al.* Chemical and structural investigation of zinc-oxo cluster photoresists for DUV lithography. *Journal of Materials Chemistry C* **5,** 2611–2619 (2017).

186. Schneller, T., Waser, R., Kosec, M. & Payne, D. *Chemical solution deposition of functional oxide thin films* (Springer, 2013).

187. Danks, A., Hall, S. & Schnepp, Z. The evolution of 'sol–gel' chemistry as a technique for materials synthesis. *Materials Horizons* **3,** 91–112 (2016).

188. Hwang, C.-C. & Wu, T.-Y. Synthesis and characterization of nanocrystalline ZnO powders by a novel combustion synthesis method. *Materials Science and Engineering: B* **111,** 197–206 (2004).

189. Trolier-McKinstry, S., Zhang, S., Bell, A. J. & Tan, X. High-Performance Piezoelectric Crystals, Ceramics, and Films. *Annual Review of Materials Research* **48,** 191–217 (2018).

190. Guilbault, G. G., Jordan, J. M. & Scheide, E. Analytical Uses of Piezoelectric Crystals: A Review. *C R C Critical Reviews in Analytical Chemistry* **19,** 1–28 (1988).

191. Alexander, C. & Sadiku, M. *Fundamentals of electric circuits* Fourth Edition. ISBN: 978–0–07–352955–4 (McGraw-Hill, Inc., 2009).

192. Ward, R. W. *The Constants of Alpha Quartz* in *38th Annual Symposium on Frequency Control* (May 1984), 22–31. doi:`10.1109/FREQ.1984.200732`.

193. Ballato, A. in *Piezoelectricity: Evolution and Future of a Technology* 9–35 (Springer Berlin Heidelberg, Berlin, Heidelberg, 2008). ISBN: 978-3-540-68683-5. doi:`10.1007/978-3-540-68683-5_2`.

194. Lee, J., Nam, S. C. & Tak, Y. On the origin of electrodeposition mechanism of ZnO on ITO substrate. *Korean Journal of Chemical Engineering* **22,** 161–164. ISSN: 1975-7220 (Jan. 2005).

A p p e n d i x   A

FABRICATION CHALLENGES

A.1   Hollowing
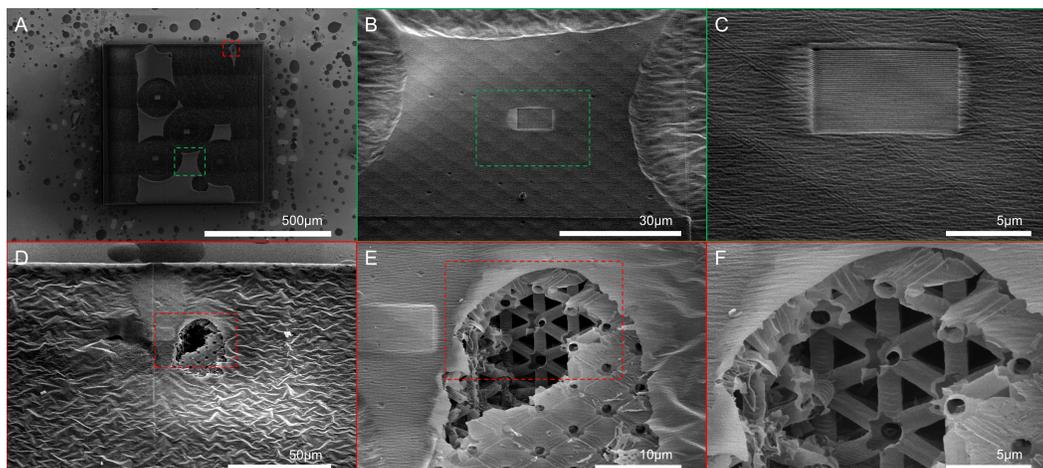
Figure A.1: SEM images of an attempted second FIB procedure to open new holes in the alumina coating in order to speed the hollowing process. A) Top-down SEM image of a large stitched nanolattice capacitor after two weeks in an oxygen plasma environment. The lighter contrast regions indicate polymer remains present in the structure. The green box designates a successful new FIB opening that can be seen at higher magnification in panel B. The red box designates a failed FIB procedure that can be seen in greater detail in panel D. B) Higher magnification of a new FIB window milled into a region with remaining polymer, the green box is C) a higher magnification of the FIB window, revealing the underlying polymer. D) Overview of a failed new FIB window procedure. The square of slightly different contrast depicts where the window was attempted. During this milling, material was ejected out of the adjacent hollow region, likely due to charge buildup and subsequent dielectric breakdown. The red box is E) a closer view of the damage with a red box F) a higher magnification of the underlying nanolattice, showing the hollow nature of the tubes and nodes.

In order to measure the electrical properties of the hollow alumina nanolattices, we needed to create a large area nanolattice, with some approaching 1 mm x 1 mm for taller designs. It was quickly discovered that hollowing these large stitched nanolattices required an unsustainable amount of time in the oxygen plasma when removing the outer alumina coating on the two edges alone. In order to provide additional exposure to the oxygen plasma, windows were created in the top alumina

plate using the FIB to carefully mill square patterns, stopping within the underlying polymer in order to avoid damaging the nanolattice below. On several occasions, after two continuous weeks in the oxygen plasma, it was discovered that there either were an insufficient number of holes or that the thin alumina shell had collapsed and closed off areas, preventing the hollowing process.

In order to remedy this situation without fabricating entirely new structures, we attempted a second FIB session to open more windows to the underlying polymer. Figure A.1 illustrates this process. Figure A.1A shows a top-down SEM image of the nanolattice, where the lighter contrast regions indicate polymer remains in the tubes of the nanolattice. Figure A.1B-C show a successful attempt at milling a window into the underlying polymer to allow for a quicker remover in the oxygen plasma. Figure A.1D-F depicts a significant failure of this process, which ultimately rendered this capacitor unusable. Milling the window into a polymer region in proximity to a hollow region caused a catastrophic ejection of material, likely due to charge build up in the polymer. This experience indicates that it's important to place sufficient openings for removing the polymer before any oxygen plasma process has done. If future FIB work is required, it's important to avoid locations that are close to hollow regions.

A.2 Delamination
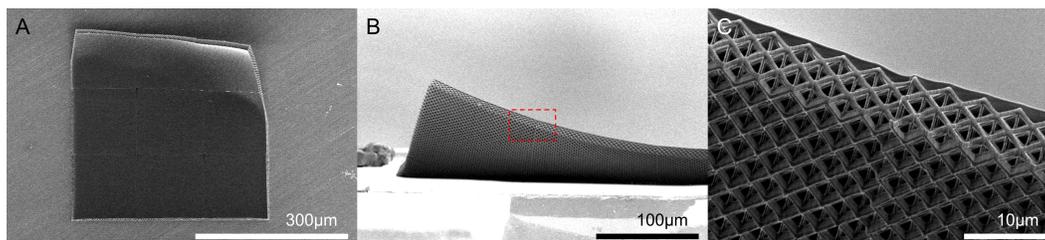
Figure A.2: SEM images of delamination of a large stitched nanolattice. A) Top-down SEM image of a large stitched nanolattice capacitor with top portion of the image delaminated from the substrate. B) Side image of the delaminated nanolattice, creating a fin-like structure, with the red dashed box marking a C) close-up image of a seam portion of the nanolattice suspended above the substrate. There is no apparent damage to the integrity of the structure.

Another common failure is delamination of the structure from the substrate. Interestingly, this does not always correspond to damage of the underlying nanolattice. Seams between nanolattices can be maintained despite significant deflection, such as the situation depicted in Figure A.2. This could allow for the purposeful creation

of fins or other curved surfaces composed of an architected material sheet. In order to correct this, additional surface find segments were added to the TPL write process to ensure the write always began at the substrate surface. These surface find steps add additional time to the write and can cause discontinuities if debris exists on the surface; however, for cleaned substrates this fix resulted in a continuous layer of architected material that was well-adhered to the substrate.

MECHANICAL DATA CORRECTIONS

In order to present accurate mechanical data, several measurement factors must be considered. The load frame stiffness of the nanoindenter is already factored into the measurement and is occasionally checked against a known reference. Over small displacements, these reference calibrations are quite sufficient. However, the large distances involved with these experiments introduce two additional sources of error that need to be corrected when the displacement is controlled by the load cell, such as in the ex-situ case. The most apparent error is due to non-linearity in the spring. This can be corrected by performing an indent in air and subtracting this baseline force measurement from the data at corresponding raw displacements of the indenter. The second error is a linear drift that is observed as a linearly changing load such that the load at zero displacement after unloading is not at the starting load. It should be noted that this drift is distinct from thermal drift and is always in the same direction for a given tool.
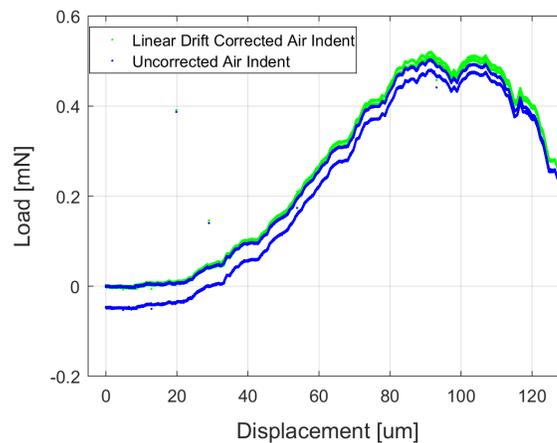

Figure B.1: Load displacement data for an uncorrected air indent (blue) compared to the linear drift corrected air indent (green).

Figure B.1 shows an uncorrected air indent in blue. The linear load drift can be removed from the air indent data by creating a linear function of the form:

$$P_{LD} = mt + b \tag{B.1}$$

with

$$m = \frac{(P_f - P_i)}{(t_f - t_i)}$$
<div align="right">(B.2)</div>

where P_{LD} is the linear load drift, P_f and P_i are the final and initial loads at the reference displacement, respectively, and t_f and t_i are the final and initial time values corresponding to these loads, respectively. When the displacement is normalized to 0, as is here the case, $b = 0$. The corrected version of the air indent can be seen as the green curve in Figure B.1.
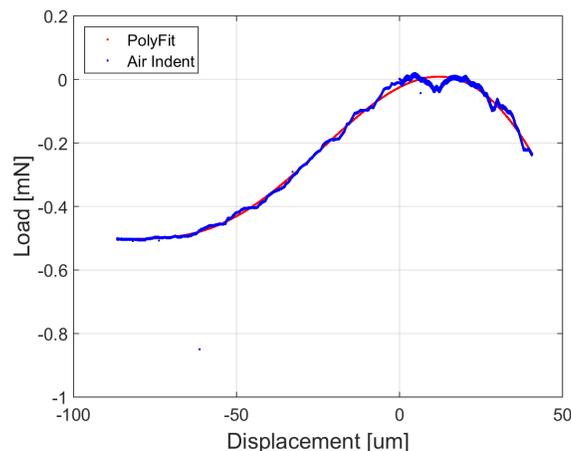

Figure B.2: Linear drift corrected air indent (blue) compared to the polynomial function generated to estimate the spring error of the measurement over the displacement range of the experiment.

This same linear load drift correction can be applied to the raw mechanical data. In order to apply the air indent to the data, we create a polynomial fit to the data to create a function that relates the load offset to the raw displacement. We have chosen a 5th order polynomial for these functions, as they correlate well to the data with an R value above 0.996 for all types of samples except one, which had an R value of 0.981. The polynomial fit for the illustrated example can be found as the red line in Figure B.2, compared to the linear load corrected air indent in blue.

Armed with the polynomial for the spring correction, we can now subtract this function from the linear load drift corrected data. This results in both corrections applied to the data, such that there is no load at zero displacement at the end of each displacement cycle and the non-linearity of the spring is accounted for. An example of only load drift corrected data in red is compared to a combined spring and drift corrected data set in blue for an 8 µm unit cell uniform density nanolattice in Figure
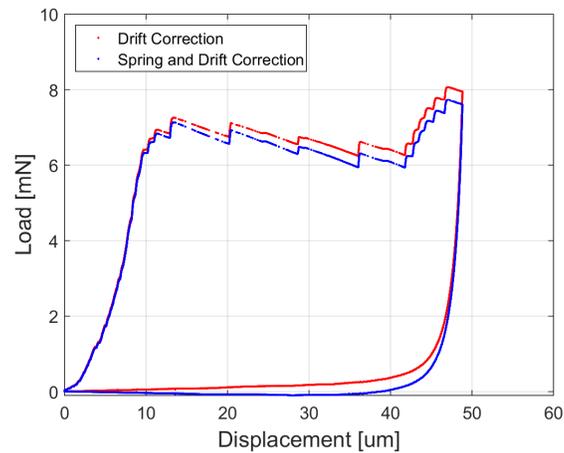
Figure B.3: Load drift correction only data (red) compared to both spring and load drift correction data (blue).

B.3. This has only a small effect on the Young's modulus and strength, but it displays an unloading curve that is much more representative of the physical system, with zero load for the entirety of the unload portion once the tip has lost contact with the sample. As a note, these spring measurement corrections are not necessary for in-situ experiments where the extension arm is used to apply displacement, because the load cell displacement is held constant, resulting in no meaningful spring travel.